# Developing Lower Cost Radiotherapy Solutions for Low and Middle Income Countries

by

Jericho O'Connell
B.Sc., University of Victoria, 2018

A Report Submitted in Partial Fulfillment of the
Requirements for the Degree of

Doctor of Philosophy

in the Department of Physics and Astronomy

Developing Lower Cost Radiotherapy Solutions for Low and Middle Income Countries

by

Jericho O'Connell
B.Sc., University of Victoria, 2018

Supervisory Committee

---

Dr. Magdalena Bazalova-Carter, Supervisor
(Department of Physics and Astronomy)

---

Dr. Derek Wells, Departmental Member
(Department of Physics and Astronomy)

---

Dr. Margaret-Anne Storey, Outside Member
(Department of Computer Science)

# Abstract

Radiotherapy research often focuses on state-of-the-art methods to provide small improvements in the treatment of patients in high-income countries, while less focus is put on providing low-cost treatments suitable for the majority of people in the world who have little or no access to radiotherapy. In an effort to remedy this paradigm we optimise, design, and benchmark lower cost radiotherapy treatment modalities with the overarching goal of increasing treatment accessibility in low- and middle-income countries (LMICs).

This body of work has focused on the simulation of cost reducing modification to linacs, in an effort to reduce linac production cost while maintaining treatment efficacy. One method is to simplify current linacs through the elimination of the kilovoltage on-board CT imaging system (kV-OBI). The removal of the kV-OBI would greatly reduce production costs of treatment linacs. However, the removal of the makes many image guided radiotherapy (IGRT) treatments infeasible, treatments which form the bulk of modern radiotherapy. To allow IGRT without the kV-OBI, novel megavoltage cone beam CT (MV-CBCT) methods are simulated to find low-cost setups that provide image quality similar to kV-OBIs. Additionally, cost reduction can be achieved through redesigning current radiotherapy machines by replacing expensive linear accelerator-based treatment heads with low-cost x-ray tubes. To validate this methodology, arc treatments were simulated on a simplified isocentric kilovoltage arc (SITKA) treatment machine with a novel treatment planning system. Additionally, machine learning solutions are used to ameliorate the systems OBI image quality such that a separate planning CT machine is not needed.

The Fastcat tool was developed to rapidly simulate CBCT through a combination of pre-calculated Monte Carlo (MC) data and GPU raytracing. To demonstrate this tool improvements, addressing the low contrast to noise ratio in MV-CBCT were studied and proposed. The rapid prototyping of CBCT setups available through Fastcat greatly improve the development of CBCT systems by providing a fast alternative to time-consuming MC simulations in key development situations: Allowing researchers to efficiently optimize a CBCT detector design based on quick feedback in terms of image quality in phantoms for a given dose. This was seen through utilization of Fastcat for the purpose of virtual clinical trials and detector design optimization of novel perovskite and cadmium tungstate (CWO) detectors Perovskite detectors showed higher contrast to noise ratio (CNR) and spatial resolution, resulting in better image quality for clinical tasks such as patient positioning and micro-calcification detection, all at a very low manufacturing cost. Likewise, the novel, low-cost system in combination with adaptive machine learning methods and novel planning is demonstrated to provide clinically practical lung treatments that meet the urgent and increasing demand for radiotherapy treatment in low-income countries as well as rural and remote areas.

# Contents

# List of Tables

# List of Figures

# Acknowledgements

While I was the one who supplied the keystrokes to produce this document, none of it would have happened without Magdalena. And while, as I'm sure she would tell you, I don't listen to her all the time, I did listen to her when she told me to do a PhD. So, the credit (or blame) for this remarkable (or satisfactory) body of work should go to her. She is my constant advocate and supporter, providing steadfast belief and encouragement. Having now been introduced (by her) to many wonderful people in the medical physics community, I believe there is no better supervisor for me. I would also like to express my deep gratitude to my supervisory committee members, Dr. Margaret-Anne Storey and Dr. Derek Wells, for their insightful guidance throughout my PhD journey. I am also thankful to Dr. Michael Weil, who has been a supportive mentor, offering valuable clinical and grammatical insights for my work. Thanks to my friends in the XCITE lab who through a magical feat made academics not only tolerable but occasionally enjoyable. I would also like to thank the Natural Sciences and Engineering Research Council of Canada for providing generous CGS-D funding in support of my PhD studies as well as the FGS and the department for their award nominations. Thanks specifically to my Uncle Art who would get a kick out of being in my acknowledgements. Perhaps most of all, I would like to thank my friends and family, not specifically for this thesis but in the same holistic sense in which I will be endlessly grateful for them.

*I acknowledge and respect the lekwungen peoples on whose traditional territory the university stands and the Songhees, Esquimalt and WS̱ÁNEĆ peoples whose historical relationships with the land continue to this day. Special thanks to Janet Dick of the Songhees and her generous gift of honorary membership to her clan.*

# Dedication

To my parents, Joan and Dan, and my brothers, Noah and Will.

*"I will arise and go now, and go to Innisfree,*
*And a small cabin build there, of clay and wattles made;"*
— W. B. Yeats (speculating about what to do after his doctorate)

# Chapter 1

# Introduction

In the context of public health today, cancer remains a leading cause of death worldwide. According to the latest estimates from the International Agency for Research on Cancer (IARC), there were approximately 19.3 million new cancer cases and 10 million cancer-related deaths globally in 2020 [1]. In Canada alone, it is estimated that there were 233 thousand new cancer cases and 85 thousand cancer-related deaths in 2021. By current estimates, 44 out of 100 men and 43 out of 100 women will develop cancer during their lifetime. As the demand for cancer care continues to grow, there is an increasing need for effective and affordable cancer treatments[2].

Radiotherapy is a critical component of cancer care, using high-energy radiation to destroy cancer cells and shrink tumors. The treatment works by damaging the DNA of cancer cells, preventing them from dividing and growing. This technique can be applied at any stage of cancer, either as the primary treatment or in conjunction with other therapies. The radiation can be delivered to the affected area through external beams or internal implants. Radiation oncologists, medical physicists, and radiation therapists work together to design and administer personalized treatment plans, ensuring that the radiation is delivered precisely to the targeted cancer cells while minimizing exposure to healthy tissues. Radiotherapy has become increasingly sophisticated over the years, incorporating state-of-the-art imaging technology, including computed tomography (CT) and magnetic resonance imaging (MRI), to accurately locate tumors and guide treatment delivery.

Cancer care in high-income countries (HICs) and low- and middle-income countries (LMICs) presents a stark contrast. While HICs have advanced technologies and sophisticated treatment options, LMICs often lack basic cancer care resources. In HICs, early detection of cancer is common, and treatment options are diverse and readily available. This includes access to surgery, chemotherapy, radiation therapy, and supportive care services. However, in LMICs, most cancer cases are diagnosed at later stages, when treatment is less effective, and often with limited options. Additionally, the availability of trained oncology professionals and infrastructure to support cancer care is often limited in LMICs. This disparity in cancer care highlights the urgent need to develop cost-effective and sustainable approaches to cancer prevention, diagnosis, and treatment that can be implemented in LMICs to improve cancer care outcomes.

## 1.1 Cancer in Low- and Middle- Income Countries

In 2020, of 10.35 million new cases of cancer in LMIC more than 70% did not have access to proper treatment for their disease [1]. The development of low-cost radiotherapy treatment machines is imperative for improving cancer outcomes for patients in LMIC as x-ray treatment is effective as a single or combined modality for local–regional tumor control [3, 4]. To treat the unserviced population in LMICs the World Health Organisation estimates 5000 megavoltage (MV) radiotherapy linear accelerators (linacs) are needed [5]. With new linacs costing on the order of $5M USD, the sort of investment for procurement and operation of this many machines will likely not be garnered by LMICs. This lack of low cost treatment options in LMICs is the premise behind my PhD work, and specifically, I am investigating two independent solutions to lowering the cost of these radiotherapy machines: The first is through the elimination of the costly kilovoltage on-board imagers (kV-OBI) through the introduction of novel MV imaging detector materials in combination with low atomic number linac targets to make a lower cost treatment machine. The second is the development of a very low cost kilovoltage radiotherapy system.

To motivate the necessity to improve MV imaging technology it is helpful to have some background in recent radiotherapy development. Currently, there is a huge potential for increasing the throughput of conventional radiotherapy machines. With new stereotactic ablative radiotherapy (SABR) treatments being used throughout the developed world [6, 7, 8, 9, 10], cancer sites that once would have required a month of once per day radiotherapy treatment can now be treated within a week using relatively few fractions of radiation. This opens up the possibility of very high patient throughput for some treatment sites if these treatments can be performed in LMICs [11].

However, to perform these SABR treatments some technical aspects must be addressed that prove challenging in LMICs. A key challenge in SABR treatment is to position the patient accurately during treatment so that the treatment beam precisely hits the patient's tumour [12, 13]. The best way to ensure proper treatment positioning is to use a kilovoltage cone beam CT system (kV-CBCT) mounted to the treatment machine. Unfortunately, these kV-CBCT systems contribute significantly to the cost of the radiotherapy machine. While a pre-owned treatment machine without a kV-CBCT system can cost as low as $175,000 USD, pre-owned machines with kV-CBCT capability are generally over three times this amount [14].

## 1.2 MV CBCT

To avoid the added cost of a kV-CBCT system, megavoltage CBCT (MV-CBCT) can be used to acquire CT scans with the treatment beam itself [15, 16]. The downside of MV-CBCT is that the CT images acquired have lower contrast and require a higher patient radiation dose to maintain equivalent image quality to kV-CBCT [17] as seen in Figure 1.1. Current solutions for improving the image quality of MV-CBCT include introducing multiple beam modes, some with characteristics for treatment and others with characteristics for imaging [18, 19, 20]. Likewise, the x-ray detector design is an active area of development with new detector materials providing higher detection efficiency of x-rays, resulting in lower noise for MV beams [17, 21, 22]. To improve MV imaging quality, novel low atomic number (Z) beam targets have been examined to generate photon beams with higher fluence in the kV range. The use of aluminum and carbon targets has been shown to improve image quality: Simulation studies show a 16-19% increase in contrast between an aluminum target and the default tungsten target for a 6 MV photon beam [23, 24]. Experimentally, Baek *et al.* showed that a gantry mounted aluminum target improved the limiting spatial frequency (f50) from 0.451 lp/mm to 0.745 lp/mm for a tungsten target 6 MV beam [25]. Additionally, Parsons *et al.* showed an increase in the contrast to noise ratio (CNR) in projection images of cortical bone by factors ranging from 3.7 to 7.4 between carbon and aluminum targets with 2.35 and 1.9 MV photon beams and the default 6 MV tungsten imaging setup [18].

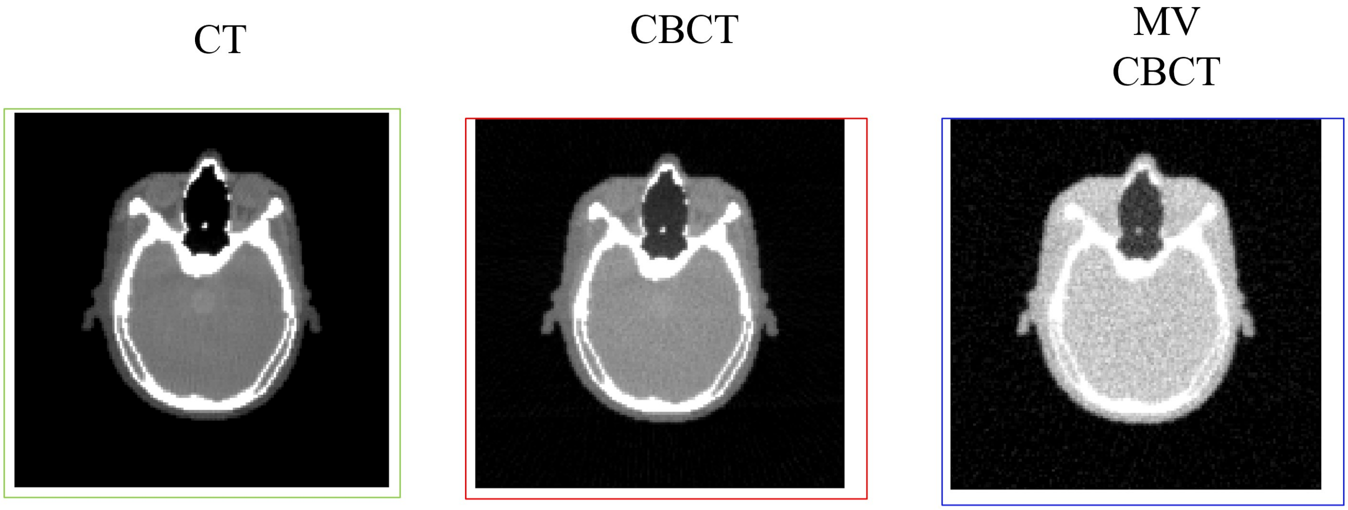

Figure 1.1: Qualitative image quality comparison between CT, CBCT, and MV-CBCT generated using the Fastcat simulation code.

Furthermore, advances in MV (electronic portal imager) EPID design have shown promise in improving MV image quality. Many MV EPIDs use a gadolinium oxysulfide (GOS) scintillator, which is opaque to its own scintillation photons. This limits the thickness of GOS detectors which in turn limits the quantum efficiency of the detector. Star-lack *et al.* examined cadmium tungstate (CWO) and bismuth germinate (BGO) detectors, which are higher Z materials and can be made thicker for MV photon detection [17]. CWO was noted to have a 20-fold efficiency improvement over GOS with significantly higher stability and light yield than BGO [17]. Likewise, image quality improvement was seen using multi-layer GOS imagers with 2-4 times greater CNR than an equivalent single layer GOS detector [21].

An additional novel material with high density and cheap production costs is Perovskite ($MAPbBr_3$)

which has very recently been used for medical imaging applications [26, 27, 28, 29, 30, 31, 32, 33]. Additionally, Perovskite has a high effective atomic number due to its lead content, which is a beneficial property for MV imaging applications. These crystals, which are generally used as solar cells, have recently demonstrated excellent spatial resolution for kV imaging [34, 35, 36]. Their lead content, high spatial resolution, and cheap production costs make them an attractive candidate as an MV detector material. However, the use of Perovskite crystals in MV imaging is currently an unexplored topic.

Currently, these two approaches to improving MV imaging, the amelioration of detector efficiencies and introduction of low-Z targets, have remained largely separate. Likewise, direct comparison of the benefit of different imaging strategies in the literature remains challenging as different works have different combinations of voxel size, cone-beam size, phantom dose, focal-spot size and other imaging variables.

Thus, to develop MV-CBCT setups with adequate image quality to enable SABR treatments on repurposed linacs, many candidate imaging setups are needed to be explored in a standardized manner. To do this, I developed a new simulation tool to evaluate CBCT setups in an efficient and standardized way. Below I will briefly describe some background for the simulation tool and other work that has been done in creating similar simulation tools.

### 1.3 CBCT Simulation

To quantify novel MV-CBCT imaging setup Monte Carlo (MC) simulation codes are generally used which are very accurate but also exceptionally computationally demanding. MC simulation codes transport subatomic particles individually using random numbers to model the probabilistic nature of quantum mechanical interactions. To properly simulate real world events like x-ray imaging, a large number of particles (often $10^8$ or more) need to be simulated to form an image, especially when simulating the special detector materials in medical imaging, called scintillators, which convert individual x-ray photons to many optical photons which can be measured more easily.

The long simulation time of MC simulation, especially for MV detector simulation, can be primarily attributed to two factors. First, MV detectors generally have low detective quantum efficiency (DQE), meaning that many particles that are transported in the simulation do not interact with the detector and do not contribute to image formation. A typical EPID DQE is as low as 1%-1.5% [22, 37]. Second, the scintillating detector in which the optical photons are produced generally has a high scintillation yield; generating thousands of optical photons to be transported per interaction event. These two factors result in simulation times often as long as 3,000 core-hours for a $10^7$ primary x-ray simulation of one EPID projection [38]. Further, to produce a clinically equivalent image of 1 MU with a $10 \times 10\text{cm}^2$ field size a simulation with more than $10^{11}$ photons is required [39, 40, 41]. This problem is compounded in CBCT simulation, where it is necessary to simulate many projections of the object for CBCT image reconstruction.

Large headway has been made to reduce this computational overhead. Star-lack *et al.* have shown that one can simulate the detector response with only a fraction of the scintillation yield, significantly reducing the computation time [40]. Likewise, by simulating the optical spread function at discrete energies beforehand and convolving these optical spread functions with the energy deposition of an absorbed photon one can avoid simulating the scintillation processes completely [42, 43]. Additionally, Shi *et al.* introduced the fastEPID framework which pre-calculates energy deposition efficiency ($\eta$) and optical spread function (OSF) to remove particle transport in the detector entirely without loss of image quality [39]. Where $\eta$ is defined as the ratio of the total energy deposition in the scintillator and the total x-ray photon energy incident on the detector. However, these simulations are still considered computationally intensive with one image at 1 MU taking $1.540 \times 10^4$ core-hours on an Intel Skylake CPU core (Intel Corp., Santa Clara, Ca). Other MC approaches that are promising for image simulation are the GPU methods used by Badal and Badano as well as Bert *et al.* [44, 45]. The approaches have seen MC simulation speedup factors of 27 and 80-90, respectively. However, at this time, open source GPU MC codes lack the stability and versatility of more established codes such as Geant4 or EGSnrc.

Conversely, one can forego MC methods and simulate fan and cone beam CT analytically to reduce computation time, an approach that is fast but does not produce the characteristic noise and scatter which are essential component to study in medical images. For example, ImaSim analytically simulates fan and cone beam CT through raytracing using vectorized phantoms [46]. VOXSI simulates kV fan beam CT using analytical raytracing with voxelized phantoms [47] and shows agreement with experimental images in terms of image contrast. DukeSim simulates kV fan beam CT with voxelized phantoms through a combination of analytical raytracing and GPU MC and demonstrates agreement between experimental and simulated images in terms of image contrast, noise magnitude, noise texture, and spatial resolution [48]. A drawback to the DukeSim approach is that the GPU MC reduces the simulation speed, requiring a 2-3 minute simulation per source rotation while running on 4 Nvidia Titan Xp GPUs with 64 GB of memory. Overall, none of these platforms are open-source and only DukeSim shows agreement with experimental noise and image contrast. Additionally, none of these platforms show experimental agreement for kV or MV CBCT.

In my PhD work I used a modified fastEPID pre-calculation of MC data for the detector response while also pre-calculating the energy spectrum of the beam source as well as energy dependent scatter kernels for a cylindrical water phantom. I combined this data with an analytical GPU raytracer that provides the primary particle attenuation. This simulation strategy is used to create Fastcat, an open source simulation tool I made for CBCT image simulation to enable studies of novel beam, detector, and phantom combinations. Fastcat shows good agreement with MC simulations of full CBCT data acquisition and it results in extremely short run times on the order of 1 GPU-minutes for a full CBCT simulation.

In my PhD work I also simulate image quality for combinations of novel MV beam target materials such as carbon and aluminum with different detector materials such as CWO and a novel Perovskite crystal detector. I compare these novel imaging methodologies with standard kV imaging setup devices such as columnar cesium iodide (CsI) detectors. I investigated whether the combination of novel MV beams and detectors can result in MV CBCT image quality approaching kV CBCT image quality in the effort to create a low cost SABR capable linac for LMICs.

### kV Treatment Machine Design

An entirely different approach can be used to lower the cost of radiotherapy treatment using kV treatments machines instead of linacs. While kV treatment machines cannot be expected to have comparable treatment efficacy and versatility to MV linear accelerators, their low cost makes them the only approach realistic for some LMICs. Thus, while the approach of modifying a pre-owned linac for SABR as described above may work for some middle income countries a different approach is likely needed for a much lower cost machine in many cases. Modern radiotherapy treatment machine design centres around the use of a linear accelerator to create MV photon beams. These beams are ideally suited to this task in that they can deposit cell damaging radiation in cancerous lesions deep in the human body while sparing the sensitive skin from radiation burns.

Historically, throughout the early $20^{th}$ century, kV photon beams were used in this application since they are simple to produce and have the same cell damaging properties as MV x-rays, however, these kV photon beams generally produced radiation burns on the patients' skin when used in this fashion. Currently, with advances in x-ray tube development, treatment planning optimization, and robotics there are opportunities to re-introduce kV photon beams as a treatment option for deep lesions in LMICs where treatment options are currently unavailable [49]. Additionally, kV photon beams show major benefits when used in combination with gold nanoparticles (GNPs), or other high atomic number materials as a radiosensitizer [50] and are much more effective in this regard than MV beams as they interact more strongly with high atomic number materials such as gold. Additionally, even though this GNP/kV treatment modality is quite promising for some deeper lesions, there is currently no commercial solution which is optimized for treating deep lesions with kV beams.

A key design feature of a kV treatment machine is to have multiple beams converging on the tumour. This allows the skin dose to be spread out over a large area, delivering sufficient dose delivered to the tumour while no individual area of skin is given a radiation dose above the threshold known to cause painful side effects for the patient. An additional attractive feature of kV x-rays incident on a high atomic number (Z) material such as gold or iodine will generally interact using the photo-electric effect. The photo-electric effect in turn produces Meitner electrons, sometimes referred to as Auger-electrons, these electrons deposit dose locally and are effective tumor radiosensitizers, increasing the efficacy of kV radiotherapy treatments. Previous designs have used a scanning electron beam over many targets to create many converging beams [51].

In 1999, a kV treatment modality constructed out of a repurposed CT scanner, termed CTRx, used a modified pencil-beam collimator to treat brain lesions in clinical trials [52, 53]. CTRx was capable of IGRT due to its ability to function as both a diagnostic and therapeutic system. Mesa *et al.* additionally used Monte Carlo dose calculations to investigate the dosimetric properties of the CTRx system used in conjunction with Iodine as a radiosensitizer. The energy spectrum used in the simulations was modelled after the 140 kVp setting of a GE CT scanner. Skull dose reduction was explored both by means of increasing the concentration of iodine (up to 20 mg/ml) in the tumor as well as the use of three non-coplanar (20°, 0° and -20°) treatment arcs by tilting the gantry. The CTRx treatments were compared to simulated treatments with a conventional 10 MV photon beam modelled after a linac. The CTRx system was capable of achieving suitable tumor dose distributions given sufficient iodine concentrations and non-coplanar beams.

In my work, I explore a novel design for a kV treatment system using a conventional x-ray tube mounted on an articulating robotic arm. This system leverages the decreased cost of robotic arms which can handle the weight of an x-ray tube at a cost of approximately $30K USD. This robotic arm would be used in combination with a 320 kV industrial x-ray tube to provide a non-coplanar kV-treatment machine. These machines could hypothetically cost less than $150K USD, with low operating costs, few specialised components, and low shielding requirements. These treatment machines, although likely not as effective as MV treatment machines, would avoid the estimated $5M USD price of a new linac and $2M USD additional cost of constructing the 2 metre thick cement bunker needed for safe operation of a linac.

## 1.4 Primary Contributions and Significance of the Work

Overall, the significance of this work lies in its comprehensive investigation of novel imaging techniques, simulation setup, and detector performance through the lens of lowering radiotherapy cost. The novel rapid simulation tool, Fastcat, is developed for image quality assessment and virtual clinical trials (VCTs). The work also does a preliminary investigation of novel low-cost perovskite detectors in VCTs using the Fastcat tool. These findings have implications for improving imaging accuracy and treatment planning. Finally, an investigation was undertaken to assess the effectiveness of lung SABR treatment using a low-cost kV radiotherapy machine with the goal of establishing a radiotherapy platform for LMICs. The findings contribute to the advancement of medical imaging technology and its potential impact on clinical practice, laying a groundwork for the future direction of low-cost radiotherapy treatments.

## 1.5 Structure of the Thesis

An overview of my PhD and how the different topics intersect is shown in Figure 1.2. Development and validation of the Fastcat hybrid MC code allows the simulation of novel CWO and Perovskite detectors. Likewise, Fastcat's simulation methods are applied to kV treatment planning and opti-

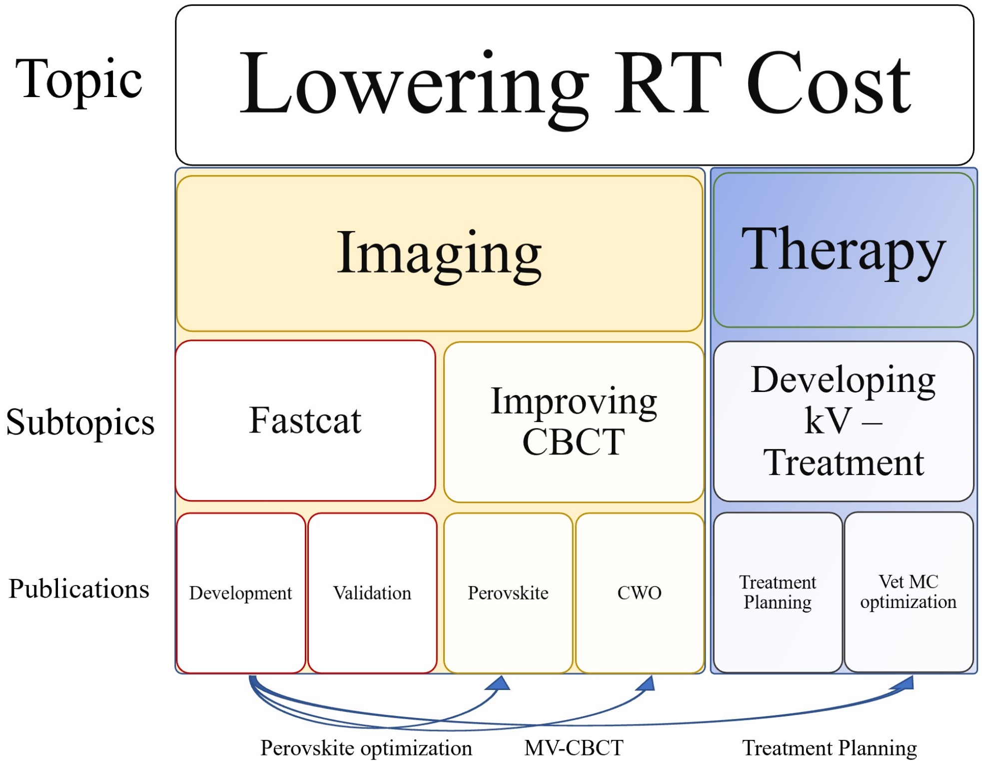

Figure 1.2: An overview of my PhD work and the relation between projects.

mization of the kV treatment machine's CBCT imaging system.

# Chapter 2

# Radiography and Radiotherapy Physics

In this chapter, we will briefly go over some of the fundamental principles behind radiography and radiotherapy from a physics perspective. We will explore the behavior of photons and electrons, their interactions with matter, and how these interactions are harnessed to achieve precise imaging and therapeutic outcomes.

## 2.1 Radiography and Radiotherapy Physics

Fundamentally, radiography and radiotherapy treatments are founded upon the properties and behaviors of fundamental particles, namely photons and electrons. These particles play a pivotal role in enabling us to visualize the human body with exceptional clarity and precision, as well as selectively target and destroy tumors while sparing healthy tissues.

Without the unique characteristics exhibited by photons and electrons, the remarkable view inside the human body provided by medical imaging would be unattainable, and the ability to effectively treat tumors through radiotherapy would be compromised. Thus, to accurately assess the applications of radiography and radiotherapy, it is essential to delve into the fundamental principles of physics that govern the behavior of these particles. By understanding the intricacies of photon and electron interactions at a fundamental level, we gain valuable insights that shape the field of medical physics. This knowledge forms the foundation for optimizing diagnostic imaging techniques, refining treatment planning strategies, and ultimately improving patient outcomes in the realm of healthcare.

## 2.2 Role of Photons in Medical Physics

Photons play a central role in both radiography and radiotherapy, serving as a primary tool in these fields. However, it is crucial to recognize the diversity within the broad spectrum of photon energies. While optical light and megavoltage x-rays are both photons, it would be misleading to lump them together without distinction. Each application, whether it be photon radiotherapy or a photomultiplier tube, is finely tuned to the specific properties of the respective photons. Interchanging these photons would lead to ineffective treatment and a lack of signal detection.

To provide a comprehensive understanding, we will begin by discussing the general properties of photons. We will then delve into their specific characteristics, highlighting the importance of photon energy in medical physics. When a photon encounters another particle, there is a probability of interaction, which varies depending on the photon's energy. The medical physicist's attention to photon energy stems from the significance of these interactions.

## 2.3 Photon Interactions

The nature of photons raises philosophical questions, as their properties, such as particle-wave duality, defy our everyday understanding of objects. If an ordinary chair were to behave like a photon, sitting down would become a risky proposition, with a probability that the universe would play a practical joke by moving the chair to another location, leaving us perplexed on the floor. Fortunately, we live in a world where chair positions are not subject to probability distributions, but the position of photons remains uncertain. Although many aspects of photons and fundamental particles are mysterious, we can still describe certain reliable properties and relationships although to simulate them fully (as we will see in later chapters) we will need to take into account their probabilistic nature.

Essential to a medical physicists understanding of photons is their propensity to interact with matter. Once a photon is generated with a given amount of energy, it travels at the speed of light on an endless trajectory, moving through the vast expanse of space unhindered if not for the presence of matter scattered throughout the universe. When matter is encountered by a photon, the energy it contained may be partially or fully transfer to the matter. Photon-matter interaction serves as the fundamental mechanism for energy and information transfer throughout the universe, forming the foundation of radiation therapy and radiography.

### Photon Interactions in Materials

Let us begin by emphasizing that the probability of a photon interacting with the constituent particles of a uniform medium in an infinitesimal distance $dx$ remains constant regardless of its travel distance through a material. Unlike a weary hiker, photons do not suffer from fatigue or blisters along their journey. Whether they have traveled 20 kilometers or 20 million kilometers, their likelihood of succumbing to an interaction remains the same. This property implies that, on a larger scale, if half of the initial number of photons reach a depth $x$ in a material, only a quarter will reach a depth of $2x$. The distribution of these particles follows an exponential pattern given by the equation:

$$N = N_0 \exp(-\mu x) \tag{2.1}$$

In the above equation, $N$ represents the number of photons, $N_0$ represents the initial number of photons, $x$ represents the depth within the material, and $\mu$ represents the linear attenuation coefficient [54, 55].

Similar to hikers, photons generally strive to leave minimal impact on the matter they interact with. While electrons may create a trail of ionized molecules, causing damage to the tissue, photons, known as "indirectly ionizing" particles, primarily induce damage to tumors through secondary electrons they produce, rather than through direct ionizations. Therefore, understanding electron interactions and their products is crucial in comprehending photon radiation therapy.

In this section we will introduce four fundamental processes: Rayleigh scattering, photoelectric effect, Compton scattering, and pair production. Rayleigh (coherent) scattering refers to the elastic scattering of a photon by an atom, causing a change in its direction without any energy transfer. The photoelectric effect involves the absorption of a photon by an atom, leading to the ejection of an electron. Compton (incoherent) scattering occurs when a photon collides with an electron, resulting in the photon's energy transfer and change in direction. Lastly, pair production involves the conversion of a photon into an electron-positron pair in the presence of a nucleus. The total mass attenuation coefficients for a few example materials can be seen in Figure 2.1. While the energy ranges in which the different effects dominate can be seen in Figure 2.2.

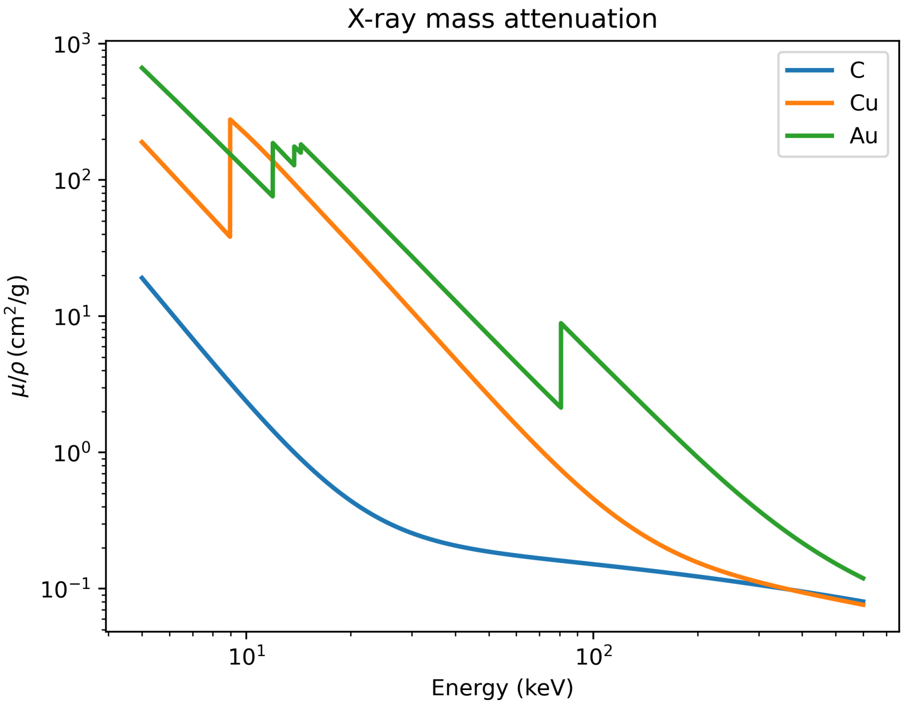

Figure 2.1: The total mass attenuation coefficients for carbon, copper, and gold in the kV range of energies.

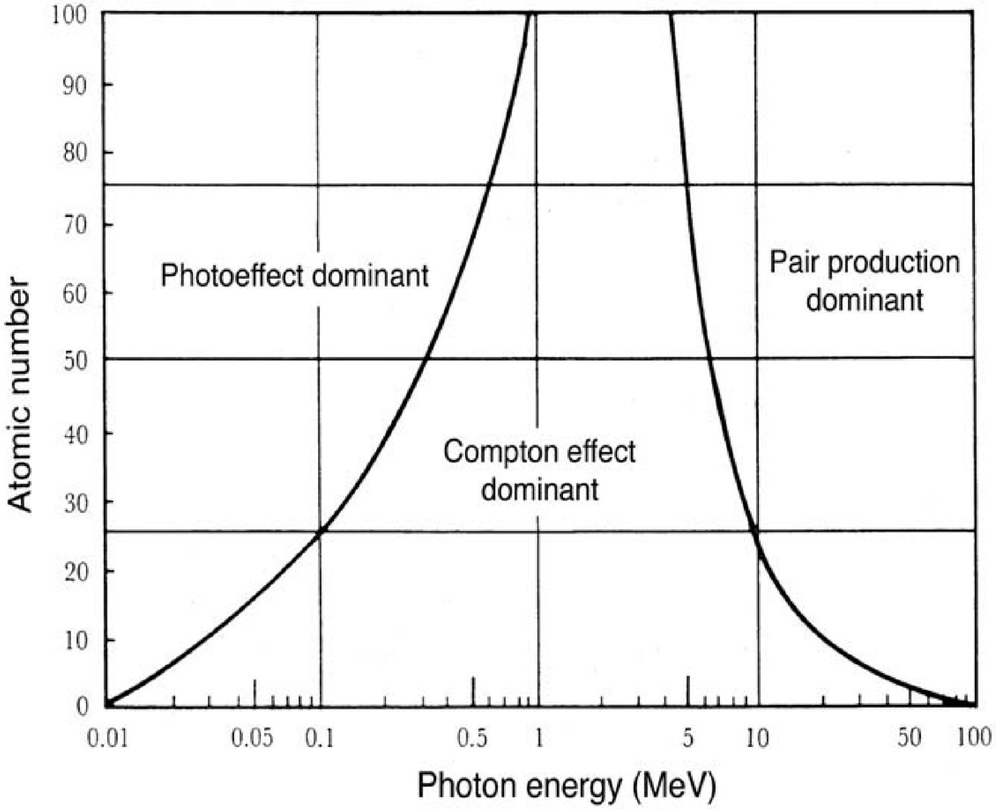

Figure 2.2: Regions of relative predominance of the three main forms of photon interaction with matter. The left curve represents the region where the atomic coefficints for the photoelectric effect and Compton effect are equal, the right curve is for the regio where the atomic Compton coefficient equals the atomic pair production coefficient [Reproduced from Podgorsak [56] with permission].

### 2.3.1 Rayleigh Scattering

The most basic of photon interactions is Rayleigh scattering, which is the most elastic of the photon interactions we will discuss it involves the interaction of a photon with an entire atom. The atom absorbs the photon and emits another photon with almost exactly the same energy, in a direction that is essentially isotropic around the interaction point. The Rayleigh scattering cross section scales as $(Z/E)^2$, where $Z$ is the atomic number and $E$ is the photon energy [56]. In biological materials at the energies used in radiography and radiation therapy, Rayleigh scattering is a minor interaction. Since minimal energy is transferred, Rayleigh scattering does not significantly contribute to treatment doses. However, the change in photon direction complicates the relationship between the intensity of a detector pixel and the composition of the material between the pixel and the source, a crucial aspect of radiographic imaging.

### 2.3.2 Compton Scattering

Compton scattering is a fundamental phenomenon wherein a photon interacts with an electron, leading to the alteration of the photon's trajectory and the recoil of the electron. This process holds great significance in the realm of radiotherapy as it gives rise to secondary electrons, which play a crucial role in the deposition of dose during treatment.

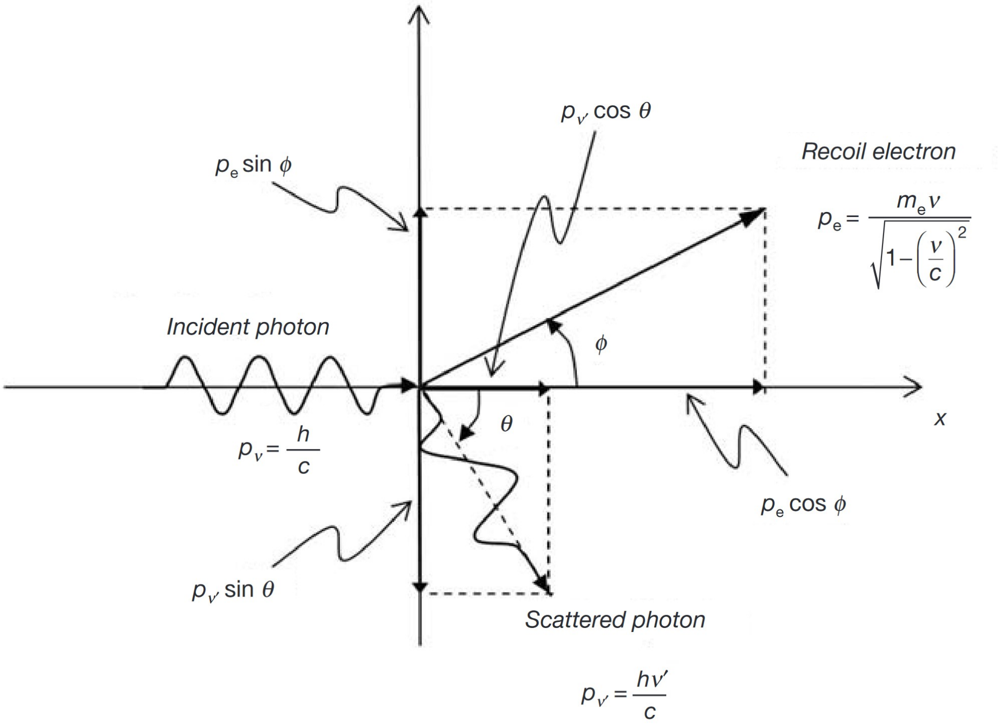

Figure 2.3: Schematic diagram of Compton scattering. An incident photon with energy $h\nu$ interacts with a lossely bound (essentially free) atomic electron. The electron is ejected from the atom as a recoil (Compton) electron with kinetic energy $E_K$ and a scattered photon with energy $h\nu' = h\nu - E_K$ is produced. [Reproduced from Podgorsak [56]. with permission]

Unlike Rayleigh scattering, which involves the scattering of photons by free atoms or molecules, Compton scattering occurs when photons interact with electrons bound loosely by atoms, as shown in the Figure 2.3 schematic. The exchange of energy and momentum between the photon and electron facilitates the scattering event. Consequently, the photon changes its direction, causing a disruption in radiographic signals and impacting image formation in various medical imaging techniques.

One notable distinction between Compton scattering and Rayleigh scattering lies in the substantial transfer of energy from the photon to the electron. As the photon interacts with the electron, a portion of its energy is transferred, resulting in the recoil of the electron. The scattered photon retains some energy, albeit with a longer wavelength compared to the incident photon. Notably, the energy transferred to the electron can be considerable, especially when dealing with high-energy photons employed in radiotherapy applications. The energy transfer in Compton scattering can be quantified using the Compton shift formula:

$$\Delta\lambda = \lambda' - \lambda = \frac{h}{m_e c}\left(1 - \cos(\theta)\right) \tag{2.2}$$

where $\Delta\lambda$ is the Compton shift, $\lambda'$ is the wavelength of the scattered photon, $\lambda$ is the wavelength of the incident photon, $h$ is the Planck constant, $m_e$ is the rest mass of the electron, $c$ is the speed of light, and $\theta$ is the scattering angle [56].

Furthermore, the probability of Compton scattering occurring within a specific solid angle can be calculated using the Klein-Nishina formula:

$$\frac{d\sigma}{d\Omega} = \frac{r_0^2}{2}\left(\frac{\lambda'}{\lambda}\right)^2\left(\frac{\lambda'}{\lambda} + \frac{\lambda}{\lambda'} - \sin^2\theta\right) \tag{2.3}$$

In this equation, $d\sigma/d\Omega$ represents the differential cross-section, $r_0$ is the classical electron radius, $\lambda$ is the wavelength of the incident photon, $\lambda'$ is the wavelength of the scattered photon, and $\theta$ is the scattering angle. The properties of Compton scattering, including the energy transfer to secondary electrons and the angular distribution of the scattered photons, are of utmost importance when considering patient treatments. The Compton interaction cross section (another name for an attenuation coefficient) is dependent on the electron density, and therefore $Z$, of the material; the interaction cross-section decreases with increasing beam energy.

### 2.3.3 The Photoelectric Effect

The photoelectric effect is a crucial phenomenon in which a photon, generally in the keV range can be completely absorbed by an atom, leading to the excitation of the target atom and the emission of an orbital electron as well as a characteristic x-ray or a Meitner-Auger electron. The energy of the emitted electron is equal to the difference between the energy of the incident photon and the binding energy of the electron.

A notable characteristic of the photoelectric effect is the presence of absorption edges and spectral peaks when the photon energy matches the binding energy of an atomic shell. At these specific energies, the probability of interaction and the cross-section increase significantly. The differential cross-section exhibits distinct peaks, corresponding to the absorption edges, indicating the strong interaction between the photon and the atom at those energies.

It is important to note that the photoelectric cross-section is proportional to Z to the power of four ($Z^4$) and inversely proportional to the photon energy ($E^3$). This dependency explains the enhanced significance of the photoelectric effect in high-$Z$ materials, such as shielding and collimating components in accelerators. Additionally, in low-energy applications like diagnostic x-ray beams, the photoelectric effect is more prominent compared to clinical megavoltage (MV) beams, where other processes dominate.

Understanding the physics of the photoelectric effect provides insights into the behavior of photons interacting with matter, offering valuable knowledge for various fields, including medical imaging and radiation therapy. By comprehending the intricacies of this phenomenon, researchers can optimize imaging techniques, design shielding materials, and develop accurate dose calculations, contributing to advancements in medical physics and related disciplines.

### 2.3.4 Pair and Triplet Production

As photon energies surpass the critical energy of $2m_ec^2 = 1.02, \mathrm{MeV}$ in megavoltage radiotherapy, two additional interactions emerge. Pair production involves a photon interacting with a nuclear Coulomb field, resulting in the absorption of the photon and the creation of an electron-positron pair as seen in Figure 2.4. Triplet production, occurring at twice the energy threshold of pair production, involves an interaction within the field of an orbital electron and leads to the emission of an additional orbital electron. Both pair and triplet production produce positrons, which annihilate and generate two $0.511, \mathrm{MeV}$ photons that typically escape the patient, thus not significantly contributing to patient dose.

#### Summary

A summary of the different properties of the interactions is seen in Table 2.1.

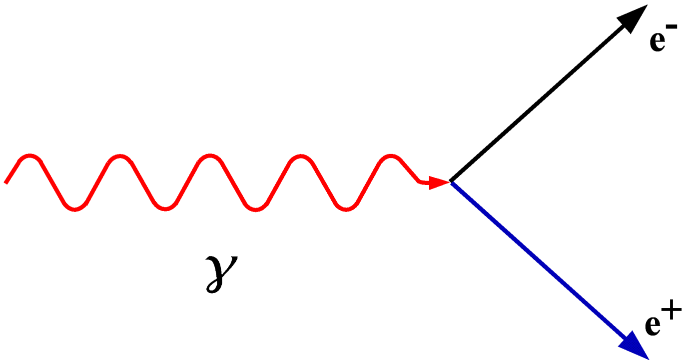

Figure 2.4: A schematic of the incident photon ($\gamma$) hitting a Coulomb field and producing an electron ($e^-$) and a positron ($e^+$).

### 2.3.5 Electron Interactions

In the realm of clinical practice, it is important to note that this thesis does not involve direct electron treatment of the patient. Instead, the patient is subjected to photon irradiation, which gives rise to secondary electrons as byproducts.

In contrast to photons, which dissipate their energy generously, electrons exhibit a more conservative behavior, preferring numerous smaller energy exchanges. It is not uncommon for electrons to

Table 2.1: Main characteristics of the different photon interactions. [As appears in Podgorsak [56]]

| | Photoelectric Effect | Rayleigh scattering | Compton effect | Pair production |
|---|---|---|---|---|
| Photon interaction | With whole atom (bound electron) | With bound electrons | With free electrons | With nuclear Coulomb field |
| Mode of photon interaction | Photon disappears | Photon scattered | Photon scattered | Photon disappears |
| Energy dependence | $\frac{1}{(hv)^3}$ | $\frac{1}{(hv)^2}$ | Decreases with energy | Increases with energy |
| Threshold | No | No | No | $2m_ec^2$ |
| Linear attenuation coefficient | $\tau$ | $\sigma_R$ | $\sigma_C$ | $\kappa$ |
| Particles released | Photoelectron | None | Compton (recoil) electron | Electron-positron pair |
| Atomic coefficient dependence on $Z$ | ${}_a\tau \propto Z^4$ | ${}_a\sigma_R \propto Z^2$ | ${}_a\sigma_C \propto Z$ | ${}_a\kappa \propto Z^2$ |
| Mass coefficient dependence on $Z$ | $\frac{\tau}{\rho} \propto Z^3$ | $\frac{\sigma_R}{\rho} \propto Z$ | Independent | $\frac{\kappa}{\rho} \propto Z$ |
| Subsequent effect | Characteristic X ray, Meitner effect | None | Characteristic X ray, Meitner effect | Annihilation radiation |
| Significant energy region for water | $< 20$keV | $< 20$keV | 20keV$-$ 10MeV | $> 10$MeV |

traverse merely a fraction of a millimeter before engaging in interactions with other electrons and atomic nuclei. As the electron gradually loses energy, a realization dawns upon it—much like our own introspection as we near the conclusion of our unpredictable journey through life—that interactions with the surrounding environment carry greater significance than initially surmised. Consequently, the electron begins to allocate more energy to each interaction before eventually reaching a state of rest. This phenomenon can be quantified by expressing the stopping power of electrons, which increases as their energy decreases.

Furthermore, we identify two distinct components that contribute to the electron stopping power: radiative and collisional interactions. These discrete aspects govern the intricate dynamics that underlie the dissipation of electron energy within the tissue.

### Collisional Interactions

Collisional interactions involve the electron's encounters with charged particles present in the tissue, such as atomic nuclei and other electrons. These collisions lead to energy transfer between the electron and the target particles. The energy transfer can result in various processes, including excitation or ionization of atoms, leading to the production of additional secondary electrons or the emission of characteristic X-rays. The energy loss per unit path length $S_{\text{col}}/\rho$ due to collisional interactions can be described by the Bethe-Bloch formula:

$$\frac{S_{\text{col}}}{\rho} = \frac{4\pi N_A Z}{A} \frac{r_e^2 m_e c^2}{\beta^2} z^2 \left[ \ln \frac{2 m_e v^2}{I} - \ln(1-\beta^2) - \beta^2 - \frac{C}{Z} \right] \tag{2.4}$$

where $\beta = \frac{v}{c}$ is the usual ratio of the particle velocity to the speed of light ($c = 2.998 \times 10^8$ m/s), $r_e$ is the classical electron radius ($2.818 \times 10^{-15}$ m), $N_A$ is Avogadro's number ($6.022 \times 10^{23}$), $Z$ is the atomic number (number of protons in the nucleus), $A$ is the atomic mass number (number of nucleons), $z$ is the projectile charge, $I$ is the mean excitation potential ($I \propto Z$), and the ratio $\frac{C}{Z}$ is the shell correction factor [56, 55].

### Radiative Interactions

Radiative interactions play a significant role in the energy dissipation of electrons. As an energized electron traverses the tissue, it can emit photons through the process of bremsstrahlung, or braking radiation. This emission occurs when the electron experiences the influence of atomic nuclei, causing it to decelerate and emit electromagnetic radiation in the form of bremsstrahlung photons. The energy carried away by these emitted photons does not contribute to the local energy deposition within the tissue and has implications for dose distribution during radiotherapy. Mathematically, the mass radiative stopping power ($S_{\text{rad}}/\rho$) due to radiative interactions can be described by the Bethe-Heitler formula:

$$\frac{S_{\text{rad}}}{\rho} = \sigma_o \frac{N_A Z^2}{A\rho}(E_k + m_e c^2)\bar{B}_r \tag{2.5}$$

where $\sigma_o$ is a constant ($5.80 \times 10^{-28}$ cm$^2$/atom), $\bar{B}_r$ is a function of $Z$ and $E_k$, the electron kinetic energy. The relationship between the mass radiative stopping power $S_{\text{rad}}/\rho$) and the kinetic energy of an electron is responsible for the increasing significance of Bremsstrahlung production at higher electron beam energies. Additionally, the $Z^2$ term in the equation explains why the radiative interaction becomes more dominant in materials with higher atomic numbers [56].

The interplay between radiative and collisional interactions governs the intricate dynamics of electron energy deposition within the tissue. Understanding the contributions of these interactions provides a foundation for optimizing treatment planning, dose delivery, and overall treatment outcomes in the realm of clinical medical physics.

## 2.4 Medical Imaging Physics

In contrast to other imaging modalities like MRI or ultrasound, radiography relies on multiple interactions between photons and matter, as discussed previously, to generate an image. The composition of the imaged object influences the specific proportions of these interactions, resulting in variations in the generated image. Complicating matters further, x-rays, unlike other modalities, deposit ionizing radiation in tissues, increasing the patient's risk of cancer. In an ideal scenario, we would employ long exposures of low-energy photons to achieve high-resolution, MRI-like image quality. However, x-ray imaging protocols must adhere to the "as low as reasonably achievable" (ALARA) principle to limit patient dose, necessitating modifications from the ideal approach.

While much of the field of diagnostic radiology may be qualitative; interpreting an x-ray image of a fractured bone or a CT-slice of a lung lesion where qualitative differences in appearance of anatomy are adequate for diagnosis. In radiation oncology we differ from these qualitative observables, looking instead for CT to give quantitative attenuation coefficients and in turn electron densities essential to proper treatment planning. Quantitative attenuation coefficients can be found theoretically but can generally only be approximated in a clinical setting:

Imagine an idealized imaging system that aims to provide perfect attenuation coefficients of the human body. This perfect system might include a synchrotron monoenergetic source that emits a tightly collimated pencil beam, while two collimators are strategically placed to reject any scattered photons. To minimize motion artifacts, the pencil beam rotates rapidly around the patient during image acquisition. This setup effectively addresses the challenges posed by the polyenergetic nature of attenuation coefficients in computed tomography (CT) and the confounding effects of scatter and would give you a nearly exact map of a human's attenuation coefficients. Unfortunately, synchrotron sources are prohibitively expensive and collimation reduces the efficiency of acquisition making practical imaging solutions different from this, by examining existing imaging system relative to this ideal system that gives perfect attenuation coefficients we can get a good idea of the strengths and weaknesses of CT imaging systems.

The imaging workflows discussed in this dissertation deviate from this idealized scheme, introducing artifacts that can affect image quality. The focus of this thesis is often on CT systems which utilizes a polyenergetic x-ray beam generated by an x-ray tube with a peak energy of approximately 100 keV. Aluminum filtering is employed to remove low-energy photons. The beam takes on a conical or fan shape, providing a larger detection area, and a 2D grid above the detector helps mitigate scatter. To understand the effects of this cone-beam CT geometry on the values that make up a CT image, and how they differ from idealized attenuation coefficients we will examine the image formation process.

### 2.4.1 X-Ray Projection Image Acquisition

A digital radiographic image is composed of three images: The first is what is called a flat field image, taken by irradiating the detector without any object present, the second is the dark field an image capturing the detector output without any radiation and the third is the image of the object. We then create a projection image (P) as

$$P = -\ln \frac{I - I_d}{I_o - I_d} \tag{2.6}$$

Where $I_o$ is the field image, $I_d$ is the dark field image and $I$ is the image of the object [54]. This projection image is an approximation of the attenuation for each ray between the course and detector pixel since

$$I - I_d = (I_o - I_d)\exp(-P) \tag{2.7}$$

So we can see that each pixel of the image is an approximating the path length times the average attenuation coefficient ($-\mu x$) between each detector pixel and the source. For an object of uniform composition and a monoenergetic x-ray source, $\mu x$ is the linear attenuation of the material, if we then know the path length we can find $\mu$ and we can look up the attenuation coefficient in the NIST database of x-ray coefficients to ascertain what sort of material that we are looking at. But what is the fun of taking an x-ray image of a uniform object? For a varied and interesting object the projection image is the sum of attenuation coefficients along the ray

$$P_{i,j,\theta} = \mu_1 x_1 + \mu_2 x_2 + \ldots + \mu_n x_n \tag{2.8}$$

In the case of projection radiography generally we have $\mu_{bone} >> \mu_{tissue}$ and the projection image is useful at examining bony anatomy as the rays interacting with bone are obvious compared to any voxels without bony anatomy. However, this approach is less effective when attenuations are similar [54].

In medical imaging, interpreting images with only fat and muscle can sometimes be challenging due to the similarity in their linear attenuation coefficients. This ambiguity arises when two different combinations of fat and muscle can produce the same image value, making it difficult for the viewer to distinguish between them. The complexity escalates with the use of polyenergetic x-ray beams, where attenuation coefficients encompass a range of x-ray energies. Consequently, establishing a relationship between the projection radiographic image value and the attenuation coefficient becomes unattainable as we must solve for an integration over energy to find $\mu(E', x)$

$$I(E) = \int \left[ I_0(E) \cdot \exp\left( - \int [\mu(E', x) \cdot dx] \right) \right] \cdot S(E, E') \cdot dE'$$

Here, $I(E)$ represents the intensity of the X-ray beam at energy $E$ after passing through the tissue. $I_0(E)$ represents the initial intensity of the X-ray beam at energy $E$. $\mu(E', x)$ represents the energy-dependent linear attenuation coefficient of the tissue, which varies with the energy $E'$ of the X-rays and the path length $x$. $S(E, E')$ represents the spectral distribution of the X-ray beam, describing the relative number of X-rays at different energies. The integral is taken over the entire energy spectrum of the X-ray source [55, 57].

The relationship between the image value and tissue composition is determined by the energy-dependent attenuation coefficients and the spectral distribution of the X-ray beam. The different attenuation properties of tissues at various X-ray energies, as well as the energy spectrum of the X-ray source, influence the image values. This complexity in quantifying attenuation coefficients and localizing patient anatomy in 3D space leads to the utilization of computed tomography (CT), which offers a more precise and comprehensive solution. CT imaging helps overcome the limitations of projection radiography, enabling accurate differentiation of materials with similar attenuation and providing detailed spatial information for treatment planning in radiotherapy.

### 2.4.2 CT imaging

Computed tomographic (CT) imaging is a natural extension of x-projection radiography the like of which you may encounter at the dentist on a semi-annual basis. While the extension of your teeth's bony roots into your jaw is readily answered by projection radiography, the ultimate question of the different bodily organ's position relative to each other requires a more analytical approach: This analytic approach which is fundamentally computerized is called CT and is essential to image guided radiotherapy and medical diagnostics generally.

In CT imaging, we introduce dynamic rotation of the traditional projection radiography setup around the patient's axial axis. Both the source and the detector rotate in synchrony, positioned on opposite sides of a stationary patient. At the heart of this rotation lies the isocenter, a central point between the detector and source, which assumes significance in the subsequent computerized reconstruction process.

During the rotation, we acquire a series of projection images at equally spaced intervals around the object. Unlike projection radiography, where the distinct attenuation coefficients of various lengths ($x_i$) remain indistinguishable due to the limited information contained in each ray, the multitude of acquired projection images enables us to solve for the unknowns and derive attenuation values at different points within the volume. This is achieved through a system of linear equations:

$$P_{i,j,\theta} = \mu_1 x_1 + \mu_2 x_2 + \ldots + \mu_n x_n \tag{2.9}$$

While filtered back projection is the most computationally efficient approach, recent years have witnessed a proliferation of alternative image reconstruction methods, facilitated by increased computational power.

In computed tomography (CT), the underlying mathematical relationship between the acquired projection data and the unknown distribution of linear attenuation coefficients within the imaged object is the focal point. This relationship is expressed by the Radon transform, characterized by the equation:

$$P(\theta, s) = \int\int f(x, y) \cdot \delta(\theta - \theta') \cdot \delta(s - x\cos(\theta') - y\sin(\theta')) \cdot dx \cdot dy \tag{2.10}$$

Here, $P(\theta, s)$ represents the measured projection data at angle $\theta$ and position $s$, $f(x, y)$ denotes the unknown distribution of attenuation coefficients, while $\delta(\theta - \theta')$ and $\delta(s - x\cos(\theta') - y\sin(\theta'))$ are the Dirac delta functions that impose constraints on the integration over the object.

The ultimate goal of CT reconstruction algorithms is to solve this equation and estimate the distribution of attenuation coefficients $f(x, y)$ within the imaged object based on the measured projection data $P(\theta, s)$. By unraveling the internal structures and tissue properties with enhanced precision, CT imaging allows a 3d reconstruction of the internal anatomy of the patient to be achieved. CT systems include a source and a detector rotating about an object as seen in Figure 2.5 [57].

### 2.4.3 X-ray Tubes

Radiography, the technique of using x-rays for imaging, poses a unique challenge due to the nature of x-ray production. While producing optical light is relatively straightforward through processes like heating tungsten filaments or exciting gases, generating x-rays requires much higher energies. Ordinary power supplies used in electronics, such as those driving LCD displays or motors, are insufficient for x-ray production. To create the conditions for high-energy electrons and subsequently high-energy photons, thousands to hundreds of thousands of volts are needed.

In an x-ray tube, which is a rather inefficient system, a tungsten anode is heated to generate ionization events that produce electrons. These electrons are then accelerated through a high voltage potential towards an angled tungsten cathode. X-rays, initially called "Cathode rays," are emitted

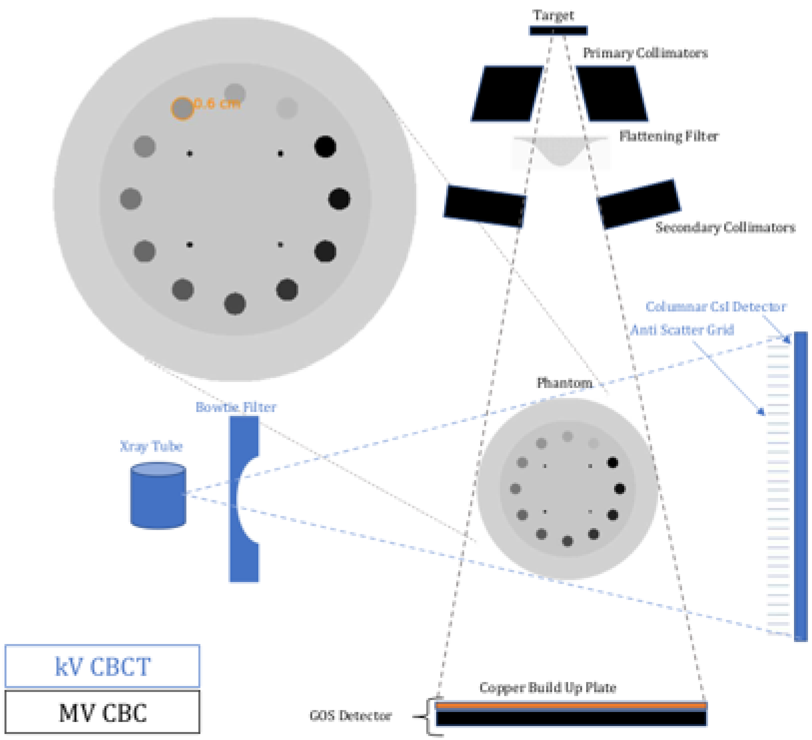

Figure 2.5: A kV and an MV setup are shown. The kV setup using an x-ray tube while the MV setup uses a linac head.

from the cathode through a process called bremstrahlung and photoelectric interactions. High-energy electrons are accelerated towards a target material, typically tungsten, leading to interactions that result in the emission of x-rays. X-rays are generated through two primary mechanisms: bremsstrahlung and the photoelectric effect. These electronics are housed in an evacuated glass envelope, while the anode may be stationary or may rotate to better dissipate heat. A rotating anode x-ray tube is shown in Figure 2.6.

When assessing an x-ray tube, several design variations are relevant to medical physicists. Firstly, the peak voltage supplied, often denoted as ”kVp” (kilovoltage peak), represents the maximum possible energy of the x-rays. However, the mean energy of the x-ray beam will typically be about half of this value in practice. Secondly, the tube current available at the peak voltage, which determines the tube’s photon output, is analogous to the light level in conventional photography. In medical imaging, exposure is defined as the tube current multiplied by the exposure time. Longer exposures are required for clear image resolution, similar to conventional photography. Similarly, for capturing moving objects, such as in sports photography, bright lighting and short exposures are needed to prevent motion blur. The same principle applies to moving anatomy, like the lungs, where high current and short image acquisition times may result in blurred images.

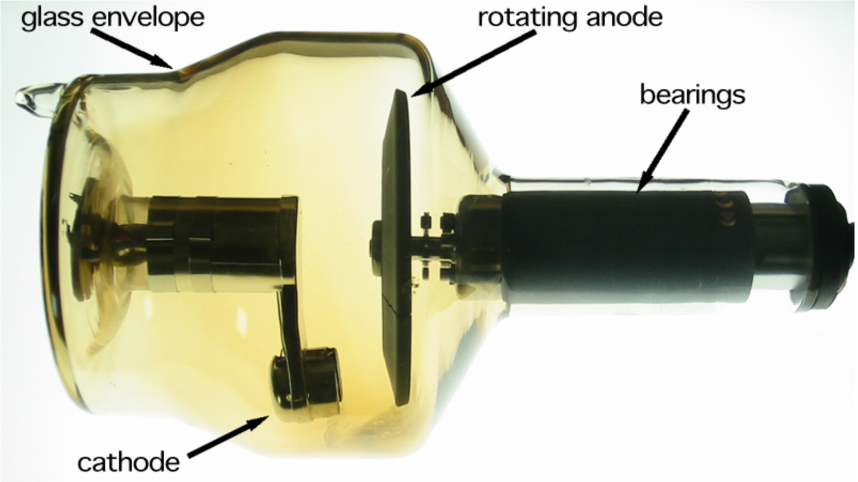

Figure 2.6: A rotating anode x-ray tube is shown with key parts labelled. [58] [Reproduced from Wikimedia by Daniel W. Rickey, CC BY-SA 3.0]

Third, the focal spot size of the x-ray tube is an important factor in determination of image sharpness as one can determine when trying to make shadow puppets, the experience shadow puppeteer will choose a candle or LED light which emit from a small point lending sharp lines to their puppetry while a less experienced puppeteer may choose an incandescent light which acts to blur the lines of their puppets and be unimpressive to any watching children. A schematic of this effect can be seen in Figure 2.7.

### 2.4.4 Focal Spots

Similarly, small focal spots act to sharpen images while large focal spots decrease the spatial resolution and make them unimpressive to any watching radiologists. The focal spot blur in radiography can be described by the point spread function (PSF), which characterizes the spatial distribution of radiation intensity around the focal spot. One common model used to represent the PSF is the Gaussian function. The equation for the Gaussian PSF is:

$$PSF(x,y) = \frac{1}{2\pi\sigma_x\sigma_y} \cdot e^{-\frac{x^2}{2\sigma_x^2}-\frac{y^2}{2\sigma_y^2}} \tag{2.11}$$

where $x$ and $y$ are the coordinates in the image plane, $\sigma_x$ and $\sigma_y$ represent the standard deviations of the Gaussian distribution in the $x$ and $y$ directions, respectively. The blurriness of the focal spot increases as the standard deviations $\sigma_x$ and $\sigma_y$ increase, indicating a larger spread of radiation intensity around the focal spot. The PSF is convolved with the image to account for the blurring effect of the focal spot in the final image [55, 57].

For different medical imaging applications it may be useful to have different combinations of focal spot, current and kVp. We must keep in mind though the dose rate is roughly proportional to the

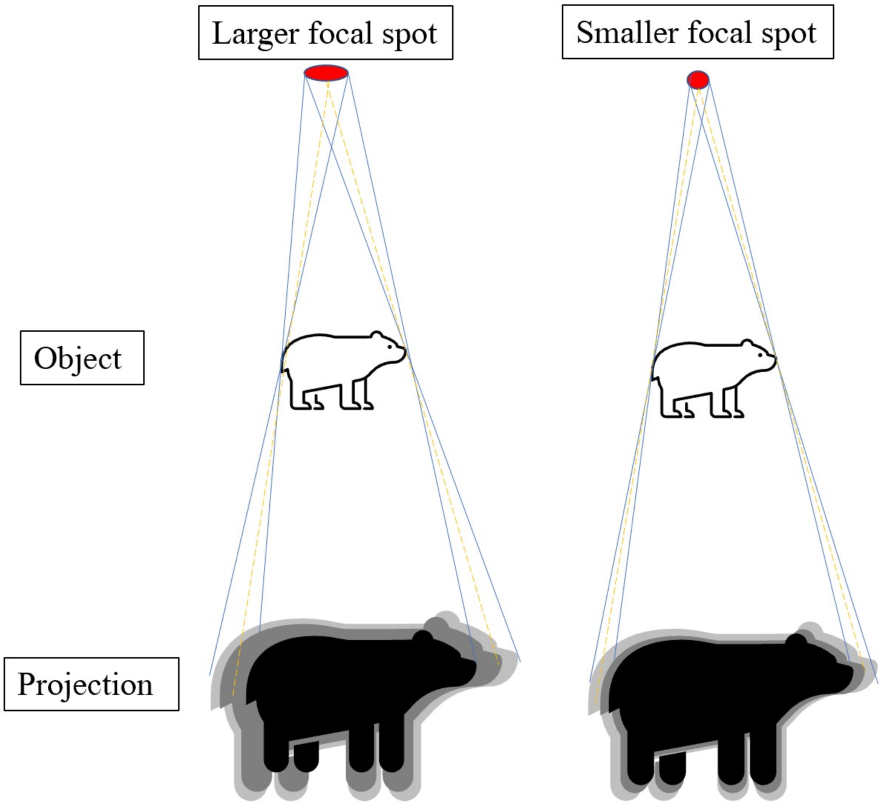

Figure 2.7: A schematic of the increased blurryness to to geometric blurring from the focal spot.

power requirement for the dose rate of the device which scales linearly with the current $(I)$ and quadratically with the voltage $(V)$. In turn, decreasing the focal spot focuses the beam on a small area on the anode, heating the anode rapidly and necessitating expedient cooling systems in the device: Mammography tubes as they operate at low voltage for short periods of time (ms) and low voltages allows for very small focal spot sizes and in turn high resolution images suited for breast calcification detection. CT scanners, on the other hand, generally operate at high current, with kVps over double that of mammography systems, as well as beam filtration necessitating larger focal spots to deliver adequate fluence without overheating the anode. In the context of kilovoltage radiotherapy very high kV sources can be used at high currents with large focal spots as focal spot blur is not as important to treatment dose distributions as it is to image resolution.

### 2.4.5 Additional Components

In the field of medical imaging, several essential components play a crucial role in optimizing image quality and reducing imaging artifacts. Bowtie filters, beam hardening filters, and anti-scatter grids are three such components that contribute significantly to the overall imaging process [54].

Bowtie filters are designed to shape the photon energy spectrum of the imaging beam, helping to compensate for variations in patient thickness. By attenuating the beam intensity towards the periphery and reducing it towards the center, bowtie filters ensure more uniform exposure across the patient. This modification of the photon energy spectrum helps in minimizing image artifacts such as beam hardening, where high-density structures can appear inaccurately dense due to the polychromatic nature of X-ray beams.

Beam hardening filters are specifically employed to address the beam hardening phenomenon. These filters consist of materials that preferentially attenuate low-energy photons, reducing their contribution to the overall beam spectrum. By selectively attenuating the low-energy X-ray photons, beam hardening filters help to mitigate beam hardening artifacts and improve image accuracy and clarity. For the Varian OBIs discussed in this work beam hardening filters generally consist of about 0.7 mm of titanium.

Anti-scatter grids are utilized to minimize the amount of scattered radiation reaching the X-ray detector. Scatter radiation can degrade image quality by reducing contrast and introducing unwanted noise. Anti-scatter grids generally consist of a series of lead strips or septa that absorb scattered radiation while allowing primary radiation to pass through. By absorbing scattered photons, anti-scatter grids enhance image contrast and minimize the occurrence of scatter-related artifacts [54].

### 2.4.6 X-ray Detectors

As early 1900s scholars would tell you, the spintheroscope is considered the best tool to visualize radiation. Like other indirect detector systems, a spintheroscope consisted of a photoconversion step and a photodetection step. In this case, a scintillating crystal was typically used as the photoconversion step, producing optical photons when exposed to high-energy radiation. The photodetection step involved a graduate student positioned behind a magnifying lens to manually count the photons. Hence, one could argue that the earliest x-ray detector known to science was the humble graduate student.

Since the early 1900s, technological advancements have replaced the graduate student with digital counterparts in most applications. In the case of CT detectors, a digital readout has always been necessary for computational reconstruction. Early models used large photomultiplier tubes (PMTs), which have now been largely replaced by amorphous silicon (aSi) semiconductors for readout purposes. Throughout the past century, various detection methods, whether involving graduate students, PMTs, or aSi semiconductors, have always relied on scintillators to convert x-rays into optical light. More recently, solid-state direct conversion detectors have gained popularity in diagnostic imaging, offering an alternative to scintillator-based systems.

### 2.4.7 Scintillating Detectors

As mentioned earlier, scintillating detectors undergo two distinct steps in the image acquisition process: photoconversion and photodetection. In the photoconversion step, incident high-energy photons or electrons interact with the atoms of the material, causing the release of electrons into the material's valence shell and generating electron-hole pairs. These electron-hole pairs then migrate to luminescence centers within the material, leading to the emission of light. When it comes to scintillators, certain properties are desirable. Firstly, high photon output is preferred, ensuring that a large number of optical photons are produced per incident x-ray. Additionally, fast scintillation is advantageous, minimizing the time delay between x-ray absorption and the emission of optical photons. Another desirable property is intrinsic collimation within the material. Since light is emitted isotropically from the luminescence centers in the crystal, it is crucial that the spatial information encoded by the point of interaction is not obscured by the scattering of optical photons throughout the material. Two commonly used detectors in x-ray imaging are CsI and GOS, each with their own specific properties, which are outlined below [54]:

### 2.4.8 Semiconductor Detectors

Unlike scintillating detectors, semiconductor detectors are based on direct conversion and do not rely on the generation of optical photons for detection. Instead, a voltage is applied across the detector crystal, and the electron-hole pairs created by incident radiation move across the potential gradient and are collected in a capacitor until readout. Direct conversion detectors typically offer higher spatial resolution and conversion efficiencies compared to scintillating detectors, as there is no additional step of converting the radiation to optical photons and no chance of optical photon spread. However, the manufacturing of direct conversion detectors is generally costly and more complicated than that of scintillators and there exist fewer materials with the correct properties for direct conversion than scintillation.

## 2.5 Image Quality Metrics

Image quality metrics play a crucial role in evaluating the performance and fidelity of medical imaging systems. Two key metrics are contrast and noise.

### 2.5.1 Basic Metrics

Contrast is a measure of the distinguishability of different structures or objects within an image. In the context of computed tomography (CT), contrast is often defined as the ratio of the signal in a region of interest (ROI) to the signal of a reference material, such as water, in the same image.

Image quality metrics play a crucial role in evaluating the performance and fidelity of medical imaging systems. Two key metrics are contrast and noise [55].

Contrast is a measure of the distinguishability of different structures or objects within an image. In the context of computed tomography (CT), contrast is often defined as the ratio of the signal in a region of interest (ROI) to the signal of a reference material, such as water, in the same image.

Noise, on the other hand, refers to the random variations or fluctuations in pixel intensities within an image. It is typically quantified by calculating the standard deviation of pixel values in a homogeneous region. A common metric to assess image quality is the signal to noise ratio (SNR), which represents the ratio of the signal level to the standard deviation of the noise. For CT imaging, the SNR can be calculated as:

$$SNR = \frac{\mu_{ROI}}{\sigma_{ROI}} \tag{2.12}$$

where $\mu_{ROI}$ refers to the mean intensity within an ROI and $\sigma_{ROI}$ corresponds to the standard deviation of pixel intensities in a noise ROI. Likewise, the contrast-to-noise ratio (CNR) combines the contrast and noise measurements to provide a comprehensive assessment of the differentiability of a material to water in a CT image [55]. CNR is defined as:

$$CNR = \frac{\mu_{ROI} - \mu_{water}}{\sigma_{ROI}} \tag{2.13}$$

Where $\mu_{ROI}$ and $\sigma_{ROI}$ are the mean and standard deviation of each ROI.

### 2.5.2 Spatial Resolution Metrics

Below are some common spatial resolution metrics mentioned in the dissertation which we describe and define formally here.

#### Modulation Transfer Function

In addition to contrast and noise, spatial resolution is a crucial aspect of image quality. The modulation transfer function (MTF) is a widely used metric to quantify spatial resolution. It characterizes the ability of an imaging system to preserve the contrast of high-frequency components in an image. The MTF can be obtained by calculating the Fourier Transform of the line spread function (LSF) and taking the magnitude of the resulting complex values. In the context of medical imaging, the line spread function (LSF) describes the response of an imaging system to a line source or a line-like object. It characterizes how the system blurs or spreads the line source in the resulting image. Mathematically, the MTF (M(f)) at a specific spatial frequency (f) can be defined as:

$$M(f) = \left| \frac{\mathcal{F}\{\text{LSF}\}(f)}{\mathcal{F}\{\text{LSF}\}(0)} \right|$$

Here, $\mathcal{F}$ represents the Fourier Transform operator. The LSF is Fourier transformed, and the magnitude of the complex values at frequency f is divided by the magnitude at zero frequency to normalize the MTF [5].

### Noise Power Spectrum

In medical imaging and signal processing, the noise power spectrum (NPS) is a valuable tool for characterizing and analyzing the noise properties present in an image or signal. It provides a quantitative description of the noise distribution across different spatial frequencies. The NPS is defined as the Fourier amplitude of a two dimensional image with intensity $I$ as

$$NPS(\mu_n, \nu_k) = \lim_{N_x, N_y \to \infty} (N_x N_y \Delta x \Delta y) |\mathcal{F}_{n,k}[I(x,y) - \bar{I}]|^2 \tag{2.14}$$

Where $I(x,y)$ is the image intensity at the pixel location $(x,y)$, $\mathcal{F}_{n,k}$ is the two dimensional Fourier transform where $n$ and $k$ are indices for the specific spatial frequency being sampled, $\bar{I}$ is the mean intensity of the image, $\nu$ and $\mu$ are the spatial frequencies conjugate to $x$ and $y$, while $\Delta x$ and $\Delta y$ are the pixel pitch of the detector and $N_x$, $N_y$ are the number of pixels in the $x$ and $y$ direction, respectively [55].

### Detective quantum efficiency

The detective quantum efficiency (DQE) of a detector is a metric that measures the degradation of the information contained in an output signal relative to the original input signal. Since detectors have physical limitations determined by Poisson statistics and finite pixel size, the DQE is measured relative to the ideal detector which is only limited by these factors. The work of Ranger *et al.* was followed to calculate the DQE [59]. Formally DQE is calculated as:

$$DQE(\nu) = S^2 \frac{MTF^2(\nu)}{NPS(\nu) \times q \times E} = \frac{MTF^2(\nu)}{NNPS(\nu) \times q \times E} \tag{2.15}$$

Where $MTF(\nu)$ is the frequency-dependent $MTF$, $NPS(\nu)$ is the frequency-dependent noise power spectrum ($NPS$), $S$ is the square of the large-area signal intensity. This equation can be simplified by using the $NNPS$ which is the noise power spectrum divided by the large-are signal intensity squared. Meanwhile, the $q$ value is an estimate of the number of incident x-ray photons per unit area per unit of exposure incident on the detector generally estimated through computer modelling. Finally, $E$ is the IEC-defined normal exposure [60].

## 2.6 Machine Learning in Medical Physics

A very brief introduction to deep learning is given for some context on the medical applications presented in chapter 7.

### 2.6.1 Deep Learning

Machine learning, a subset of artificial intelligence, is a field that focuses on developing algorithms and models capable of learning from data and making predictions or decisions without being explicitly programmed. At the core of machine learning lies the concept of a neuron, inspired by the functioning of biological neurons in the human brain.

A neuron typically takes multiple input signals, applies weights to them, and passes the sum through an activation function to produce an output. By adjusting the weights and the activation function, a neuron can learn to perform specific tasks, such as pattern recognition or classification. Multiple neurons can be connected to form a multi-layer perceptron (MLP), which enables more complex computations and higher-order representations.

Deep learning, an advanced branch of machine learning, takes the concept of MLPs further by introducing deep neural networks with multiple hidden layers. These deep networks allow for the automatic extraction of hierarchical features from data. Each layer in the network learns increasingly abstract representations, building upon the previous layers' output. This hierarchical representation learning enables deep neural networks to capture intricate patterns and relationships in data.

### 2.6.2 Medical Deep Learning Models

Machine learning has emerged as a powerful tool in the field of medical imaging, revolutionizing various aspects of diagnostic and therapeutic practices. Generative adversarial networks (GANs) have gained significant attention in recent years [61]. GANs utilize a generative model that can generate realistic data by learning from a large dataset. In medical imaging, GANs have shown promise in tasks such as image synthesis, denoising, and super-resolution, enabling the generation of high-quality images with improved details and reduced artifacts [62, 63, 64, 65].

Another notable advancement in medical imaging is the adoption of UNET models [66]. UNET is a deep learning architecture that leverages an encoder-decoder structure to perform image segmentation tasks. It has gained popularity due to its ability to accurately segment anatomical structures and abnormalities within medical images [67, 66]. UNET models have demonstrated remarkable performance in applications such as tumor segmentation, organ delineation, and lesion detection, enabling faster and more precise diagnosis and treatment planning [68].

Moreover, there has been growing use of auto-segmentation in medical imaging through machine learning techniques. Auto-segmentation utilizes algorithms that automatically delineate regions of interest within medical images, reducing the time and effort required for manual segmentation. Machine learning-based auto-segmentation methods, when trained on large datasets, can achieve high accuracy and consistency in segmenting structures, enhancing treatment planning efficiency and reducing inter-observer variability [68].

These advancements in machine learning and auto-segmentation have also found their way into clinical radiation oncology. The integration of machine learning-based auto-segmentation tools into radiation therapy workflows has the potential to improve treatment planning precision and efficiency. By automating the time-consuming task of contouring organs and target volumes, machine learning-based auto-segmentation tools allow clinicians to allocate more time to critical decision-making and personalized treatment strategies, ultimately enhancing patient outcomes.

## 2.7 Monte Carlo Simulations

Given an initial photon source and a patient, the medical physicist aims to determine the fate of these photons, which ultimately shapes the efficacy of a medical image or a patient treatment: how many photons interact within the patient and how many pass through unaffected. Initially, this calculation seems straightforward and can be accomplished using attenuation coefficients. However, the situation becomes increasingly complex when one photon generates another photon, and that photon, in turn, produces additional photons or electrons, and so on. This complexity is further amplified when considering dose scoring, as dose primarily accumulates along the random paths followed by electrons as they traverse through tissue. To tackle this challenge, two common methods are employed: the first involves setting up Boltzmann transport equations and solving them to obtain a steady-state solution for the differential equations, while the second approach, denoted MC simulation, involves simulating each particle individually as it traverses through the patient, tallying their locations and activities until a comprehensive representation of the desired metric is obtained. This metric could encompass various parameters such as dose distribution within the patient, incident photons on a detector surface, or other relevant factors. As Boltzmann solvers only exist in proprietary software and do not have the track record of accuracy many stable open-source MC softwares do, this work focuses on MC simulations only [69, 70].

EGSnrc [70], Geant4 [71], and TOPAS [69] are simulation software tools extensively used in the field of medical physics and radiation therapy research. EGSnrc is specifically designed for precise modeling of electron, photon, and positron interactions with matter, delivering highly accurate and quick simulation results. Geant4, on the other hand, is a versatile toolkit capable of simulating interactions of diverse particles with diverse materials. It offers advanced customization capabilities to tailor simulations for specific experimental setups. TOPAS, which is a wrapper for Geant4, is a user-friendly software tool focused on simulating radiation therapy treatments. It empowers the creation of patient-specific treatment plans and facilitates dose evaluation in simple scripts.

### 2.7.1 Random Number Generators

Integral to the MC process is the encapsulation of the probabilistic randomness of physics in the deterministic programming of a computer. Monte Carlo software uses (pseudo)random number generators (RNGs) to model this probabilistic nature that arises since two identical particles with identical initial conditions will often behave differently on their paths through the patients. This also gives rise to the name “Monte Carlo” in reference to the kinematic randomness of rolling dice in one of Monaco’s casinos. It remains an additional problem to produce these numbers which we denote pseudorandom rather than random as they are deterministic in nature and not truly random. Ideal pseudorandom systems do not repeat produce numbers between 0 and 1 with equal probability and do not have an obvious relation between random numbers. Incidentally, humans are terrible RNGs and this is a common fraud detection technique as humans love to pick the number 7 preferentially [72].

In medical MC simulations, it is common to track an enormous number of initial particles, often on the order of $10^{11}$, with numerous RNs being generated for each particle. To meet the demand for a vast number of RNs, a very long period (VLP) RNG is required. One option is to use the RDRANG method [73], which utilizes a hardware chip with a real entropy source, ensuring genuine randomness. However, this approach is not the most efficient and is only supported on newer chipsets. As a result, most MC software employs alternative approaches to fulfill the requirements of high-quality random number generation.

### 2.7.2 Fibonacci RNGs

Fibonacci series are some of the easiest to spot in a book of brain teasers as any number in the series is the sum of the previous two. Since the relation is obvious it stands as a poor candidate for a RNG. However, when a lag is added such that the two numbers used to produce the next occurred somewhere earlier in the sequence and not necessarily the two previous entries we get an RNG with some nice properties. The series looks something like this:

$$x_i = (x_{i-n} + x_{i-k}) \mod m \tag{2.16}$$

In this equation, $x_i$ represents the current RN being generated. $x_{i-n}$ and $x_{i-k}$ represent the previously generated numbers in the sequence, where $n$ and $k$ are the lag parameters such that $n > k$. $m$ represents the modulus, which is used to ensure the generated numbers are within a specific range. A great property of these RNGs are periods for known sets of $(2^n - 1)(2^{k-1})$. RANMAR is used in EGS which is a fibonacci type RNG.

Geant4 employs a modern RNG as its default option, with the Mersenne Twister being the chosen algorithm. While RANMAR is also available as an alternative, the intricacies of the Mersenne Twister algorithm are more complex than those of the Fibonacci RNGs and delving into the details of this RNG is not essential for comprehending the contents of this thesis [73].

### 2.7.3 MC Simulation Process

So you have developed a prospective treatment of a lung cancer patient using photons delivered from many angles to optimally treat a small lung lesion while avoiding accumulation of paralyzing dose in the spine. Thoracic anatomy, with it's alternation of bony ribs, soft tissue lesion, and low density lung presents electron build up regions and complicated dose distribution not readily modeled by analytical dose calculation, thus you would like to use a MC calculation to ensure that the treatment complies with initial objectives. You launch you MC simulation and the process looks something like this:

### 2.7.4 Simulation Setup

To properly specify a simulation we need to define a patient virtually or in some cases it is more prudent to use a test object which we call a phantom. While a real patient is a complicated thing with thoughts, feelings, hopes and dreams; for the purpose of our simulation a patient needs to only be specified as a map of their elemental composition at a resolution of about 1mm$^3$. This information has never been obtained at this resolution for any patient, in fact, the most up to date data on human elemental composition for many tissues is from the 80's for an ICRP project called the “Reference Man”. This is not, in fact, a superhero to help with reference formatting but a precedent to treat every patient (whether a person of another ethnicity or gender) with elemental composition from biopsy studies performed on young, mostly Caucasian, men from 40 years ago. Problematically, although some effort to update this database has occurred, most of these values are standard and in common use.

In radiotherapy treatment planning, accurate characterization of tissue heterogeneities is essential for precise treatment delivery. However, obtaining elemental composition information at a sub-mm level for patients is impractical through biopsies. Instead, a common approach involves using planning CT scans, which provide the required resolution but offer estimates of linear attenuation coefficients at around 100 kVp. To convert these CT values to elemental composition, a two-step process is employed. Firstly, the CT values are converted to an attenuation relative to water, leveraging the relative constantancy of this metric, the Hounsfield Unit (HU), across imaging systems. Subsequently, lookup tables, such as the one developed by Schneider *et al.* [74], are utilized to convert HU values to material composition. Schneider's method establishes the relationship between CT Hounsfield units and electron densities, serving as a fundamental input for radiotherapy planning systems considering tissue heterogeneities. Validating the precision and reliability of these calibration techniques is crucial, achieved through measurements using tissue equivalent materials and comparing the stoichiometric calibration's precision with the commonly used tissue substitute calibration. This research contributes to enhancing the accuracy and efficacy of radiotherapy planning systems, ultimately improving treatment outcomes for patients.

### 2.7.5 Virtual Models

As comparing different imaging methods on a patient is unethical due to the radiation dose, in some cases we may use virtual phantoms instead of actual patient data in simulations. Virtual phantoms are essential tools in radiotherapy treatment planning, providing a sophisticated representation of patient anatomy for accurate dose calculation and treatment optimization. These phantoms, such as the XCAT phantom developed by Segars et al. [75], seen in Figure 2.8, leverage computational models and imaging data to create realistic virtual representations of human anatomy. They incorporate intricate details of tissue heterogeneities, organ structures, and physiological functions to simulate patient-specific scenarios.

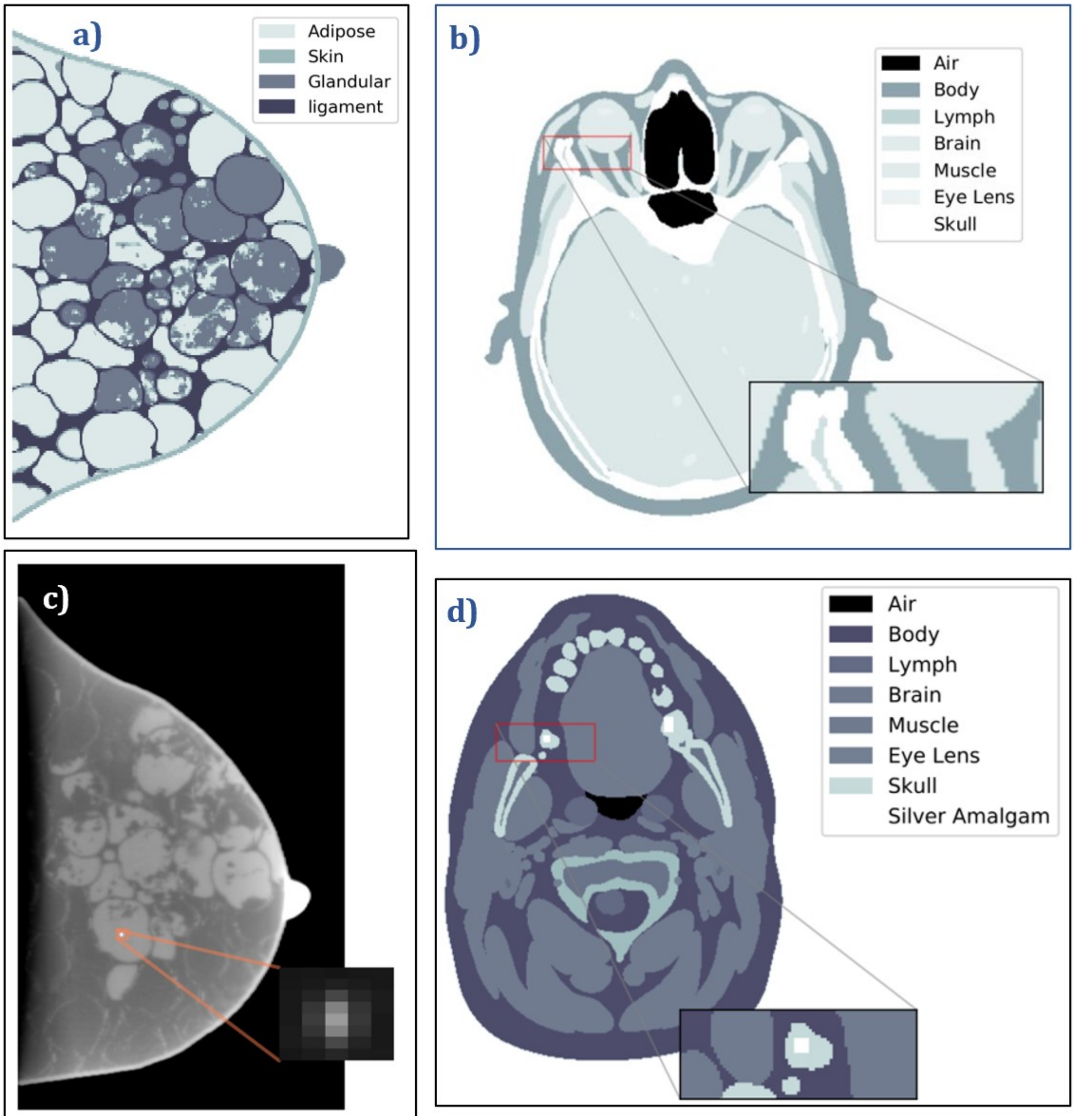

Figure 2.8: a) Anthropomorphic breast phantom by Jeon *et al.* [76] b) XCAT phantom section in the head. c) Image from Fastcat showing a reconstructed of the breast phantom with the inset showing a microcalcification. d) XCAT phantom showing the mandible region with a silver almalgam dental filling.

### 2.7.6 Beam Sources

Additionally a beam source is specified in the simulation. While the primary focus is often on photon and electron beam sources, MC simulations can equally accommodate proton or heavy ion sources. All sources require specification of direction and beam shape, such as creating a conical beam along the x-direction. Particle energy is another crucial parameter, ranging from simple mono-energetic cases like 100 keV electrons to more complex scenarios involving polyenergetic spectra in imaging simulations.

For polyenergetic beams, two approaches can be taken. The most accurate method, particularly in photon treatment contexts, involves separately simulating the treatment head of the linac head or the x-ray tube using MC simulations. The output of this simulation, stored as a "phase-space file," contains comprehensive information about particles passing through a specific plane, typically located at a known distance from the exit window of the linac or x-ray tube. Subsequently, in the patient simulation, photons are "restarted" to avoid redundant simulation of photon production [70].

Alternatively, an analytical method can be used to generate an energy spectrum for beam specification. This approach is simpler and faster but lacks the detailed energy and spatial distributions of the photons encoded in the phase-space file, as well as realistic considerations such as electron contamination and scattered photons in the beam. Nonetheless, in many simulations, this method proves to be sufficiently accurate.

### 2.7.7 Scorers

To determine the desired output values, a scorer is specified in the MC software. In treatment planning, 3D dose is typically scored in the CT volume, while in imaging, 2D photon counts or energy deposition is scored in the detector crystal. On the other hand, phase-space scorers, as previously described, can record the state of each incident particle on a specified plane, providing rich data for analysis but demanding significant memory resources and often generating gigabytes of data.

### 2.7.8 Sampling Probability Distributions

Once the simulation is defined, particle tracking begins. The initial position and momentum of particles are specified using RNs drawn from known probability distributions. We use different methods to map the uniform probability distribution of the RNs to specific probability distributions such as the angle of Compton scattering. One method involves inverting the probability distribution, enabling the mapping of a uniform distribution to any desired variable. This approach is employed for simple distributions like generating a random initial distribution from a square source of arbitrary length, where two random numbers are divided by a scaling factor to create a scaled uniform distribution. The same principle applies to Gaussian distributions, where the inverse of the distribution function is used.

When an interaction has been confirmed distributions of interaction product probabilities and their energies tabulated in the MV code for materials and energies are used to specify interaction products. Further RNs are used to specify the new particles trajectories. Probability distributions can be sampled in a few ways: Inverting the probability distribution is the most efficient way to produce samples according to a distribution but for functions that cannot be inverted different methods can be used.

The simplest way when an inversion cannot be found is to use the acceptance rejection method where a bounding box is made around the function, a random point $P_x, P_y$ is specified in this space and accepted only if $f(P_x) > P_y$ and another random point is drawn if $f(P_x) < P_y$ in this way allowing one to geometrically assign probabilities. This method is simple but inefficient, especially if area under the function is much smaller than the bounding box, likewise dimensions of the bounding box can be hard to find without calculating all values for the function. Another method called the Alias method in which the function is discretized, and the discrete function is inverted is generally used in it's place.

Table 2.2: Comparison of Sampling Techniques in Monte Carlo Simulations

| **Sampling Technique** | **Advantages** | **Disadvantages** |
|---|---|---|
| Inversion Method | - Efficient for distributions that can be inverted analytically - Provides direct samples from the desired distribution - Suitable for simple distributions like uniform or Gaussian | - Not applicable for complex distributions - Difficult to find inverse functions for many distributions |
| Acceptance-Rejection Method | - Can handle a wide range of distributions - No need to find inverse functions - Simple conceptually | - Inefficient if the bounding box is much larger than the distribution - Bounding box dimensions can be challenging to determine |
| Alias Method | - Efficient for discretized distributions - No need to find inverse functions - Relatively simple to implement | - Requires discretization of the distribution - Can introduce approximation errors |

### 2.7.9 Condensed History

Unlike photons, electrons interact readily in mediums and the exact simulation of an electrons random walk on a nanometer scale through a medium is generally unimportant in simulations with resolutions in the $mm^3$ range. However, it does become important if the electron crosses a grid boundary depositing dose in a new area. Thus, we use a condensed history (CH) approach to group many track segments of the electron random walk into a single step. The condensed history step length in the EGSnrc Monte Carlo code is determined using the following equation:

$$\Delta S_n = -\frac{1}{\mu(E,x)}\ln(\xi) \tag{2.17}$$

Where $\Delta S_n$ is the step length for the condensed history step, $\mu(E,x)$ is the energy-dependent linear attenuation coefficient of the medium, which depends on the energy $E$ of the electron and the path length $x$ traveled by the electron, $\xi$ is a random number generated from a uniform distribution between 0 and 1. This equation calculates the step length based on the inverse of the linear attenuation coefficient and the natural logarithm of a random number. It ensures that the step length is sampled probabilistically according to the exponential distribution, taking into account the attenuation properties of the medium. Similarly, the displacement and direction of the electron are sampled from other distributions. Importantly, In MC sims we are offered parameters to control the transport specifically, electron and photon cutoff energies at which we stop transporting the particles and score their energy in the current voxel [70].

So after a particle reaches a cutoff energy or exits the simulation volume, another particle is started, this process continues, laboriously and repeatedly, throughout the MC process, transporting each photon and in turn secondary particles for that photon and tracking their progress in scorers until all the particles specified by the simulation have been exhausted.

## 2.8 Treatment Planning

### 2.8.1 Treatment Planning Systems

Treatment planning systems (TPS) play a crucial role in medical physics, assisting in the precise and efficient design of radiation therapy treatments for cancer patients. One widely used TPS is Eclipse, developed by Varian Medical Systems. Eclipse utilizes a deterministic dose calculation algorithm called the Analytical Anisotropic Algorithm (AAA) for treatment planning [77, 78].

The AAA algorithm in Eclipse employs mathematical models based on empirical measurements to estimate the dose distribution within the patient's anatomy. It takes into account factors such as tissue heterogeneity and beam modulation to calculate the radiation dose delivered to the tumor while sparing surrounding healthy tissues. Eclipse provides a user-friendly interface for contouring structures, defining treatment beams, optimizing beam arrangements, and evaluating dose distributions.

In contrast, Monte Carlo treatment planning, as discussed previously, is an alternative approach that uses Monte Carlo simulations to model the transport of individual photons and electrons through the patient's anatomy. Monte Carlo simulations lead to highly accurate dose calculations. However, Monte Carlo treatment planning is computationally intensive and time-consuming compared to deterministic algorithms like AAA.

### 2.8.2 RTOG Guidelines for Lung SABR

The RTOG (Radiation Therapy Oncology Group) working group guidelines for lung stereotactic ablative radiotherapy (SABR) provide recommendations and dosimetric criteria for the treatment of lung cancer patients using high-dose radiation therapy [79]. These guidelines aim to standardize treatment planning and ensure the delivery of effective and safe radiation doses to the tumor while minimizing the dose to surrounding healthy lung tissue.

The dosimetric criteria outlined in the RTOG guidelines include various parameters that assess the radiation dose distribution within the target tumor and the dose limits for nearby critical structures. Some of the key dosimetric criteria and their purposes in the treatment of lung SABR patients are as follows:

- Planning Target Volume (PTV) Coverage: The recommended minimum dose ($D_{95\%}$) to the PTV, which encompasses the tumor, ensures adequate radiation dose coverage to the target volume, maximizing the probability of tumor control.

- Maximum Dose ($D_{max}$): The maximum allowable dose to the PTV or organ at risk (OAR) limits the risk of excessive radiation dose that could lead to complications or toxicity within the tumor or OAR.

- Normal Tissue Constraints: The guidelines provide specific dose limits for surrounding OARs, such as the lungs, spinal cord, esophagus, and heart. These constraints aim to minimize the risk of radiation-induced toxicity to these organs while still achieving effective tumor control.

By adhering to these dosimetric criteria, radiation oncologists and physicists can ensure that the treatment plans for lung SABR patients achieve the desired therapeutic effect while minimizing the risk of treatment-related side effects. These guidelines help standardize the planning process and facilitate effective and safe radiation therapy delivery for lung cancer patients undergoing SABR.

## 2.9 Forward on Research

The research presented in this dissertation has been built upon the foundation of fundamental physics principles, as well as the utilization of various tools, including software and instrumentation as described in this chapter. The subsequent chapters encompass work that has already undergone peer review and has been published in scientific journals. In these publications, detailed descriptions of the methods, motivations, and results/discussions have been provided. As a result, the chapters in this dissertation expand upon these methods, as necessary, within the context of the Methods and Materials sections. It is my intention that this section serves as a valuable contextual overview, providing insight into the general knowledge and practical considerations associated with the technologies explored and studied in the subsequent chapters.

# Chapter 3

# Development of Fastcat

**Fastcat: Fast Cone Beam CT (CBCT) Simulation** [1]

## 3.1 Introduction

Cone beam computed tomography (CBCT) is applied extensively in clinical radiotherapy. CBCT enables image-guided radiotherapy (IGRT) for the verification of patient positioning [81], quality assurance of treatment plans [82, 83], and real time tumor localization [81]. Two different methods of CBCT are clinically applied, both of which include a source and detector mounted on a rotating gantry. The most common CBCT system uses a gantry mounted kilovoltage (kV) x-ray source and a detector. This is known as on-board imaging or kV-CBCT imaging. Detectors in kV-CBCT can be thin and made of low Z materials since the beams are not very penetrating. Conversely, a megavoltage (MV) treatment beam can be used as the source in MV-CBCT imaging. MV detectors, also known as electronic portal imaging devices (EPIDs), are generally made of higher Z materials and are thicker to stop high energy x-rays. kV-CBCT has better soft tissue contrast and higher image quality than MV-CBCT [84]. However, kV-CBCT requires an additional source and detector. Conversely, MV-CBCT generally has reduced image quality and is used in specific applications such as high-Z material artifact suppression [85, 86] but does not require an additional source. Performance of these imaging modalities is dependent on the x-ray source spectrum and detector design. As such, EPID development and imaging beam optimization are active areas of research. To optimize new imaging techniques, Monte Carlo (MC) simulation methods are often used. These techniques enable an initial evaluation of imaging setups before creating an expensive prototype of the detector or source.

MC EPID simulations are accurate but exceptionally computationally demanding. A large number of particles need to be simulated to form a CBCT image. The long simulation time can be primarily attributed to two factors. First, MV detectors generally have low detective quantum efficiency (DQE), meaning that many particles that are transported in the simulation do not interact with the detector and do not contribute to image formation. A typical EPID DQE is as low as

---

[1] This work was published in the journal *Medical Physics* [80]

1%-1.5% [22, 37]. Second, the scintillator in which the optical photons are produced has a high scintillation yield; generating thousands of optical photons to be transported per interaction event. These two factors result in simulation times often as long as 3,000 core-hours for a $10^7$ primary x-ray simulation of one EPID projection [38]. Further, to produce a clinically equivalent image of 1 MU with a $10\times10\text{cm}^2$ field size a simulation with more than $10^{11}$ photons is required [39, 40, 41]. This problem is compounded in CBCT simulation, where it is necessary to simulate many projections of the object for CBCT image reconstruction.

Large headway has been made to reduce this computational overhead. Star-lack *et al.* have shown that one can simulate the detector response with only a fraction of the scintillation yield, significantly reducing the computation time [40]. Likewise, by simulating the optical spread function at discreet energies beforehand and convolving these optical spread functions with the energy deposition of an absorbed photon one can avoid simulating the scintillation processes completely [42, 43]. Additionally, Shi *et al.* introduced the fastEPID framework which pre-calculates energy deposition efficiency ($\eta$) and optical spread function (OSF) to remove particle transport in the detector entirely without loss of image quality [39]. Where $\eta$ is defined as the ratio of the total energy deposition in the scintillator and the total x-ray photon energy incident on the detector. However, these simulations are still considered computationally intensive with one image at 1 MU taking $1.540 \times 10^4$ core-hours on an Intel Skylake CPU core (Intel Corp., Santa Clara, Ca). Other MC approaches that are promising for image simulation are the GPU methods used by Badal and Badano as well as Bert *et al.* [44, 45]. The approaches have seen MC simulation speedup factors of 27 and 80-90, respectively. However, at this time, open source GPU MC codes lack the stability and versatility of more established codes such as Geant4 or EGSnrc.

Additionally, a number of works simulate fan and cone beam CT analytically to reduce computation time. ImaSim analytically simulates fan and cone beam CT through raytracing using vectorized phantoms [46]. VOXSI simulates kV fan beam CT using analytical raytracing with voxelized phantoms [47] and shows agreement with experimental images in terms of image contrast. DukeSim simulates kV fan beam CT with voxelized phantoms through a combination of analytical raytracing and GPU MC and demonstrates agreement between experimental and simulated images in terms of image contrast, noise magnitude, noise texture, and spatial resolution [48]. A drawback to the DukeSim approach is that the GPU MC reduces the simulation speed, requiring a 2-3 minute simulation per source rotation while running on 4 Nvidia Titan Xp GPUs with 64 GB of memory. Overall, none of these platforms are open-source and only DukeSim shows agreement with experimental noise and image contrast. Additionally, none of these platforms show experimental agreement for kV or MV CBCT.

In this work we use a modified fastEPID pre-calculation of MC data for the detector response while also pre-calculating the energy spectrum of the beam source as well as energy dependent scatter kernels for a cylindrical water phantom. We combine this data with an analytical GPU raytracer

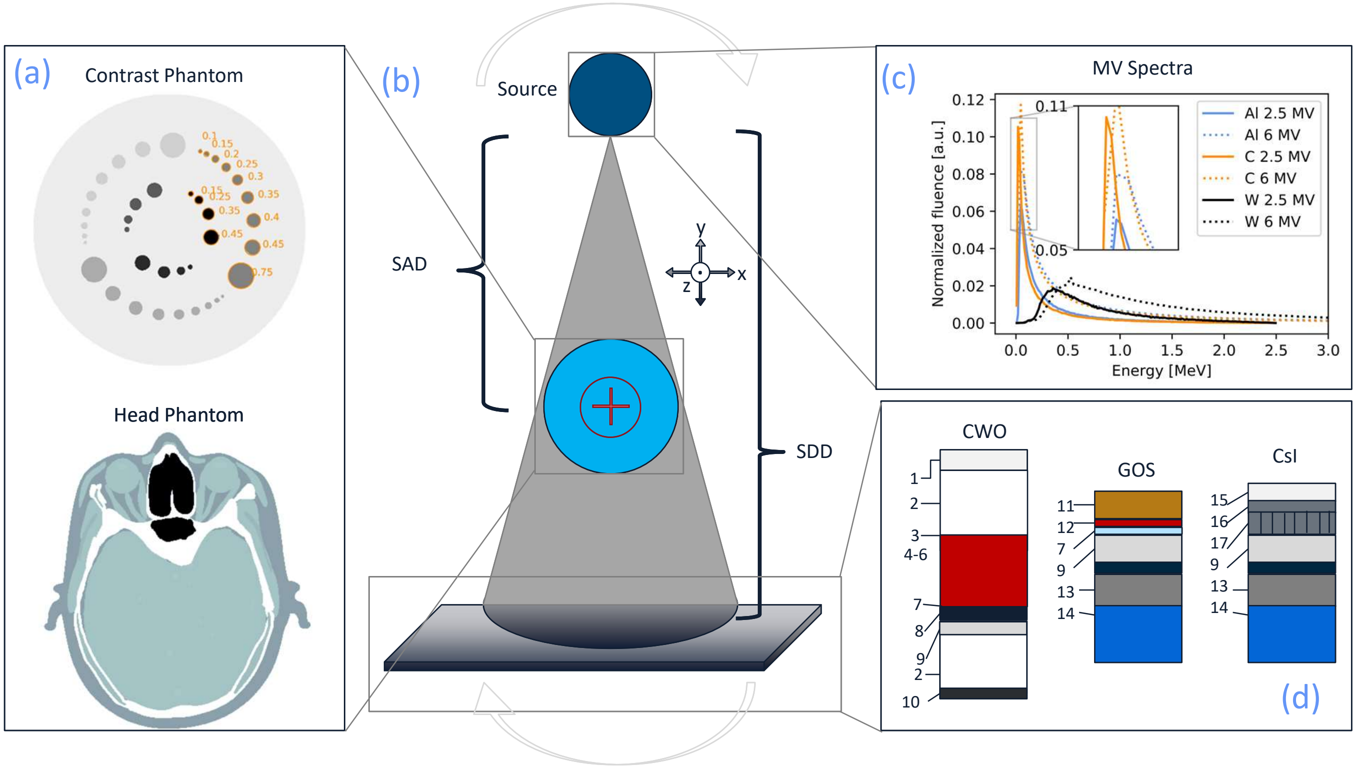

Figure 3.1: An overview of the simulation setup. a) The two phantoms used in this work, the Catphan 515 (top) and the XCAT anthropomorphic head phantom (bottom). b) The simulation geometry. c) The MV energy spectra. d) A slice of the CWO (left), GOS (center), and CsI (right) detectors with component labels corresponding to Table 5.3.

that provides the primary particle attenuation. This simulation strategy is used to create Fastcat, an open source simulation tool for CBCT image simulation to enable studies of novel beam, detector, and phantom combinations. Fastcat shows good agreement with MC simulations of full CBCT data acquisition and it results in extremely short run times on the order of 1 GPU-minutes for a full CBCT simulation.

## 3.2 Materials and Methods

The Fastcat simulation tool consists of a number of components that are described below. Fastcat is written in python (version 3.6). A Fastcat simulation can be specified and run as a python script. Likewise, the Fastcat graphical user interface (GUI) can be used to create and run Fastcat simulations. Fastcat incorporates code from xpecgen [87], an open source x-ray tube spectrum generator. The Fastcat default simulation geometry is depicted in Figure 3.1: A cone beam collimated to 16×16 cm$^2$

at isocenter impinges on a 16 cm diameter cylindrical phantom at a source-to-axis distance (SAD) of 1.00 m and a source-to-detector distance (SSD) of 1.52 m. The GUI workflow is depicted in Figure 3.2, which also shows the user selected parameters.

### 3.2.1 Imaging Beam

Fastcat can use MV or kV x-ray beams for CBCT image generation. MV spectra were calculated with EGSnrc/BEAMnrc [88] using a variety of target materials (carbon, aluminum, and tungsten) and electron beam energies (2.5 and 6 MeV) (Figure 6.1c). To generate the spectra a mono-energetic 0.02 mm diameter electron beam was incident on the target material. The thicknesses of the target materials were based on existing experimental beams for the carbon and aluminum targets [24] and are summarized in Table 3.1. For the low atomic number ($Z$) beams (carbon and aluminum), a 2 cm polystyrene filter placed at 50 cm from the target was used to reduce electron fluence in the beam. The photons were collimated by both primary and secondary collimators to create a $10\times10$ cm$^2$ field size at isocenter and phasespace files were scored at a distance of 100 cm from the target. Global electron and photon cutoffs were set to 0.01 and 0.001 MeV in the BEAMnrc simulations. $1.5\times10^8$ histories were used in each run resulting in $1\times10^6$ to $3\times10^7$ photons in the phasespace file. These simulations took on average 35 core-hours on an Intel Skylake CPU. Energy spectra with 200 evenly spaced energy bins between 0 and the maximum energy were generated from the phasespace files for input into Fastcat (Figure 3.1c). The kV spectrum was modelled for a 120 kVp beam with a 12° tungsten anode, a 0.4 mm beryllium window, and 1 mm aluminum filter in xpecgen [87].

Table 3.1: Electron target thicknesses used for the generation of the MV imaging beams.

| | tungsten | aluminum | carbon |
|---|---|---|---|
| 2.5 MV | 2.3 mm | 6.7 mm [89] | 7.6 mm [18] |
| 6 MV | 5 mm | 8 mm [25] | 9.9 mm [18] |

### 3.2.2 Detector Simulation

Fastcat currently employs two MV detectors: a novel Cadmium Tungstate (CWO) detector [17] and a Gadolinium Oxysulfide (GOS) AS1200 detector [90] (both Varian Medical Systems, Palo Alto, CA). A detector schematic is depicted in Figure 3.1d and detector material parameters are summarized in Table 5.3. The CWO detector has pixel septa between crystals and has a pixel pitch of 0.784 mm. The GOS detector has no septa and pixel pitches are set by the active matrix flat-panel imager (AMFPI) pixel pitch. AMFPI pixel pitches of 0.784, 0.392 or 0.336 mm were modelled for the GOS detector and 0.784 and 0.392 mm were modelled for the CWO detector. The response of the three detectors, including the optical transport, was simulated in Geant4 [71] using the Topas [69] wrapper. The

Table 3.2: Detector optical parameters [17, 90, 92]

| | Density (g/$cm^3$) | Material | Thickness (mm) | Abs. length (cm) \| Refr. ind. | Reflectivity |
|---|---|---|---|---|---|
| (1) carbon Fiber | 1.62 | C | 2.5 | – | – |
| (2) Foam | 0.05 | C | 33.1, 25.0 | – | – |
| (3) Vikuiti ESR | 1.05 | CH | 0.065 | 0.01 | 0.98 |
| (4) Scintillator Pixel | 7.9 | $CdWO_4$ | 15 | 125 \| 2.25 | – |
| (5) Pixel Glue | 1.0 | Epoxy | 15 | 100 \| 1.47 | – |
| (6) Pixel Septa | 2.7 | Al Mylar | 15 | 0.001 | 0.88 |
| (7) Meltmount Glue | 1.0 | $C_{21}H_{25}ClO_5$ | 0.01 | 300 \| 1.7 | – |
| (8) Mylar | 1.38 | $C_{10}H_8O_4$ | 0.065 | 100 \| 1.65 | – |
| (9) AMFPI | 2.6 | $SiO_2$ | 1 | 0.001 \| 1.70 | – |
| (10) Fiberglass | 1.85 | $SiO_2$ | 0.6, 6.0 | – | – |
| (11) Copper buildup | 8.9 | Cu | 1 | – | – |
| (12) GOS phospor | 4.59 | $Gd_2O_2S$:Tb | 0.29 | 43 \| 2.3, 1.0 (binder) | – |
| (13) Al alloy | 2.8 | Al | 1 | – | – |
| (14) Pb alloy | 10.95 | Pb | 3 | – | – |
| (15) Graphite | 2.26 | C | 1 | 0.001 | 0.88 |
| (16) CsI | 4.51 | CsI:Tl | 0.9 | 1.25 \| 1.8 | – |
| (17) Columnar CsI | 4.51 | CsI:Tl | 3.60 | 1.25 \| 1.8 | – |

responses of the detectors were modelled using a modification of the fastEPID framework developed by Shi *et al.* [39]. Mono-energetic pencil beams of energies of 10 to 90 keV in 10 keV increments, 100 to 900 keV in 100 keV increments, and 1, 2, 4, and 6 MeV were used to calculate the optical spread function (OSF) as well as the energy deposition efficiency ($\eta$) of each detector. For each of the energies, $1\times10^6$ histories were simulated resulting in a run time of roughly 48 core-hours per detector on an Intel Skylake CPU for the GOS detector. The other detectors had comparable run times but took longer to load the complex CWO pixels and columnar CsI geometries, which took 2 and 6 hours to load, respectively. All Topas simulations used the Geant4 Penelope physics list as well as the Geant4 optical physics list with a particle range cutoff of 5 $\mu m$ for all particles. No variance reduction techniques (VRTs) were used.

The kV CsI detector in this study was modelled as a 450-$\mu$m CsI scintillating detector [91] (Radiation Monitoring Devices, Inc., Water-town MA). The scintillating crystal is composed of a 100 $\mu$m graphite substrate, 90 $\mu$m of homogeneous CsI, and 360 $\mu$m of columnar CsI (Figure 6.1d). The columnar CsI was simulated with a column diameter of 10.2 $\mu$m and an 85% packing density with nitrogen gas between columns. Optical properties are summarized in Table 5.3. All MC simulation settings were the same as stated above for the CWO and GOS detectors. To reduce computation time in all detector simulations, scintillation yields of 600 photons per MeV were used.

As stated above, Topas MC simulations were used to determine the OSF and $\eta$ of each detector. The OSF is defined as

$$OSF(i,j) = \frac{Output(i,j)}{N_{incident} \times \eta}, \tag{3.1}$$

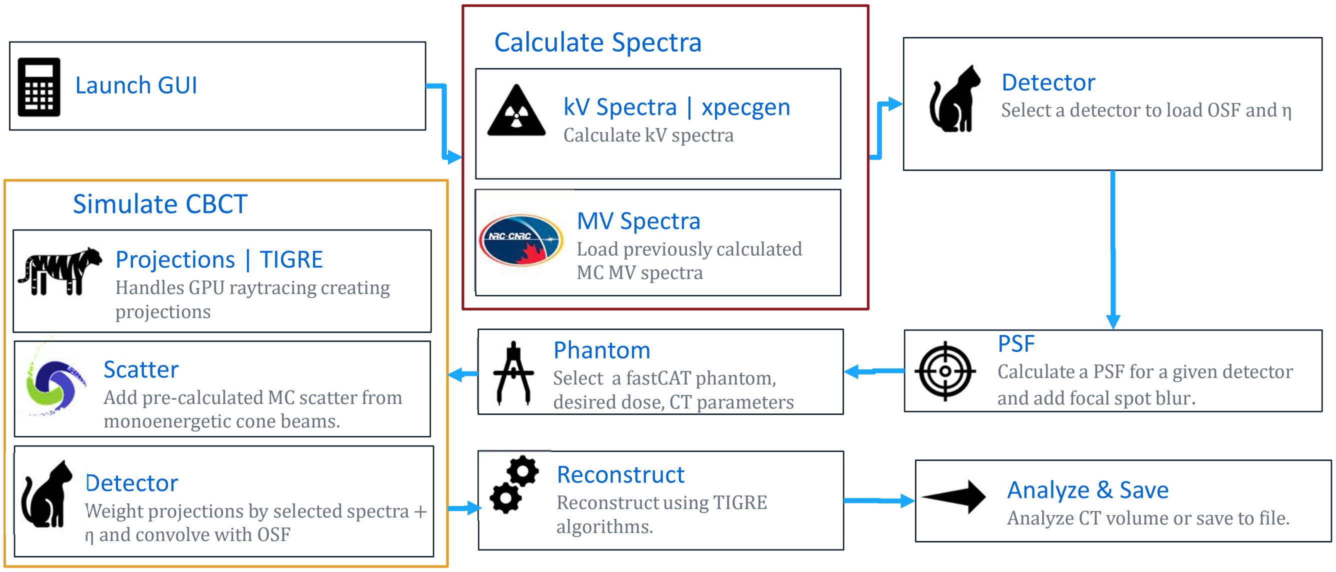

Figure 3.2: An overview of the Fastcat workflow.

where $Output(i,j)$ is the number of optical photons incident on the readout pixel with row and column indices of $i$ and $j$ and $N_{incident}$ is the total number of photons incident on the detector.

In this work, the OSFs were used to generate a detector modulation transfer function (MTF) from the point spread function (PSF). The 2D energy dependent OSFs were weighted by energy deposition efficiency multiplied with the incident spectrum from the selected beam to estimate the hypothetical PSF. This weighting is a modification of fastEPID. In fastEPID each photon is individually accepted or rejected from the detector with probability $\eta$. In Fastcat the fluence at a given energy is weighted directly by $\eta$. This approximation is done as the photons are not transported individually in Fastcat. This PSF was then convolved with an idealized 0.3 mm wide slit tilted at 2.5° to generate a line spread function (LSF), that was then presampled to estimate the MTF. The OSF was also used in the Fastcat CBCT simulation to generate the detector response, as discussed in section II.C.

The overall dimensions of the kV and MV detectors simulated in Fastcat were 40.1 cm by 10 cm, corresponding to 512 by 128 pixels. This resulted in a maximum field size of $27 \times 27$ cm$^2$ equivalent to those of real machines.

### 3.2.3 Imaging Phantoms

Two Fastcat phantoms are demonstrated in this work (Figure 3.1a): a Catphan 515 module with modified material compositions (The Phantom Laboratory, Salem NY) and the head of the anthropomorphic XCAT phantom [75]. All phantoms in Fastcat are saved as numpy integer arrays containing integers between 0 and $n-1$, where $n$ is the number of materials in the phantom. A corresponding phantom map with a string array of $n$ material names from the Fastcat material database is input into the Fastcat simulation tool. The Fastcat material database contains 336 materials from the NIST XCOM database [93], Geant4 default materials [71], and select materials from ICRU-44 [94]. Additional materials can be uploaded as a csv file containing energy and linear attenuation coefficient values.

The Catphan 515 phantom contained 5 to 15-mm in diameter inserts filled with five contrast materials. The default contrast materials in the Catphan 515 phantom were deflated lung, compact and cortical bone, adipose, brain and B-100, with material composition as defined in Geant4 default materials.

Additionally, the use of an XCAT phantom for CBCT imaging is demonstrated. Selected slices of the XCAT head phantom were first converted into a 1024×1024×10 binary array of attenuation coefficients with a voxel size of 0.5×0.5×3.125 $\text{mm}^3$, which was further converted into the Fastcat phantom format: The parameter files of the XCAT phantom were used to identify materials in the phantom by their attenuation coefficient. These identified materials were assigned equivalent Fastcat materials with energy dependent linear attenuation coefficients calculated using compositions from ICRU-44. The XCAT phantom is under the authors' individual license and not available in the Fastcat GitHub repository.

### 3.2.4 Full CBCT Topas Simulations

Topas was used to validate Fastcat by means of a full CBCT imaging simulation as well as by means of projection images. A full CBCT image of the contrast phantom for a 6 MV tungsten beam was simulated. A cone beam collimated to 16×16 $\text{cm}^2$ at isocenter impinged on the 16 cm diameter Catphan 515 phantom with SDD of 1.52 m and SAD of 1.00 m. Projection images of the Catphan 515 phantom were simulated at 180 evenly spaced angles distributed over a full 360° rotation. Particle counts were scored on an air slab at 1.52 m away from the source, and compared to Fastcat values. Simulation parameters described in the previous section were maintained. Particle transport through the full detector was not simulated as it resulted in a prohibitively long simulation time. Note that the Fastcat detector simulation was validated separately through comparing detector MTF to experimental detectors (3.2.2). CBCT MC simulations of the Catphan 515 phantom were performed using $2 \times 10^8$ particles per projection image. Full CBCT simulations were run on a high-performance computing cluster using 180×20 Intel E5-2683 v4 Broadwell cores. One full CBCT simulation took on average 37 core days.

Additional simulations of a single projection using other beam energy/target material combinations as well as average phantom dose were performed on a desktop computer using 8 Intel Skylake cores. The projection simulation parameters were the same as the CBCT simulations save the beam energy spectra, average phantom dose was scored simultaneously in these simulations. These simulations took on average 6 core-hours.

### 3.2.5 Scatter Modelling

The scatter kernels for a 16-cm diameter water phantom were generated in Topas using 18 mono-energetic cone beams and the default simulation geometry. To generate the scatter kernels a phasespace file was collected at the surface of a 40×10×0.3 cm$^3$ air slab located at the 1.52 cm SDD. Photons that did not interact in the phantom were filtered out. The spatial distribution of the scattered particles $y$ was averaged in the $z$ direction and fitted to a two parameter curve-fit of the form:

$$y = (\frac{a}{\sqrt{x^2 + a^2}})^b, \tag{3.2}$$

where $a$ and $b$ are fitting parameters and $x$ is the off axis distance. This fit was used to ensure a symmetric fit, and it resulted in a root mean squared error lower than a symmetric polynomial fit. The resultant energy distribution of the scatter from each mono-energetic cone beam was neglected in the analysis as sufficiently close agreement was seen when approximating the scatter as mono-energetic. These mono-energetic cone beam scatter curves were then combined with analytical projections to form the CBCT projection data discussed below.

While not an ideal representation, the approach of approximating the scattered radiation's energy to match that of the original beam demonstrated a higher level of accuracy than initially anticipated. For instance, when considering a 100 keV incident beam directed at the detector, the average energy of the scattered radiation was found to be 82 keV. Although this approximation does not achieve perfection, its adoption enabled substantial memory savings during code execution, thus justifying its implementation.

### 3.2.6 Raytracing

The bulk of the computational work of Fastcat CBCT image generation is in the CBCT raytracing. In this work the TIGRE [95] GPU reconstruction package was used for generating the cone beam forward projections. These primary projections are denoted as "projections" and they are equivalent to the sum of attenuation coefficient along the path of the ray between the source and detector. This is to be distinguished from what we will call the "intensity profiles" which are the counts in a given detector pixel.

One forward projection is calculated for each CBCT projection for each of the 18 energies. These primary projections are converted to intensity profiles using a flood field intensity profile made with the same geometry and number of photons as the scatter kernels, ensuring the correct scaling of the scatter. The scatter kernels are then added to the primary intensity profiles. These complete intensity profiles, $I(E)$, are then weighted by the fluence $\phi(E)$ and energy deposition efficiency $\eta(E)$ to form the final intensity $I_f$ as

$$I_f = \sum_E \phi(E)\eta(E)I(E) \tag{3.3}$$

To reduce computation time only ten slices in the z direction are simulated in the default phantoms, 512×512×10 voxels with voxel sizes of 0.31×0.31×0.31 $\mathrm{mm}^3$ were used for the Catphan 515. Likewise, the XCAT phantom had dimensions of and 1024×1024×10 voxels with voxel sizes of 0.5×0.5×3.125 $\mathrm{mm}^3$.

### 3.2.7 Noise and CBCT Reconstruction

Noise is added through a Poisson scaling of the particle counts incident on the detector. This scaling can be related to either dose or particle fluence as discussed below. The intensity profiles are then convolved with the OSF at each energy and summed to create the final profile at each beam angle. These are converted back to projections using the corresponding flood field and reconstructed. Reconstructions are performed with TIGRE algorithms which have many options for reconstruction types including the default FDK reconstruction [96] and more advanced iterative reconstruction. CBCT images were converted into Hounsfield Units (HU) using water region of the phantom for normalization. Image analyses can then be done using specific analysis modules attached to each phantom. For the Catphan 515 module, contrasts and contrast to noise ratios can be calculated. CNR was calculated as

$$CNR = \frac{|HU_w - HU_{ROI}|}{\sqrt{\sigma_w^2 + \sigma_{ROI}^2}} \tag{3.4}$$

Where $HU_w$ and $HU_{ROI}$ are the HU values water and the region of interest (ROI) and the regions respective standard deviations are represented by the $\sigma$s.

### 3.2.8 Dose calculation

The scaling of the noise in the simulation can be determined by the user based on either the requested mean dose to the phantom or the total particle fluence. Noise defined by particle fluence scales the intensity profile as $H$:

$$H = \frac{N_\gamma}{A/A_p}, \tag{3.5}$$

where $N_\gamma$ is the total number of particles $A$ is the area of the beam and $A_p$ is the area of a detector pixel. Once $H$ is found. Assumption of uniform phantom scatter n. Noise is then added using Poisson scaling based on the number of counts in a pixel.

Another option is to provide the mean dose to the water phantom for one projection. Fastcat will then estimate the noise based on the dose provided. Fastcat's dose estimate is based on the collision kerma in the phantom. This value for collision kerma is then related to dose by an empirical correction factor. This factor accounts for charged particle disequilibrium in the phantom. The dose calculation is as follows: The initial collision kerma per particle ($K_0$) at each energy is calculated as

$$K_0(E) = \frac{1}{N_i M} \sum_i E \frac{\mu_{en}(E)}{\mu(E)} (1 - e^{-\mu_i(E) x_i}), \tag{3.6}$$

where $i$ is the ray index, $\mu$ and $\mu_{en}$ are the linear and energy-absorption coefficients of water, respectively, $N_i$ is the number of rays, and $M$ is the mass of the phantom. These values estimate the average dose per particle at each energy. These initial collision kermas are weighted by the selected fluence $\phi$ and summed to get a total collision kerma $K_p$ per particle

$$K_p = \sum_E \phi(E) K_0(E). \tag{3.7}$$

These collision kerma estimates per particle were seen to correlate linearly ($R^2 > 0.99$) with the mean dose per particle calculated in Topas for the 16 cm diameter water phantom. An empirical linear fit to the Topas doses was used to relate the collision kerma to the final dose estimate per particle.

The noise was then calculated based on the number of particles. This was achieved by dividing the requested dose by the dose per particle. With the number of particles known, equation (3.5) was used to calculate the noise. The dose calculations were validated by comparing the average dose to the Catphan 515 phantom estimated in Fastcat to the dose calculated using the same imaging setup in Topas.

## 3.3 Results

### 3.3.1 Detector MTF

Fastcat showed very good agreement with measured and simulated MTFs for both the GOS and CWO detectors (Figure 3.3). For the GOS detector the average root mean squared error (RMSE) between the Fastcat and Topas simulations was 0.5%. The maximum RMSE was 1.3% at an MTF of 0.61 mm$^{-1}$. The average RMSE and maximum RMSE between the GOS MTF calculated by Fastcat and measurement data provided by Shi *et. al* was 1.2% and 2.8% at an MTF of 0.67 mm$^{-1}$, respectively. For the CWO detector, the average RMSE between the Fastcat and simulated data of Star-Lack *et al.* was 3.3 % and the largest discrepancy of 7.9 % occured at a spatial frequency of

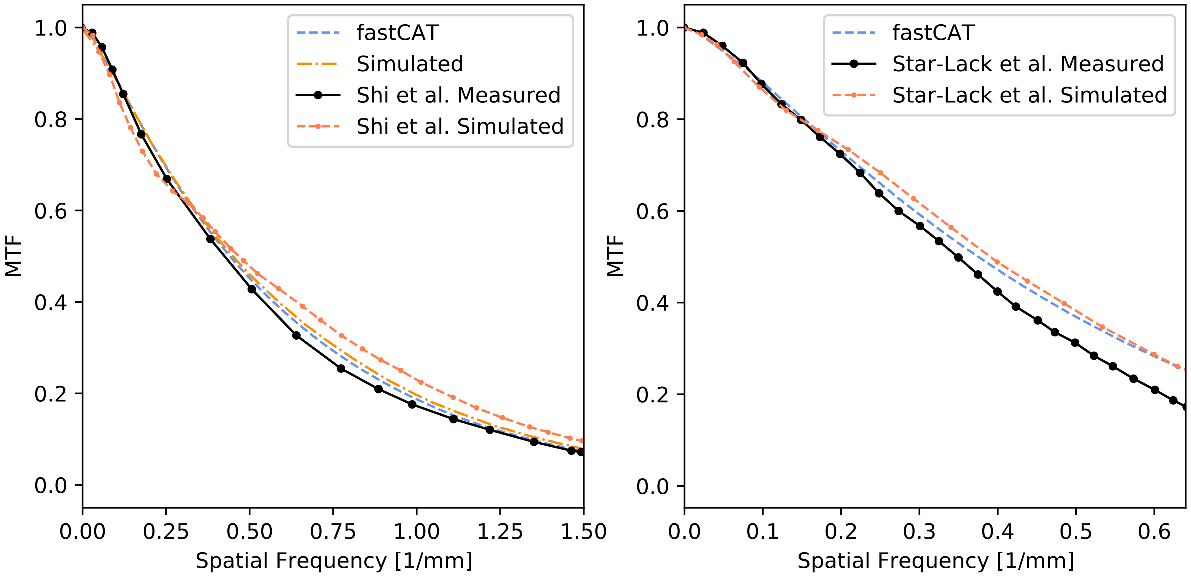

Figure 3.3: (L) A comparison of Fastcat-calculated MTF with measured and simulated values for the GOS detector with a 0.336 mm pixel pitch (based on Shi *et al.*) and (R) for the CWO detector with a 0.784 mm pixel pitch (based on Star-lack *et al.*).

0.64 $\mathrm{mm}^{-1}$. The average RMSE between the Fastcat and the measured data of Star-lack *et al.* was 3.5 % and the maximum RMSE of 7.9 % was observed at a spatial frequency of 0.64 $\mathrm{mm}^{-1}$.

### 3.3.2 Projections and dose

Comparisons of the Catphan 515 phantom projections and intensity profiles as calculated by Fastcat and Topas are shown in Figure 3.4. The intensity profiles for the 6 MV aluminum beam presented in Figure 3.4 on the left demonstrated a close agreement between Fastcat and Topas. The Fastcat and Topas intensity profiles had an average RMSE of 0.4% with a worst case RMSE of 1.1%. Likewise, for the 6 MV tungsten beam, Fastcat had an average RMSE of 0.2% of the Topas values with a worst case RMSE of 1.4%. The 120 kVp beam Fastcat intensity profile had an average RMSE of 0.5% of the Topas values with a worst case RMSE of 1.7%. The lowest accuracy was likely due to noise in Topas simulations. Fastcat noise showed good agreement with MC noise as seen in Figure 3.4 on the right. The RMSE of the standard deviation of all pixels between Fastcat and Topas was 0.21 % for the 6 MV tungsten beam.

Fastcat imaging dose calculations for the Catphan 515 phantom were compared to dose calculated for the same simulation in Topas. The mean dose to entire phantom was in a good agreement with the Topas dose estimates. Fastcat dose per photon had a mean difference of 1.4% of the Topas values for all beams. The largest dose estimation error between Fastcat and Topas was for the 2.5 MV

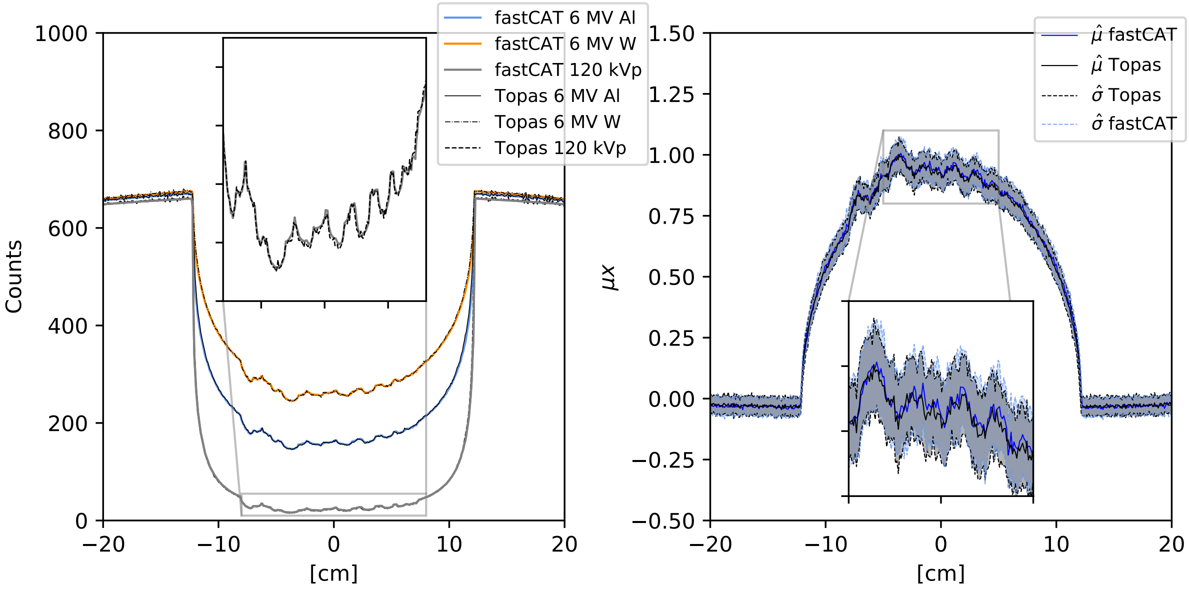

Figure 3.4: (L) Comparison of Fastcat and Topas intensity profiles for a 6 MV aluminum beam, a 6 MV tungsten beam, and a 120 kVp x-ray tube beam. (R) Comparison of Fastcat and Topas scatter profiles for a 6 MV tungsten projection (averaged over 64 pixels in the $z$ direction).

carbon beam with an error of 4.5 %.

### 3.3.3 CBCT images, CNR and calculation time

The agreement in intensity profiles translated into good agreement between HU values in a full CBCT reconstruction of the Catphan 515 phantom (Figure 3.5). The average RMSE between Fastcat and MC-calculated contrast was 0.5%. The mean error for each of the inserts was 0.6, -1.4, -1.3, 15.8, 4.2, and 10.2 HU for the deflated lung, compact and cortical bone, adipose, brain and B-100, respectively. All errors were within the 95% confidence interval.

The good contrast agreement also extended to good CNR agreement between Fastcat and Topas simulations (Figure 3.5). The average RMSE between Fastcat and MC in terms of CNR was 0.55. The RMSE for the each of the inserts was 0.30, 0.08, 0.39, 0.79, 0.15 and 1.59 for the deflated lung, compact and cortical bone, adipose, brain and B-100, respectively. All errors were within the 95% confidence interval.

To demonstrate Fastcat capability to simulate anthropomorphic phantoms, CBCT images of the head of the XCAT phantom are shown in (Figure 3.6). CBCT images presented in Figure 3.6 can be qualitatively compared to the 6 MV Catphan CBCT images presented by Star-Lack *et al.* [17] The increased noise in the GOS image due to the lower DQE of the detector is evident in both cases.

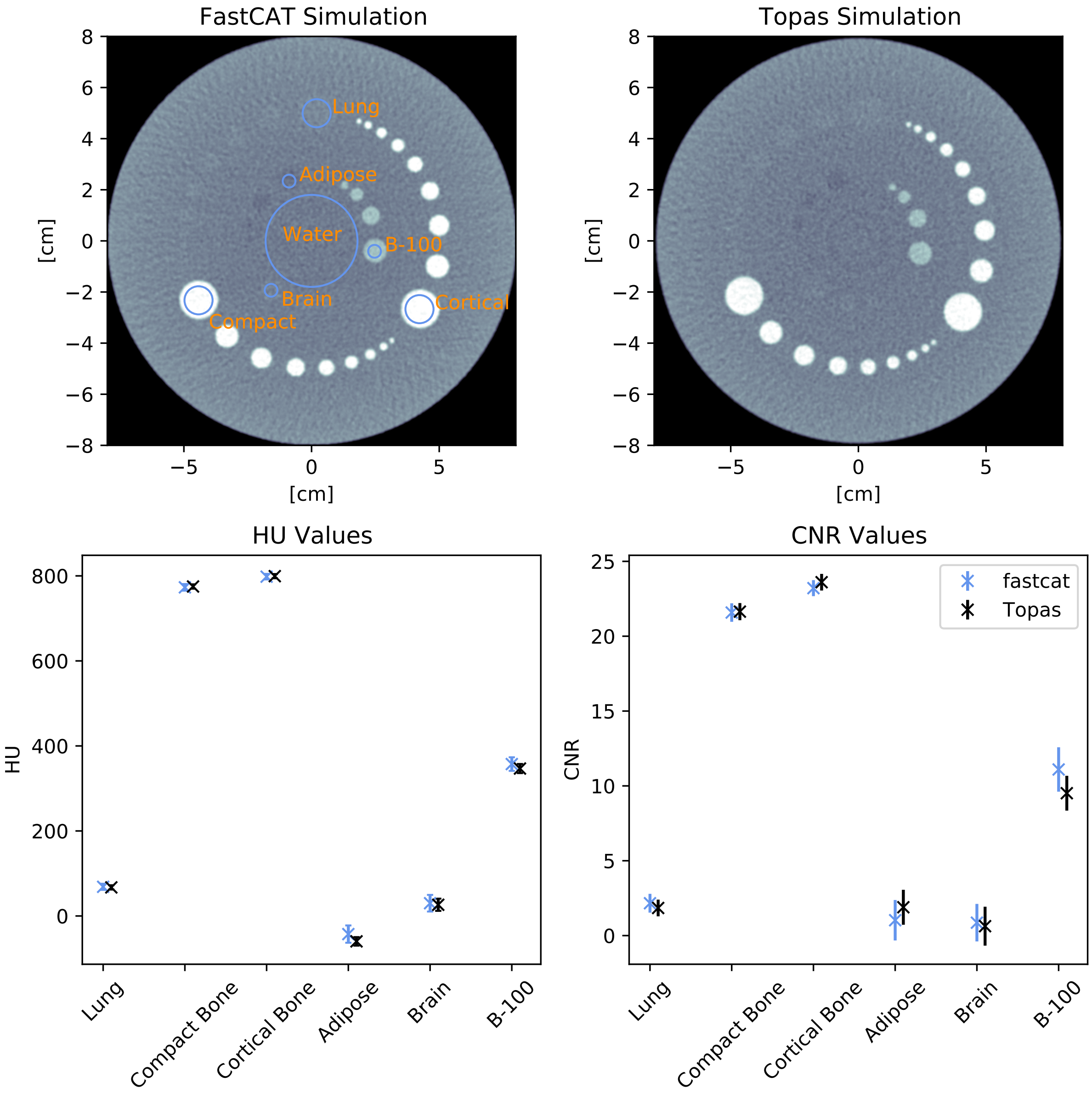

Figure 3.5: (Top) Fastcat simulation with ROI placement used for HU and CNR calculations (L) and full Topas simulation of the Catphan 515 phantom (R). (Bottom) A comparison of HU values (L) and CNR (R) in the CBCT Fastcat and Topas reconstruction.

A computational time comparison for CBCT simulations performed with a full Topas MC simulation, fastEPID and Fastcat for a 180-projection CBCT dataset generated with 6 MV tungsten beam was performed. An extrapolation is made for a full Topas MC simulation based on the time for single projection simulation with $10^9$ photons. The extrapolation predicts 5.6 core-years of compute time to create a full CBCT. A fastEPID simulation using the same parameters would take an

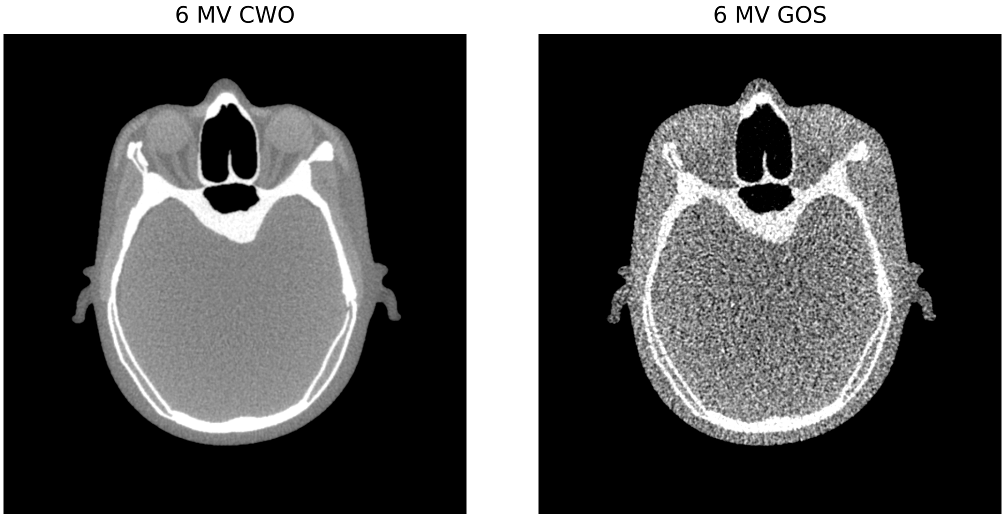

Figure 3.6: Fastcat CBCT images of an anthropomorphic head phantom created with (L) a 6 MV tungsten beam and the CWO detector and (R) a 6 MV tungsten beam and the GOS detector. CBCTs were normalized to a mean dose to the phantom of 7 mGy and used 487 projections.

estimated 0.32 core-years, while the Fastcat simulations takes 40 and 61 seconds for a 512×512×10 and 1024×1024×10 reconstructed image size respectively.

## 3.4 Discussion

While the end goal of this platform is to achieve agreement of Fastcat and experimental CBCTs data, this work focuses on agreement between Fastcat simulations and MC simulations as an initial validation. Overall, there was a close agreement between Fastcat and MC-generated MV CBCT images and the next step will consist of experimental validation. One validated Fastcat result is the MTF of the GOS and CWO detectors, which had a mean error of 1.2% and 3.5% of detector measurements performed by Shi *et al.* and Star-lack *et al.* respectively. This comparison lends some validity to the Fastcat simulation method. However, the full MC imaging simulations contains assumptions which may need to be modified to return result consistent with experimental data. These assumptions, such as a spatially uniform cone beams and not generating scatter in the primary and secondary collimators, will perhaps degrade the agreement between Fastcat results and experimental measurements. Further work will assess this fidelity and might lead to adjustments in Fastcat so as to attain the highest possible agreement with experimental data.

Fastcat's agreement with MC image quality metrics is a validation of two assumptions underlying Fastcat: 1) Simulating a phantom at 18 discrete energies, and combining with the weighting described, is sufficient to recreate MC image quality metrics accurately. 2) Scatter does not need to be angularly dependent in a Catphan simulation to generate agreement with the MC image metrics discussed.

Further, scatter generated from a uniform water phantom was an estimate of the scatter generated in a phantom of the same size containing contrast inserts. The nearly identical Fastcat and Topas intensity profiles shown in Figure 3.4 explicitly validate this assumption. The difference between Fastcat and Topas for the 6 MV aluminum, 6 MV tungsten, and 120 kVp beams, with respective RMSEs of 0.4, 0.2, and 0.5%, indicated that a generalized scatter is sufficient to produce intensity profiles within 0.5% of MC values. Due to the close agreement resulting from the uniform phantom we speculate that a similar agreement would be found for the similar sized XCAT head phantom and further research will investigate this agreement. We should note that for body-sized phantoms, a new scatter model would have to be built.

The scatter produced for the anthropomorphic head phantom originated from a cylindrical phantom with an identical diameter to that of the head phantom. Although this approximation is expected to introduce variations in the resulting images compared to those generated through Monte Carlo simulations, we posit that these artifacts will facilitate a qualitative assessment of the impact of different imaging methods on human anatomy. For a more comprehensive quantitative analysis, users can refer to the phantom images which possess accurate scatter statistics.

The scatter specified in fastcat is ideally suited for head cases and symmetric anatomical regions. Less cylindrically symmetric areas would demand a detailed scatter modeling approach, possibly involving oblong cylinders mirroring regional anatomy properties. Extremely inhomogeneous or irregular regions could benefit from alternative approaches like GPU-based MC or kernel methods for scatter generation.

### 3.4.1 Limitations

Fastcat suffers from some rigidity in terms of certain parameters. The detector pixel pitch is not a parameter that can be easily modified from the available built-in detectors as this requires rebinning of MC phasespace files in the case of the GOS detector. These files are too large (up to 2.5 GB in size) to include in the software. For a detector like the CWO, modifying the pixel pitch is even more complicated as the detector septa must be moved and the simulation rerun. The implemented scatter kernels further restricts the use of Fastcat, as scatter is made for the simulation of a 16-cm diameter water phantom and the agreement between Fastcat and MC simulation will degrade for phantoms that are significantly larger or smaller.

Additionally, in the time comparisons, Fastcat would suffer from memory constraints in completing simulations with high resolution reconstructions, while memory would not be a factor in MC simulations. For example, a simulation of the XCAT head phantom with a phantom size of 1024×1024×10 voxels, 360 projections, and a detector size of 124×512 pixels uses 2.6 GB of RAM. Extending this to a full detector of 1024×1024 pixels and a larger phantom one could easily exceed the RAM capacity of most personal computers. This is due to Fastcat memory requirement scaling linearly with the number of detector pixels. Further work will aim to resolve this rigidity.

We would also like to mention that in the time comparison Fastcat is being compared to a Topas MC simulation without the use of VRTs. Topas was used due to its ability to simulate optical photons. However, Topas as it is a wrapper of Geant4 is seen to be slower than other codes such as EGSnrc in some instances. Sometimes the difference can be by an order of magnitude for common MC simulations [97]. Likewise, VRTs such as cross section enhancement, interaction forcing, or importance sampling could be used to increase the efficiency of the MC calculation. Thus, it is possible that another MC simulation method could reduce simulation times by about two orders of magnitude as compared to the MC simulations shown in this work.

Likewise, Fastcat is dependent on the TIGRE python package which in turn has a CUDA dependency. This is a limitation of the simulation tool, as many users may not have a CUDA installation, a CUDA capable GPU, or have a GPU at all. Therefore, further work will aim to make a CPU version of Fastcat to increase accessibility.

In this work, the tissue elemental composition values from ICRU 44 [98, 94] were utilized as the primary dataset. It is important to note that while this dataset is the most comprehensive of its kind, it has certain limitations in terms of demographic representation. The majority of the samples within the dataset are derived from biopsy studies conducted on Caucasians with a bias towards men biopsied in the 60s and 70s. As a result, there is a potential inadequacy in adequately representing the diversity of demographics within the population. It is essential to acknowledge that the simulation data contained within this package may predict elemental compositions with a certain degree of inaccuracy for individuals from different demographics.

### 3.4.2 Future applications

Three applications of Fastcat are speculated by the authors: 1) development of new CBCT imaging techniques (the primary goal of this platform), 2) deconvolution of CT images using an approximation of the PSF, and 3) dataset generation for machine learning (ML) deployment. First, Fastcat can be used to quickly asses the effect of various combinations of beam energies and detector types on CBCT image quality. Fastcat greatly decreases the time it takes to simulate these combinations as it can be done in minutes while giving comparable results to MC in terms of image spatial resolution, contrast and CNR. This allows for a greater flexibility in exploring the parameter space for CBCT imaging equipment and protocols. Second, Fastcat generates a PSF for a given beam and detector with an arbitrary focal spot size. If agreement can be achieved between the image MTF of Fastcat and a system experimental data by modification of the focal spot size, one could use the Fastcat PSF to estimate the system PSF. The knowledge of PSF allows one to perform a deconvolution of the image to improve the spatial resolution of CBCT images. In a test case using Richardson-Lucy deconvolution [99, 100] on a Fastcat MTF phantom (Figure 3.7), CBCT image MTF increased by a factor of two using deconvolution of the projection images.

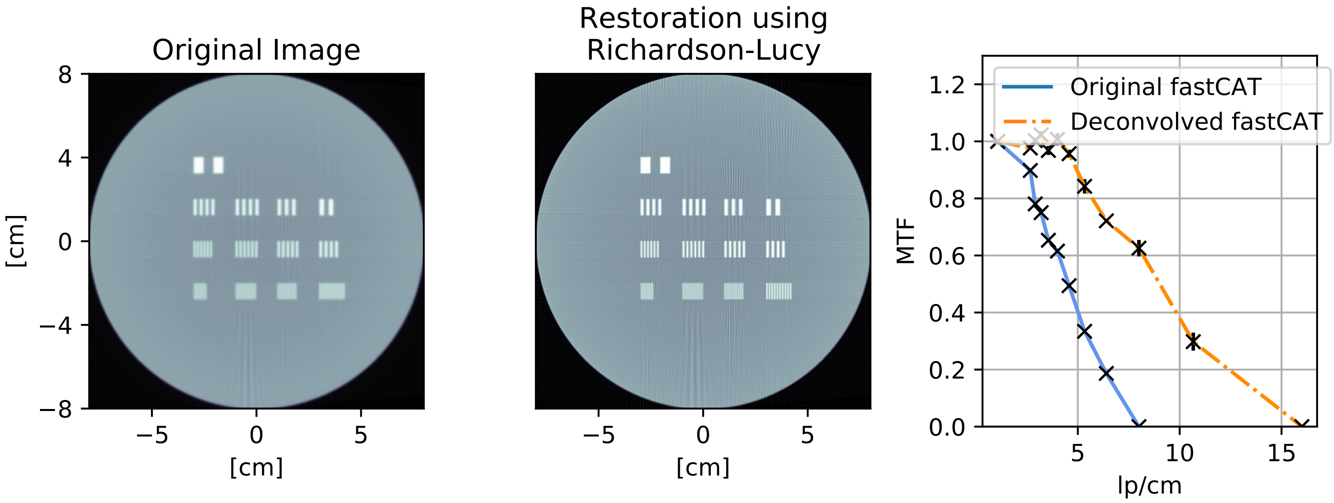

Figure 3.7: The MTF phantom (L) reconstructed conventionally and (Center) using the Richardson-Lucy deconvolution and the PSF calculated by Fastcat. (R) MTF comparison for the two images. The crosses mark the spatial frequencies in the phantom.

Third, Fastcat could be imagined as a tool to link simulation space to real clinical imaging. This could be done by maintaining a Fastcat model of a clinical imaging setup through adjusting user parameters available in Fastcat to agree with monthly quality assurance (QA) images of a Catphan phantom. A clinic could then use Fastcat to generate arbitrary ML training data personalized to a given machine in terms of contrast and MTF. This overcomes some obstacles that arise in terms of ML algorithms which have to be trained on general datasets and can not necessarily respond to changes in medical imaging equipment output over time. This allows for a more personalized approach between dataset generation that links to clinical QA. The Fastcat simulation method could provide superior performance of ML algorithms and remove risks that ML output would be invalid due to changing machine performance. Automated segmentation of bone CBCT for patient positioning could be suitable for Fastcat, where algorithms could be retrained on adjusted data if drift in QA MTF or contrast indicated a change in image quality.

Additionally, Figure 3.6 demonstrates the use of Fastcat with an anthropomorphic phantom to simulating more clinically relevant imaging situations. The use of an anthropomorphic phantom with Fastcat allows users to conduct virtual clinical trials [101]. In a virtual clinical trial, different imaging methods could be compared to ascertain the most successful imaging method for a given clinical situation. This could be used, for example, to asses different CBCT acquisition settings for use in radiotherapy treatment planning.

### 3.5 Conclusion

We presented Fastcat: a fast simulation tool for kilovoltage and megavoltage CBCT image generation. Fastcat shows good agreement with measurements with respect to MV beam spatial resolution for a GOS and a CWO detector. The simulation tool was also validated with respect to Monte Carlo simulations using contrast modules of a Catphan 515 phantom. A maximum difference of 16 HU between Fastcat and Monte Carlo simulations was observed for the brain, deflated lung, compact and cortical bone, and adipose tissues inserts. The complete Fastcat CBCT dataset generation for a 512×512×10 and a 1024×1024×10 reconstruction size took 40 and 61 seconds, respectively. This is approximately five orders of magnitude faster than the corresponding Monte Carlo simulations.

### 3.6 Acknowledgments

The authors would like to acknowledge Chelsea Dunning for the contribution to the name Fastcat. We would also like to thank Marios Myronakis for sharing the GOS MTF data with us. This research was enabled in part by support provided by WestGrid (www.westgrid.ca) and Compute Canada Calcul Canada (www.computecanada.ca). We would also like to thank Paul Segars for providing us with an XCAT license. The work was partly funded by an NSERC Discovery Grant and the Canada Research Chair program.

### 3.7 Conflict of Interest

The authors have no conflicts to disclose.

### 3.8 Data Availability

The Fastcat package is available at https://github.com/jerichooconnell/Fastcat.git.

# Chapter 4

# Experimental Validation of Fastcat

**Experimental validation of Fastcat kV and MV cone beam CT (CBCT) simulator** [1]

## 4.1 Introduction

Cone beam computed tomography (CBCT) [103, 104] is used extensively to visualize patient anatomy in the planning and administration of radiotherapy treatment. As such, CBCT that provides more accurate and realistic images can improve radiotherapy patient positioning and beam alignment. To this end CBCT is being constantly ameliorated, active research is being conducted end to end in the imaging process. To evaluate the efficacy of new research, two approaches are often used. New CBCT imaging methods can be evaluated based on an experimental phantom of known composition and dimensions with reproducible results but limited relation to real patient data. Conversely, evaluations can be performed using real patient data of unknown composition and dimensions with limited reproducibility. The ideal case, to evaluate new research on a realistic patient model with known composition, dimensions and robust reproducibility is an active area of study and the focus of this work.

With the introduction of new anthropomorphic virtual phantoms [105, 106], a new approach to evaluating x-ray imaging research has become viable. Realistic anthropomorphic phantoms allow simulations to be performed with realistic patient anatomy without the patient dose and uncertain ground truth associated with clinical data. Numerous simulators exist that are compatible with these phantoms.

These CT simulators generally use Monte Carlo (MC) platforms [45, 107, 108]. These MC platforms, while used primarily for dose calculation in radiation therapy, have superior accuracy due to precise simulation of the particle transport underlying CBCT. However, MC methods suffer from long compute times for simulating CBCT. This is due to a variety of factors, e.g. the number of projections needed, the handling of a high resolution voxelized phantom, and the transport of optical photons in the simulator, all of which can be detrimental to computation speed. For example, in

---

[1] This work was published in the journal *Medical Physics* [102]

a study by Blake *et al.* [38] simulation of one projection image with a scintillating detector and $10^7$ primary x-rays took 3000 CPU-hours. Conversely, recently developed GPU MC methods show speedup factors exceeding 1000 times traditional MC [109]. These methods, while promising, are not widely implemented due to the current lack of demonstrated accuracy and stability as compared to CPU methods. Likewise, MC methods suffer from increased load times, compute times, and memory constraints as the resolution of an anthropomorphic phantom is increased. For example, in the work of Yeom *et al.* [110], which examines the performance of Geant4, MCNP, and PHITS with respect to dose calculation speeds in voxelized anthropomorphic phantoms, simulation times were increased by an order of magnitude in Geant4 when decreasing voxel size from 1 $mm^3$ to 0.1 $mm^3$, while MCNP nor PHITS could simulate a 0.1 $mm^3$ phantom due to the number of phantom voxels exceeding the maximum limit of the simulation codes.

Other simulation approaches are currently available to improve simulation time. Graphical processing unit (GPU) MC is a current method that shows speed up factors of 27-90 over traditional CPU-based MC [44, 45]. Likewise, ray-tracing methods are available for CPU and GPU [47, 46]. These methods are very fast but cannot account for scatter in phantoms and detector response. A variety of hybrid methods also exist [111, 112, 113, 48]. Hybrid methods have been successful in some applications. For example, gDDR simulations [111] showed agreement with experimental noise amplitude in CBCT with a relative difference 3.8%. However, these methods have some limitations. The methods were either not validated against commercial CBCT scanners for realistic voxelized phantoms or take hours to generate a CBCT image without a high performance computing cluster.

To address these limitations, Fastcat, an efficient hybrid CBCT simulator of both kV and MV CBCT imaging, was developed [80]. Fastcat combines analytical primary radiation and MC scatter to create CBCT volumes. Fastcat is capable of simulating both kV and MV commercial CBCT scanners and it takes a few minutes to run a CBCT simulation using a realistic number of projections on a desktop computer with a single GPU. The method behind Fastcat, as well as validation against MC has been described in previous work[80]. However, a concern with our past work was the lack of experimental validation against CBCT scanners. Here we experimentally validate the Fastcat simulation platform. A comprehensive evaluation of image quality metrics is performed to demonstrate the accuracy of the method. This platform enables rapid evaluation of new CBCT protocols.

## 4.2 Materials and Methods

### 4.2.1 Experimental Data Acquisition

Fastcat was validated for two different experimental CBCT data sets acquired on a Truebeam STx linac (Varian Medical Systems, Palo Alto, CA).

### kV CBCT

An experimental kV CBCT image was acquired using the Varian Truebeam kV Planar Imager (which we also refer to as the OBI). The kV CBCT image was acquired using a Varian GS-1542 x-ray tube with a 100 kVp x-ray beam. The spectra was filtered by 2.7 mm aluminum inherent filtration as well as a 0.89 mm titanium beam hardening filter. An aluminum bowtie filter was also used with a minimum thickness of 1.53 mm and a maximum thickness of 27.42 mm. The detector was a PaxScan 4030CB (Varex Imaging Corporation) flat panel detector with an anti-scatter grid (ASG). The ASG was the default model with a grid ratio of 10, septal thickness of 0.036 mm, and line density of 60 lines/cm. The detector itself was a 0.6 mm columnar CsI detector with a fill factor of 70% and an amorphous silicon readout pitch of 194 $\mu$m. The scan was acquired in the fluoro-mode with pixels binned to 388 $\mu$m. Thus, the detector had a pixel matrix of 1024×768, with a total detector size of 397×298 mm. A total of 887 views of the phantom were acquired at equally spaced angles over a 360 degree rotation. The beam was collimated to 14 cm × 14 cm at isocenter. The scan $\mathrm{CTDI}_{vol}$ was 21.1 mGy. The CBCT was acquired in developer mode and the reconstruction was performed using the FDK algorithm [96] with a ram-lak filter. The reconstruction kV CBCT image size was 512×512 pixels with isotropic voxel dimensions of 0.391 $\mathrm{mm}^3$.

### MV CBCT

The MV CBCT was acquired using the 6 MV therapy beam with the default tungsten target and a flattening filter. The detector used was a Varian as1200 GOS detector with a pixel pitch of 0.392 mm. Optical properties of the detector are described in more detail in the work of Shi *et al.* [90]. The detector had a pixel matrix of 1024×768, with a total detector size of 401×301 mm. A total of 493 views of the phantom were taken at equally spaced angles over a 360 degree rotation. The beam was collimated to 14 cm × 14 cm at isocenter. The scan was acquired with a dose of 300 MU. A high dose was used to ensure adequate image quality from the low quantum efficiency GOS detector. It should be noted that 300 MU is much too high for a clinical MV CBCT dose and was only used for validation. The CBCT was acquired in developer mode and the reconstruction was performed using the FDK algorithm with a ram-lak filter. The reconstructed CBCT image size was 512 × 512 pixels with isotropic voxel dimensions of 0.391 $\mathrm{mm}^3$. An fft-wavelet ring artifact reduction was used to reduce artifacts in the presented image [114]. Ring artifact reduction was not used in the analysis since the dampening of high wavelet frequencies can reduce image noise.

### 4.2.2 Fastcat Overview

The goal of Fastcat is to simulate CBCT with the highest computational efficiency without compromising accuracy; a detailed description of Fastcat can be found in the previous work of O'Connell and Bazalova-Carter [80]. Fastcat's methodology is to separate a MC simulation into primary radiation and scatter. The primary radiation is attenuated analytically while the scatter is simulated in MC. The scatter is then curve fit to remove noise. Scatter is only calculated once per phantom at 18 discrete energies and stored in Fastcat. One scatter profile is calculated for each phantom and used independently of the angle of projection. The scatter calculation depends on certain aspects of the geometry. Namely, the scatter depends on the source and detector distances from the isocenter, cone angle, and phantom size. When these variables are changed, the scatter must be updated. To allow for arbitrary polyenergetic beams the primary and secondary radiation are both simulated at 18 discrete energies between 10 keV to 6 MeV. The energies are 10 keV to 100 keV in 10 keV, 300 to 900 keV in 200 keV increments and additional 1, 2, 4, and 6 MeV. To form the image the primary radiation and scatter are weighted, quantum noise is added through Poisson scaling based on a user defined mean phantom dose or number of photons, the counts at different energies are then combined. Currently, only quantum noise is modelled in Fastcat as it results in generally a much larger effect than electronic noise. The focal spot of the source is simulated by convolving the detector point spread function and a Gaussian kernel with a full width at half maximum (FWHM) the size of the focal spot multiplied by a magnification factor to account for the geometry of the simulation. These weights are determined by the input spectrum and the detector energy response. Here we will focus on the descriptions of additional Fastcat features that were included in this work.

Fastcat simulations were performed on a linux desktop computer with 16 GB memory a Nvidia GeForce RTX 2070 GPU and eight Intel Skylake CPUs.

#### Phantom

The phantom used in this study was the CTP404 sensitometry module from a Catphan 504 phantom (The Phantom Laboratories, Salem, NY). The 20-cm diameter sensitometry module contains 1.2-cm diameter inserts filled with air, acrylic, low-density polyethylene (LDPE), teflon, polystyrene, delrin and polymethylpentene (PMP). The phantom was positioned with the center of the CTP404 module at isocenter.

### 4.2.3 Fastcat CBCT Simulations

The kV Fastcat simulation used as input an analytical x-ray source generated in xpecgen [87] with an anode angle of 14° and a tube voltage of 100 kVp. Fastcat setups are seen in the graphic in Figure 4.1. The source was subject to additional analytical filtration of 2.7 mm of aluminum and a 0.89 mm titanium beam hardening filter. The detector modelled in the simulation was a columnar CsI detector with optical properties based on the work of Freed *et al.* [92]. The columnar CsI was 0.6 mm thick with a fill factor of 70% and a pixel pitch of 384 $\mu$m.

The MV Fastcat simulation source was a 6 MV Truebeam phase-space file provided by Varian. Although considered preferable by the authors, an analytical simulation of the MV beam was not used as a suitable model could not be found. This phasespace was binned by photon energy to

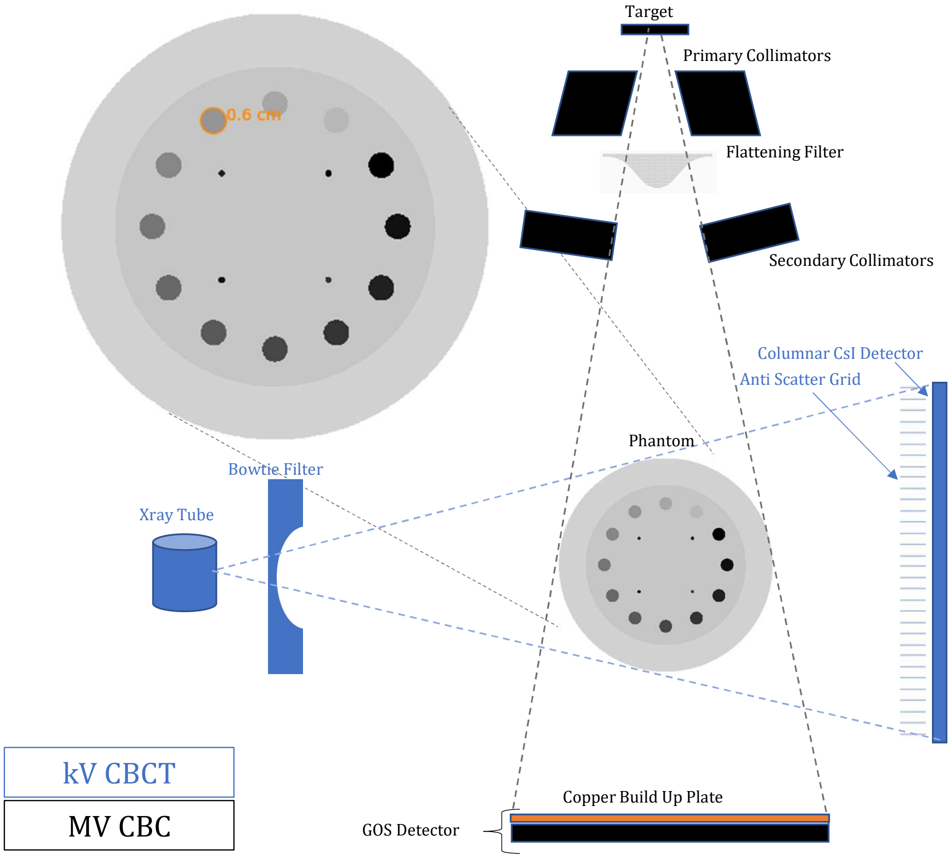

Figure 4.1: A schematic of the Truebeam linac and CTP404 module. The kV and MV imaging systems are shown in blue and black, respectively. Dotted lines outline where the beams would be generated. The phantom displayed is used to represent the phantom geometry. Thus, the phantom colormap does not correspond to any material property. The schematic is not to scale.

provide a photon spectra for input into Fastcat. The detector used in the simulation was modelled as a Varian as1200 detector using the optical properties from Shi et al [90]. This detector is the same as described in previous work [80]. The GOS scintillator was 0.29 mm thick with a pixel pitch of 392 $\mu$m.

### 4.2.4 Additional Fastcat Modelling

#### Bowtie and Flattening Filters

Additional models in Fastcat are applied to model some features of the scans. The kV bowtie filter was known to have a minimum thickness of 1.53 mm aluminum and a maximum thickness of 27.3

mm aluminum. The proprietary bowtie filter shape was unknown and estimated from the shape of a kV OBI air scan. With Fastcat's model of the kV imager spectra and the energy response of the detector, a weighted attenuation coefficient of aluminum was calculated for the kV OBI. This attenuation coefficient was then used to estimate the thickness of aluminum filtration present at each pixel. While an additional thickness of 1.53 mm of aluminum was added to each pixel to account for the base thickness of the bowtie filter. The maximum thickness of aluminum was calculated to be 28.3 mm using this method. This thickness is seen to be nearly equivalent to the specified thickness plus an additional factor accounting for a non-perpendicular path through the filter. Fastcat's kV beam was then filtered by the calculated amount of aluminum at each pixel during simulation. Additionally, the MC scatter for the kV image was recalculated to include the bowtie filter's effect on scatter. To account for the heel effect in the beam, tungsten filtration in the shape of a linear ramp increasing in the cathode-anode direction with a maximum height of 0.1 mm was added.

The thickness of the MV flattening filter was also estimated. In this case, the Fastcat beam was attenuated by a gaussian tungsten flattening filter. The height and standard deviation were chosen such that a profile through the reconstructed CBCT best matched experimental CBCTs.

### Anti-scatter Grid

To correctly model the kV OBI a model for the anti-scatter grid (ASG) was introduced. The model is based on measurements made by Wiegert *et al.* [115] Primary transmission factor and scatter transmission factors from the 44r10 ASG discussed in the paper were used. These factors are 0.76 and 0.37, respectively. Primary fluence reaching the detector in the Fastcat simulation was multiplied by the primary transmission factor. The scatter transmission factor was used to separate the scatter into two portions handled by the simulation as either accepted or attenuated, respectively. The first portion was accepted by the detector while the second portion was assumed to be incident on the ASG at a 12 degree angle. Where 12 degrees was the mean angle of scatter incidence from Weigert *et al.*'s work. This second portion was filtered by 173 $\mu$m of lead, which is the path length through the 36 $\mu$m lamella at an angle of 12°. The number of particles in these two portions were calculated such that the total Fastcat scatter transmission factor agreed with the theoretical.

### Virtual Phantom

A virtual version of the Catphan phantom was created. The virtual phantom was voxelized into 1024 pixels horizontally (h) 1024 pixels vertically (v) with voxel dimensions of 0.195 mm (h), (v) and a slice thickness of 0.313 mm. The slice thickness was made larger than axial voxel dimensions as the phantom is cylindrically symmetric and the slice thickness has no effect on simulation results. Materials linear attenuation coefficients were calculated using the material compositions and densities in the Catphan documentation. Densities of Delrin and the inner and outer body materials of the phantom were estimated as data was not available on their exact composition. Delrin's composition was estimated to match the attenuation coefficient available on the manufacturer site. The two body materials were estimated using the composition of acrylic and densities that would give the materials the relative electron densities reported in Star-Lack *et al.* [17].

### 4.2.5 Dose Comparison

A validation of dose linearity was performed. Four CBCTs at increasing doses were acquired experimentally for both the kV and the MV setups. Doses were measured using machine CTDI for the kV CBCTs with CTDIs of 5.27, 7.03, 10.55, and 21.1 with a 16 cm diameter CTDI phantom. Four MV CBCTs were acquired with machine MU values which were 75, 100, 150, and 300 MU. The dose in Fastcat was adjusted such that the average CNR over all inserts in the Catphan phantom agreed with that of the experimental CBCT with the lowest dose averaged. This Fastcat dose was then multiplied by factors of 1.5, 2, and 4. Agreement between average CNR was then compared between these Fastcat simulations and the experimental CBCTs.

An MC validation of the Mean phantom dose for a single projection was performed. Mean phantom dose for a single projection was calculated in Topas [69] using an MC model of the Catphan phantom with $2{\times}10^8$ initial photons. This dose was compared to the dose calculated in Fastcat for the same number of photons. These simulations used the Geant4 Penelope physics list and a particle range cutoff of $5\mu$m. Simulations were run on a linux desktop computer with 8 Intel Skylake CPUs. No variance reduction techniques were used. Two simulations were run in total, one with the 6 MV Varian phasespace file and one with an analytical 100 kVp x-ray spectrum filtered by 2.7 mm of aluminum, 0.89 mm titanium, and an aluminum bowtie filter. Both simulations measured the mean phantom dose to virtual Catphan 504 phantom.

The mean dose values from the MC simulations were used to perform a back of the envelope calculation to check that values were consistent between Fastcat kV and MV mean phantom doses and linac values reported as CTDI and in MUs, respectively. A conversion factor between the number of Fastcat photons to Fastcat mean phantom dose was estimated using the ratio of the dose scored in the MC simulations to the number of MC-simulated photons. The conversion factors were multiplied by the number of photons in the kV and MV experimental Fastcat simulations to get the mean phantom dose per projection and finally by the number of experimental projections to get the mean phantom dose for the total simulation.

### 4.2.6 Validation Metrics

#### Detector MTF

Detector modulation transfer function (MTF) was measured using a slanted virtual slit of 0.3 mm in Fastcat. The method of measuring the detector MTF is discussed in previous work [80]. Detector MTF was compared to experimental results from previous works of Howansky *et al.* and Shi *et al.*

[116, 90].

### CBCT Contrast, CNR, and NPS

To validate Fastcat, image quality was compared between Fastcat and experimental images. Original units of attenuation coefficients in $cm^{-1}$ for both images were first converted to Hounsfield Units (HU) by subtracting the CT value of water in the image and scaling by the difference between water and air regions in the image.

$$HU = 1000\frac{im - \mu_{water}}{(\mu_{water} - \mu_{air})} \tag{4.1}$$

Where $im$ is the reconstructed image and $\mu_{water}$ and $\mu_{air}$ are the linear attenuation coefficients of water and air, respectively. For Fastcat, water values were taken from a separate scan of a water phantom. Contrast was compared using regions of interest (ROIs) in each insert of the CTP404 sensiometry module. Regions of interest were made slightly smaller than the inserts to avoid partial volume effects. The mean value over sixteen slices was used as the contrast value while the standard deviation of the contrast in the sixteen slices was used as an estimate of the standard deviation. Contrast to noise ratio (CNR) was measured using the same ROIs. The standard deviation of each ROI was used as an estimate of the noise. Contrast, again, was measured against water, the CNR was then

$$CNR = \frac{\mu_{ROI} - \mu_{water}}{\sigma_{ROI}} \tag{4.2}$$

Where $\mu_{ROI}$ and $\sigma_{ROI}$ are the mean and standard deviation of each ROI. CNR was measured in each slice over sixteen slices, with the mean value used as a final estimate of the CNR. The standard deviation of the sixteen slices was used as an estimate of the standard deviation of the CNR.

Radially averaged noise power spectrum (NPS) was calculated using 50 randomly sampled 64 × 64 pixel regions inside a region of 100 × 100 pixels at the center of the CTP 404 module for each of the experimental and Fastcat images. NPS was calculated in each slice by averaging the squared 2D Fourier transform radially and the results were averaged over four slices to reduce noise.

## 4.3 Results

### 4.3.1 CBCT Image Comparison

Experimental and Fastcat simulated CBCTs were compared. Figure 4.2 shows a comparison of 100 kVp and 6 MV experimental and Fastcat images, respectively. Qualitatively, the experimental and Fastcat-simulated CBCT are similar. The effect of the bowtie filter can be seen in the 100 kVp CBCTs which are qualitatively uniform. The effect of the flattening filter can be seen in the 6 MV images where beam hardening artifacts can be seen.

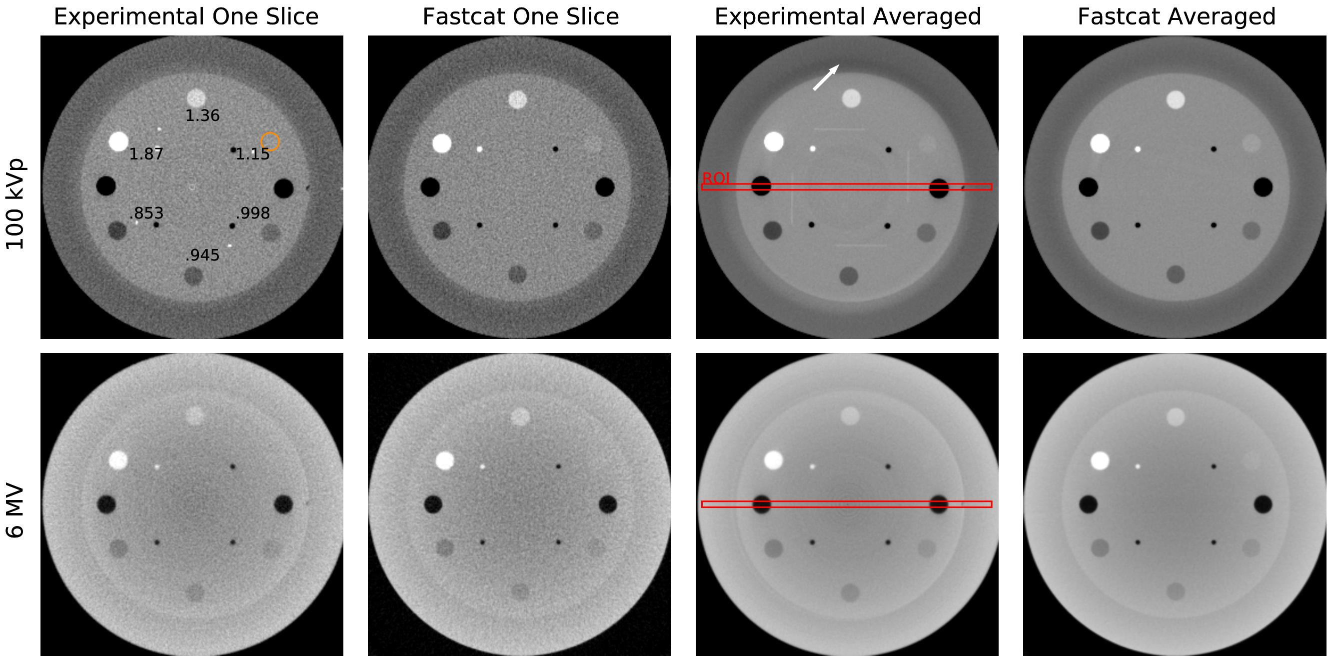

Figure 4.2: A qualitative comparison between experimental CBCTs and Fastcat simulations averaged over 16 slices and for one CBCT slice, respectively. The relative electron densities of the inserts are shown in black. The mean of the ROI shown in red are plotted in Figure 4.3. An arrow indicates a crescent artifact from mechanical misalignment. The small dark spot on the right of the experimental phantom is an alignment marker not included in the Fastcat simulation. Window (W) and level (L) of 1000/300.

Different features can be seen in the averaged CT images in Figure 4.2. The 100 kVp image shows a radial uniformity thanks to the presence of the bowtie filter. However, the image is not completely uniform. The bowtie filter ends just inside the lower density outer layer of the Catphan. This causes non-uniformity in the phantom in this lower density region. A difference between the experimental and Fastcat kV images is a large crescent artifact denoted by a white arrow in Figure 4.2. The effect of this artifact can also be seen at the edges of the kV profile in Figure 4.3. In the Varian documentation such artifacts are said to be related to mechanical misalignment between the detector, x-ray tube and bowtie filter. Since Fastcat does not account for this sort of artifact it is not present in the Fastcat image. A dark circle artifact is also present at the center of the 100 kV experimental image. Ring artifacts due to pixel non-uniform response were prevalent in this area and this artifact is due to the accumulation of these ring artifacts and has no physical significance.

In the 6 MV image, the flattening filter causes the beam to be harder in the center of the phantom than the periphery. This leads to cupping in the center of the phantom as seen in both images. Some

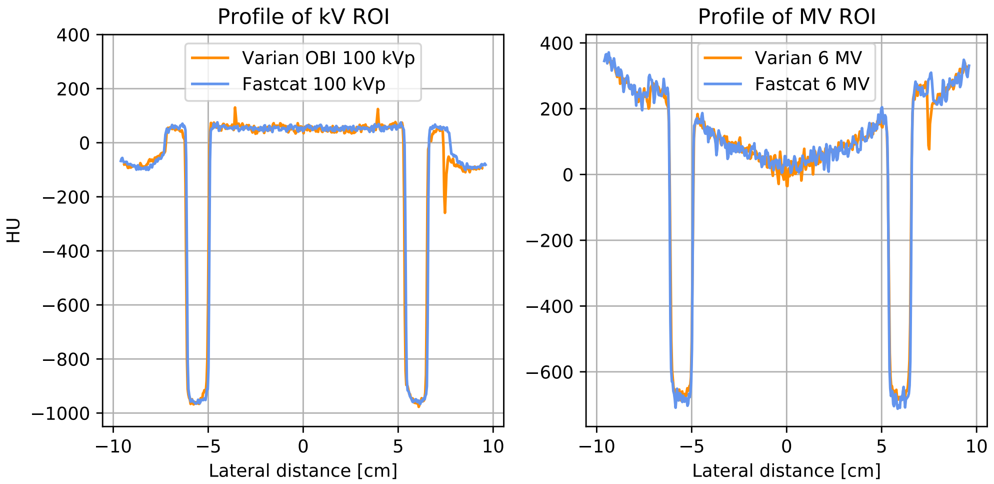

Figure 4.3: Profiles over the ROI marked in red in Figure 4.2. The two peaks at -4/4 cm and the valley at 7 cm correspond to wire ramps and alignment markers in the experimental phantom, respectively. These features were not included in the Fastcat simulations.

difference is seen between MV profiles in the center of the phantom in Figure 4.3. This difference may be from ring artifacts or due to the estimation of the flattening filter as Gaussian.

Overall, the contrast is visibly similar in between both sets of images in Figure 4.2. The 100 kVp image has high contrast, clearly differentiating all of the inserts while the 6 MV image has low contrast reflecting the lower number of photo-electric interactions at this energy.

Table 4.1: kV and MV HU values in CTP404 module, values are in HU while standard deviations are in parentheses.

| | PMP | LDPE | Polystyrene | Acrylic | Delrin | Teflon |
|---|---|---|---|---|---|---|
| kV Exp. | -204 (91) | -102 (102) | -48 (92) | 135 (91) | 357 (105) | 995 (87) |
| kV Fastcat | -192 (103) | -104 (91) | -62 (93) | 133 (97) | 356 (102) | 1005 (102) |
| Abs. Diff. | 12 | 2 | 14 | 2 | 1 | 10 |
| MV Exp. | -70 (124) | 14 (136) | 74 (131) | 219 (129) | 397 (121) | 847 (115) |
| MV Fastcat | -73 (129) | 17 (126) | 65 (135) | 222 (124) | 398 (128) | 850 (144) |
| Abs. Diff. | 3 | 3 | 1 | 3 | 1 | 3 |

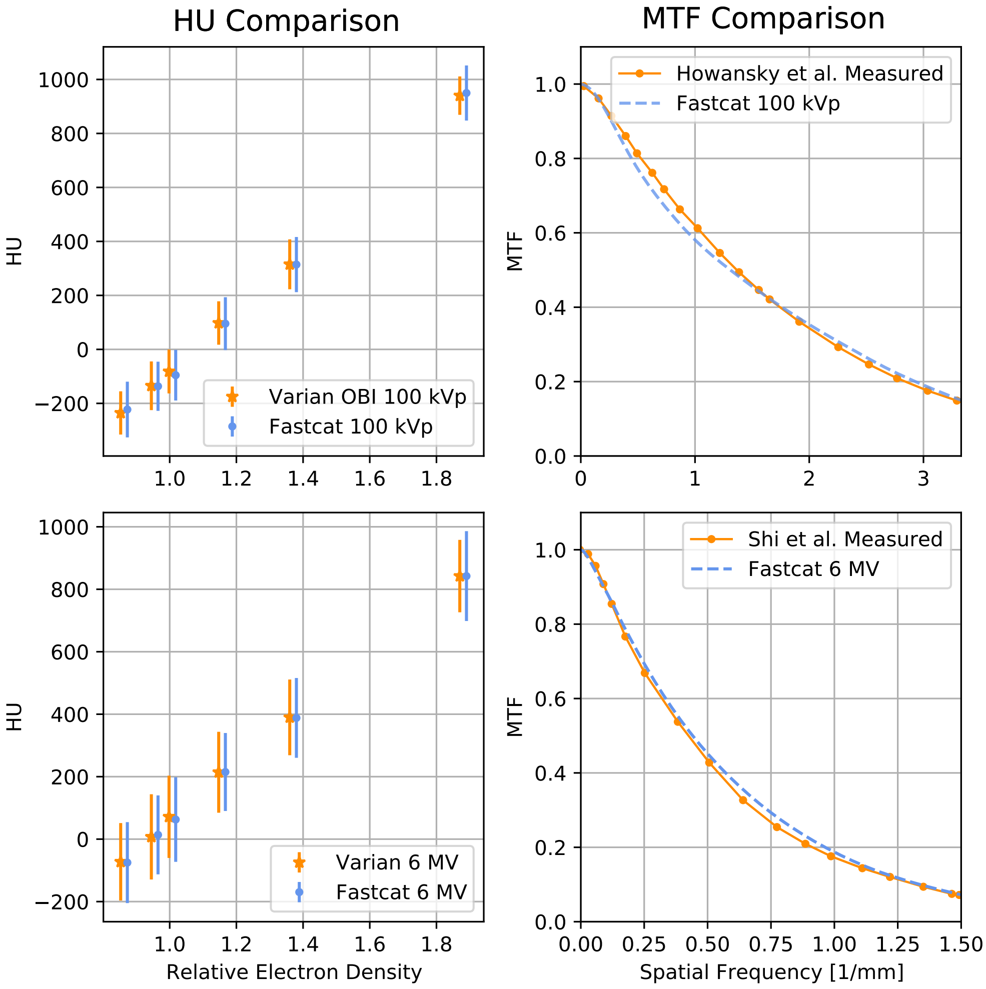

Figure 4.4: (L) A comparison is demonstrated between the experimental kV and MV CBCTs and the Fastcat simulations in terms of HU values in an experimental and virtual CTP404 module, respectively. (R) Comparison of detector MTFs calculated by Fastcat and based on experimental data presented by Howansky *et al.* [116] and Shi *et al.* [90] for the kV and MV detector, respectively. The Fastcat 6 MV MTF curve shown is similar to work from Figure 3. in O'Connell and Bazalova-Carter [80] with a slightly larger pixel size of 0.392 mm rather than 0.336 mm.

### 4.3.2 Contrast and MTF

Looking quantitatively at these images, there is also close agreement. In Figure 4.4, HU values are compared between experimental and Fastcat CBCT images. The HU values in the inserts are shown in Table 4.1. HU values for the kV and MV images agreed within 14 and 9 HU values, respectively. The kV HU values were all within the range defined in the Catphan documentation. kV and MV detector MTF was also compared to measurements made by and Shi *et al.*, respectively. The measurements for the CsI detector were within 4.2% of measurements by Howansky *et al.* with an average RMSE of 1.7%. MTF deviated mostly at frequencies between 0.5-1.3 $\mathrm{mm}^{-1}$ while agreeing closely at larger spatial frequencies. The MTF measurements for the GOS detector were within 2.5% of measurements by Shi *et al.* agreeing well over all spatial frequencies with an average root mean squared error (RMSE) of 0.5% and a slightly higher MTF at spatial frequencies between 0.5-1.0 $\mathrm{mm}^{-1}$.

### 4.3.3 CNR and Dose

CNR was examined in each insert for each of the images seen in Figure 4.2. The CNR results are shown in Figure 4.5. CNR values are summarized in Table 4.2. CNR agreed within 0.4 and 0.2 for the kV and MV images, respectively. CNR as a function of dose was examined as seen in Figure 4.5. Fastcat CNR values were seen to have average RMSE of 2.6% and 1.4% for kV and MV images, respectively. RMSE between experimental and Fastcat CNRs as a function of dose were seen to be 1.19% and 1.22%, respectively.

Table 4.2: kV and MV CNRs in CTP404 module, standard deviations are in parentheses.

| | PMP | LDPE | Polystyrene | Acrylic | Delrin | Teflon |
|---|---|---|---|---|---|---|
| kV Exp. | 6.1 (.55) | 6.7 (.62) | 6.9 (.72) | 7.9 (.50) | 8.9 (.56) | 12.0 (1.11) |
| kV Fastcat | 6.5 (.57) | 6.9 (.54) | 7.1 (.74) | 7.9 (.46) | 9.1 (.64) | 12.0 (.88) |
| Abs. Diff. | 0.4 | 0.2 | 0.2 | 0.0 | 0.2 | 0.0 |
| MV Exp. | 6.2 (.34) | 6.7 (.35) | 7.0 (.70) | 7.8 (.56) | 8.7 (.59) | 11.0 (.74) |
| MV Fastcat | 6.4 (.60) | 6.9 (.56) | 7.1 (.76) | 7.8 (.65) | 8.9 (.66) | 10.8 (.55) |
| Abs. Diff. | 0.2 | 0.2 | 0.1 | 0.0 | 0.2 | 0.2 |

### 4.3.4 NPS

NPS was examined in a 100 × 100 pixel region in the center of each of the images seen in Figure 2. NPS results are shown in Figure 4.6. NPS agreed within 11 and 14 $\mathrm{HU}^2\ \mathrm{mm}^3$ for the kV and MV images respectively. Fastcat and experimental NPS had average RMSEs of 7 and 9 $\mathrm{HU}^2\ \mathrm{mm}^3$ with a slightly larger discrepancy at higher spatial frequencies between 0.6 to 1 $\mathrm{mm}^{-1}$.

### 4.3.5 Dose and Speed

Dose was compared between MC simulations and Fastcat using $2 \times 10^8$ initial photons. Dose was calculated for both the kV and the MV CBCT simulated acquisitions. The mean dose to the entire

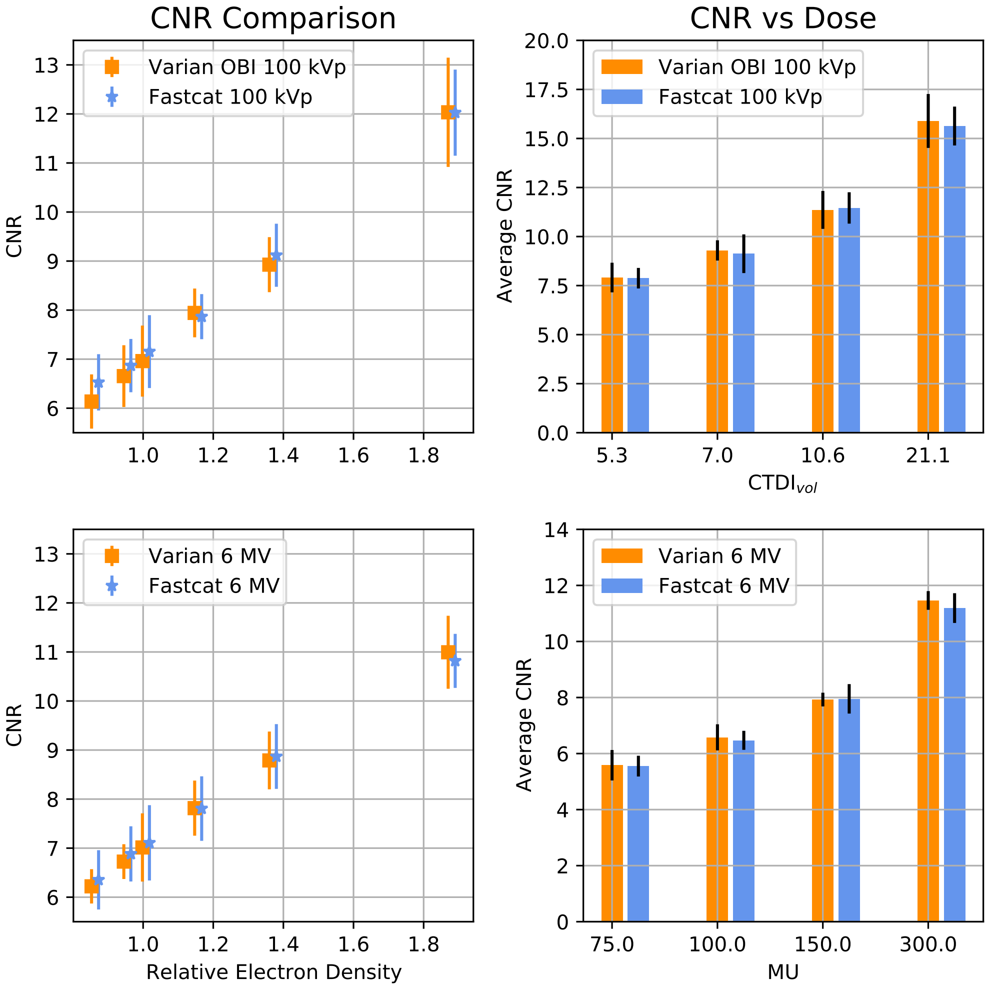

Figure 4.5: (L) A comparison is shown between the Varian Truebeam kV and MV CBCTs and the Fastcat simulated CBCTs in terms of CNR in an experimental and virtual CTP404 module, respectively. (R) CNR is compared between Truebeam CBCTs and Fastcat CBCTs as a function of dose.

Catphan for a single projection with the kV beam were 0.416 and 0.426 $\mu$Gy for the MC and Fastcat calculation, respectively. The mean doses to the Catphan for the MV beam were 7.31 and 7.19 $\mu$Gy for the MC and Fastcat calculation, respectively. Thus, there were differences of 2.4% and 1.6% between Fastcat and MC dose calculations for kV and MV, respectively. By matching Fastcat and experimental CNRs, the number of Fastcat photons per projection was found to be $9.59 \times 10^{10}$ and $1.42 \times 10^{11}$ for the kV and MV images. As a result, the Fastcat mean phantom doses for 887 and 493 projections were 17.52 mGy and 2.566 Gy for the kV and MV simulations, respectively. These values were consistent with the CTDI of 21.2 mGy and 300 MU reported by the linac for the kV and MV simulations, respectively.

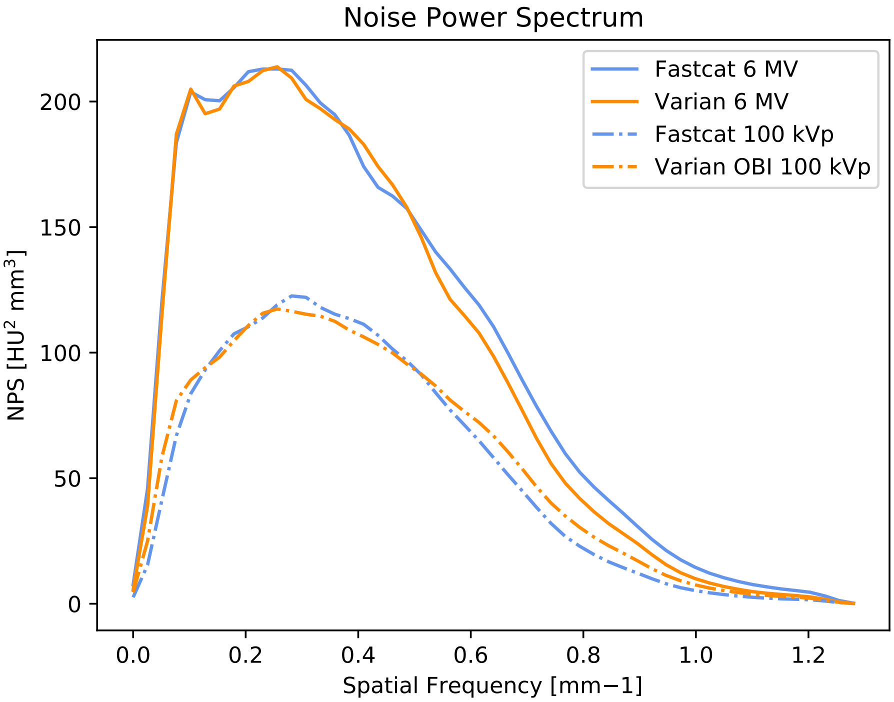

Figure 4.6: NPS in the center of the Catphan 404 module. Calculated from 50 separate 64 × 64 pixel ROIs in a 100 × 100 pixel area in the center of the phantom and averaged.

Simulation times were recorded for four Fastcat simulations to estimate the relationship between computation time and the number of projections. Results are shown in Figure 4.7. Computation time scaled linearly with the number of projections for the MV and kV Fastcat simulations with both linear fits having $R^2$ values above 0.999. kV simulations are faster, scaling at 0.37 s/projection while MV simulations scaled at 0.55 s/projection. kV simulations are seen to be more computationally efficient since only ten discrete energies are simulated between 10 and 100 keV while the MV simulation used 18 energies between 10 keV and 6 MeV. All simulated phantoms contained 12 different materials.

The phantom in this study was low resolution in the $z$ axis to reduce simulation times. An increase in simulation time can be expected for higher resolution phantoms. For example, using the same parameters as the 6 MV beam in Figure 6 which took 74 seconds to simulate 493 projections, using an isotropic phantom with a voxel size of 0.195 mm takes 108 seconds.

## 4.4 Discussion

We present and perform a two energy validation of Fastcat, a free open-source CBCT simulator against CBCTs acquired on a Varian Truebeam linac. This simulator performed simulations of

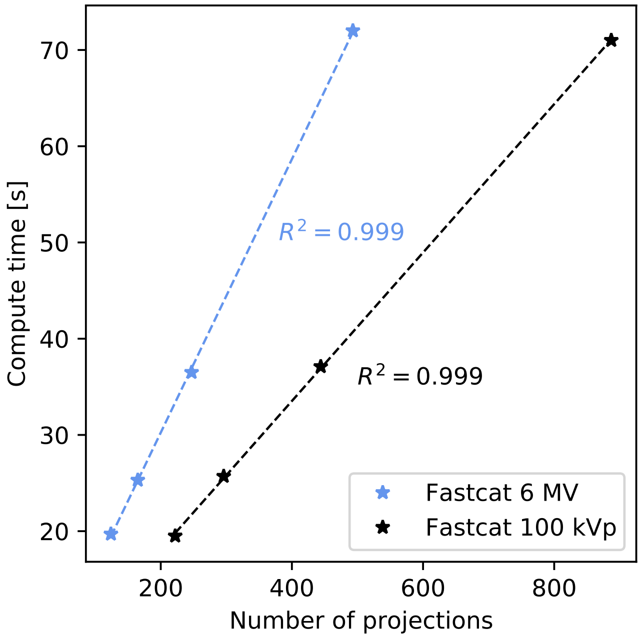

Figure 4.7: A time comparison as a function of the number of projections in a Fastcat CBCT simulation.

high-resolution voxel based phantoms on a desktop computer with 16 GB of memory and an Nvidia RTX 2070 GPU. Simulation times were on the order of a minute to simulate the images used in the validation. Simulated CBCT images demonstrate unprecedented accuracy for their speed, enabling novel application of CBCT simulation in research and clinical workflows. A comparison of Fastcat to four other simulation tools is discussed. DukeSim, CatSim, VOXSI, and gDDR were selected for comparison since they accept voxelized phantoms, use analytical methods to reduce simulation times, and were validated with experimental data.

Compared to the validation of other CT and CBCT simulators, the experimental validation of Fastcat is exceptional in its comprehensiveness and accuracy. The two energy validation presented, using very different imaging systems mitigates possible overfitting resulting from a validation on a single scanner as was conducted for DukeSim, CatSim, and gDRR. VOXSI provides an experimental validation at three tube potentials, however, it uses the same source and detector in each simulation. This might lead to uncertainty in extrapolating the simulator to different detectors and sources, as simulation parameters may be unintentionally specific to the one setup.

Fastcat was experimentally validated with the ubiquitous Catphan 504 phantom and standard imaging metrics such as HU values and CNR. Of the simulation tools discussed, only VOXSI is experimentally validated using a common phantom while other tools were validated using only a single material. VOXSI simulations were within 42 HU of a Gammex RMI 467 tissue characterization phantom (Gammex, Middleton, WI), while Fastcat which was within 14 HU of a comparable Catphan CTP404 module. DukeSim displayed simulated CT images of a Mercury phantom [117], however neither contrast nor CNR comparisons were shown. This Fastcat validation presents CNR agreement to experimental data with an average RMSE of 2.6% and 1.4% in the CTP404 module inserts for kV and MV images, respectively.

Unique among the simulation tools discussed, Fastcat demonstrates agreement with detector MTF. Values were within 4.2% and 2.5% of measurements for CsI and GOS detectors, respectively. CatSim and DukeSim use a simple estimation of detector spatial resolution based on neighbouring crosstalk. In reality, scintillating detectors have crosstalk that extends further than their nearest neighbors. Fastcat accounts for this based on the fastEPID framework [39] which found an 81 × 81 pixel OSF was necessary to simulate an accurate detector response. VOXSI and gDRR do not include simunelations of the spatial resolution.

Computational efficiency was paramount in Fastcat's methodology. As such, Fastcat's computational efficiency compares favorably to other CT and CBCT simulation tools. Direct comparisons currently remain unfeasible as simulation times depend on phantom resolution, processors, noise, and the number of projections, variables which are not always presented in the literature. Nevertheless, qualitative comparisons can be made by examining reported simulation times: Fastcat is estimated to have faster simulation speeds than gDDR, 1 projections of a gDRR high resolution anthropomorphic head phantom with isotropic 512 × 512 × 100 voxels with 0.976 $\text{mm}^2$ transverse dimensions and 2.5 mm slice thickness took 95.3 s on an Nvidia GTX 590 GPU. Analogously, Fastcat took 28 seconds to simulate 360 views of a similar resolution Catphan 504 phantom with a more powerful Nvidia RTX 2070 GPU. VOXSI is also less computationally efficient than Fastcat, taking 45 seconds to simulate a CT with 512 × 512 × 1 voxels, 1024 detectors, and 780 projections, on two Intel Xeon 2.67 GHz processors. Simulations in DukeSim invoke a GPU MC tool to calculate scatter, the scatter calculation speed and total calculation speed thus depend on the desired noise. A sample DukeSim CT simulation with a phantom of 1900 × 1900 × 1000 with isotropic voxels of 0.25 mm, 6912 projection images, and 47104 detectors, and $10^8$ MC photons per projection took about 10 minutes on 4 Nvidia Titan Xp GPUs. In this case the simulation of such a large phantom and the added aspect of the MC noise is considered too different from Fastcat to compare computational efficiencies.

Fastcat introduces a new CBCT simulation method that could be a useful research tool. While MC simulations can agree with experimental results to the level shown in this work, they are computationally expensive. Fastcat is computationally efficient such that imaging settings can be quickly explored. Fastcat also contains a complex enough simulation method to agree closely with experimental results in terms of contrast and CNR, as seen in this work. Fastcat could be used as a quick and accurate exploration tool to examine the benefit of many CBCT imaging protocols. Further confirmation of promising protocols could then be performed using established MC and demonstrated with experimental methods.

Fastcat could also be used in a clinical setting: A Fastcat model of a given linac can be constructed such that it agrees with clinical CBCT quality assurance (QA) through the use of the virtual Catphan phantom. This can be done by adjusting the beam energy, focal spot size, detector material, and other parameters. Unlike with MC models, due to its fast simulation times Fastcat could build scanner specific, virtual clinical datasets of hundreds of CBCT volumes of an anthropomorphic phantom overnight. With a calibration between the Fastcat CNR and machine dose these datasets could be used to estimate the correct imaging settings for a given clinical situation. Such as estimating the CTDI necessary to achieve a given soft tissue CNR for a patient of a specific size. Likewise, Fastcat could be used in conventional workflows. Fastcat, with the addition of a mapping between experimental DICOM voxel values into material compositions like that of Schneider *et al.* [74], could be used to simulate an MV CBCT from a kV CBCT, this would allow generation of MV beam's eye view images for the validation of a given treatment quickly from a given patient-specific CBCT acquired by the OBI.

Fastcat is unique in its simulation speed and accuracy. No other analytical CBCT simulator has shown such close agreement with experimental results, while no MC simulator has similar computational speed. Fastcat is limited, however, due to its dependence on pre-calculated data. Detector optical spread functions (OSFs), MV beams, and scatter kernels for different phantoms are stored in Fastcat. A simulation that uses a different detector, MV beam, or phantom than those available in Fastcat may need the additional step of simulating the necessary pre-calculated data in an MC application and be subject to new experimental validation. As an open-source simulator, ideally this new pre-calculated data could be uploaded by groups who use Fastcat, making a variety of commercial setups available and improving the simulator as a whole. Currently however, the type of accuracy shown in this work is only available for the Varian Truebeam EPID and Varian Truebeam OBI systems. An additional limitation is Fastcat's dose calculation methodology where dose can only be specified as a mean phantom dose. Further work will focus on allowing simulation doses to be specified in more common clinical units such as CTDI or specified in MU based on a specific reference depth and calibration distance as defined in the Fastcat documentation. Currently, noise can be matched between Fastcat and experimental data in a given phantom and a conversion factor between a given machine unit of dose and mean phantom dose can be calculated.

The method used to sample the NPS here was somewhat arbitrary, devised by the authors to mitigate measurement noise. While established approaches exist for detector NPS measurement, assessing NPS in the reconstruction space relies on numerous variables (reconstruction parameters, beam-hardening algorithms, bowtie, etc.), hampering precise quantitative evaluation. Hence, our focus was on describing differences between measures rather than their absolute values. Given the comparative nature of the images, the NPS parameters' absolute significance was considered less crucial, as the intention was relative comparison rather than adherence to a specific standard. While the full distribution of energies in the kV range between 10-100 keV in 10 keV intervals may be important for kV imaging, for MV imaging it is likely that fewer low energy bins could be used in the simulation for similarly accurate results. This can be specified in fastcat and would greatly improve the efficiency of the simulations.

The scatter specified in fastcat is ideally suited for head cases and symmetric anatomical regions. Less cylindrically symmetric areas would demand a detailed scatter modeling approach, possibly involving oblong cylinders mirroring regional anatomy properties. Extremely inhomogeneous or irregular regions could benefit from alternative approaches like GPU-based MC or kernel methods for scatter generation.

## 4.5 Conclusion

In this work we demonstrate experimental agreement between the Fastcat CBCT simulator and a Varian Truebeam linac. Fastcat 100 kVp and 6 MV CBCT images agreed closely with experimental kV and MV CBCT images, respectively. Close agreement was seen between experimental and Fastcat's HU values, detector MTF, dose, and CNR. CBCT simulation took 71 and 72 seconds for the kV and MV CBCT, respectively. We demonstrate the accuracy of a fast, free, open-source CBCT simulator that is well suited for the evaluation of new CBCT imaging protocols.

## 4.6 Acknowledgments

The authors would like to acknowledge Chelsea Dunning for the contribution to the name Fastcat. We would also like to thank Marios Myronakis for sharing the GOS MTF data with us. This research was enabled in part by support provided by WestGrid (www.westgrid.ca) and Compute Canada Calcul Canada (www.computecanada.ca). The work was partly funded by an NSERC Discovery Grant and the Canada Research Chairs program.

# Chapter 5

# Fastcat Simulation of Novel MV-CBCT

**Investigation of image quality of MV and kV CBCT with low-Z beams and high DQE detector**[1]

## 5.1 Introduction

Image guided radiotherapy (IGRT) is the state-of-the-art tool for reducing patient positioning errors during cancer treatment with radiation [119]. When designing a radiotherapy treatment plan, a number of margins around the visible tumors are added to the tumor volume. The final planning tumor volume (PTV) accounts for, among other things, difference in patient positioning during the treatment planning CT scan and during treatment delivered with a linear accelerator. This is generally minimized using IGRT where patient positioning is verified and adjusted based on a cone beam CT (CBCT) scan acquired on the linear accelerator just prior to treatment. CBCT image quality leads to better alignment, which in turn can lead to tighter PTV margins and increased normal tissue sparing.

IGRT is generally performed with kilovoltage (kV) x-ray on-board imagers (OBIs) mounted on the gantry of the linear accelerator at 90 degrees with respect to the megavoltage (MV) treatment beam. OBIs take advantage of the higher image contrast produced by kV CBCT [84]. However, an alternative approach is to use the megavoltage (MV) treatment beam for image guidance with the aid of an electronic portal imager (EPID). Benefits of this approach include high atomic number artifact reduction [85], less complex linear accelerators without the OBI equipment, and the availability of EPID dosimetry [82, 83]. Limits of this approach include the aforementioned reduction in image contrast compared to kV CBCT due to smaller variation between tissue attenuation coefficients in the MV range, as well as reduced detector quantum efficiency (DQE) due to the more penetrating MV beam. There have been extensive efforts to reduce these limitations.

To improve MV imaging quality, novel low atomic number (Z) beam targets have been examined to generate photon beams with higher fluence in the kV range. The use of aluminum and carbon

---

[1] This work was published in *Medical Physics* [118]

targets has been shown to improve image quality: Simulation studies show a 16-19% increase in contrast between an aluminum target and the default tungsten target for a 6 MV photon beam [23, 24]. Experimentally, Baek et al. showed that a gantry mounted aluminum target improved the limiting spatial frequency (f50) from 0.451 lp/mm to 0.745 lp/mm for a tungsten target 6 MV beam [25]. Additionally, Parsons et al. showed an increase in the contrast to noise ratio (CNR) in projection images of cortical bone by factors ranging from 3.7 to 7.4 between carbon and aluminum targets with 2.35 and 1.9 MV photon beams and the default 6 MV tungsten imaging setup [18].

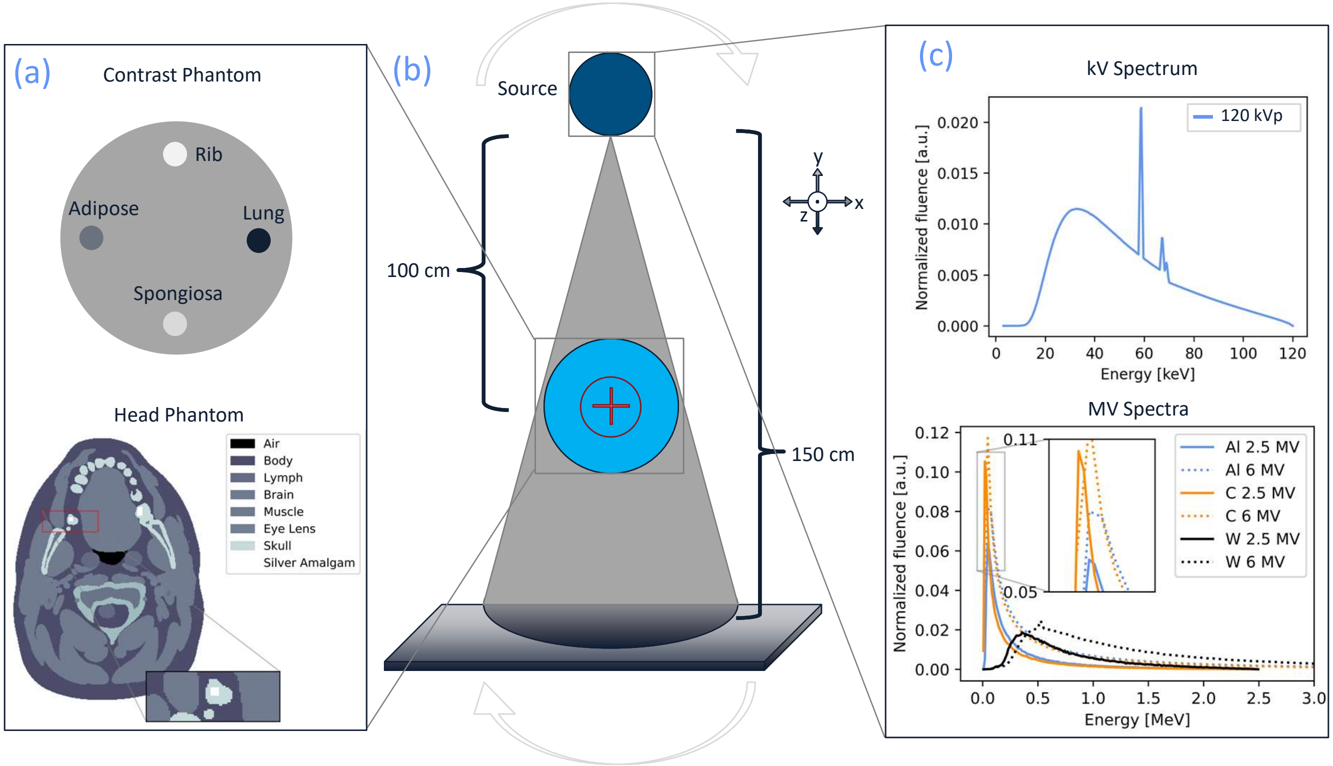

Figure 5.1: An overview of the simulation setup. a) The phantoms used in this work, the contrast phantom (top) and an XCAT head phantom with silver amalgam fillings (bottom, not all tissues shown in legend). b) The simulation geometry. c) The kV and MV energy spectra.

Furthermore, advances in MV EPID design have shown promise in improving MV image quality. Many MV EPIDs use a gadolinium oxysulfide (GOS) scintillator, which is opaque to its own scintillation photons. This limits the thickness of GOS detectors which in turn limits the quantum efficiency of the detector. Star-lack *et al.* examined cadmium tungstate (CWO) and bismuth germinate (BGO) detectors, which are higher Z materials and can be made thicker for MV photon detection. CWO was noted to have a 20-fold efficiency improvement over GOS with significantly higher stability and light yield than BGO [17]. Likewise, image quality improvement was seen using multi-layer GOS imagers with 2-4 times greater CNR than an equivalent single layer GOS detector [21].

Currently, these two approaches to improving MV imaging, the amelioration of detector efficiencies and introduction of low-Z targets, have remained largely separate. Likewise, direct comparison of the benefit of different imaging strategies in the literature remains challenging as different works have different combinations of voxel size, cone-beam size, phantom dose, focal-spot size and other imaging variables.

In this work we simulate image quality for combinations of novel MV beam target materials such as carbon and aluminum with different detector materials such as CWO. We compare these novel imaging methodologies with a standard kV imaging setup using a columnar cesium iodide (CsI) detector. We investigate whether the combination of novel MV beams and detectors can result in MV CBCT image quality approaching kV CBCT image quality.

## 5.2 Materials and Methods

### 5.2.1 Experimental Validation

FastCAT was validated against two CBCT images acquired with a Varian Truebeam linac; one using the 100 kVp on board imager with a CsI detector and another using a 6 MV therapy beam with a GOS detector. HU values are compared between the two sets of images for each insert as a function of electron density. All Fastcat HU values showed agreement within the 99% confidence interval of experimental values. Detector MTF comparisons to previous works displaying agreement within 5%.

### 5.2.2 Fastcat

The Fastcat simulation tool [80, 102] is a hybrid Monte Carlo application that was used to simulate the CBCT images presented in this work. Fastcat was demonstrated to be an ideal tool for the rapid and accurate assessment of the modulation transfer function (MTF) and contrast to noise ratio (CNR) of MV and kV imaging setups. Agreement has previously been demonstrated between Fastcat and a Varian Truebeam linac (Varian Medical Systems, Palo Alto, Ca) for both a 100 kVp CBCT acquired on the OBI as well as a 6 MV CBCT acquired using the EPID [102]. Specifically, CNR in inserts of a Catphan CTP404 (The Phantom Laboratories, Salem, NY) module had an average RMSE of 2.6% and 1.4% between Fastcat and experimental measurements for the 100 kVp and 6 MV CBCTs, respectively. Likewise, Fastcat detector MTFs were assessed to be within 4.2% and 2.5% of experimental values for the kV and MV detectors, respectively.

The kV imaging setup used in the study is based on the specifications of the Varian Truebeam OBI. Fastcat's kV model includes an aluminum bowtie filter with a minimum thickness of 1.53 mm and a maximum thickness of 27.42 mm with a shape defined by the relative intensity of an experimental air scan. An anti-scatter grid (ASG) is also used based on the measurements of Wiegert et al. [115] which define the primary and scatter transmission factors for the 44r10 ASG used with the CsI detector of the Varian Truebam OBI. Primary and scatter transmission factors were 0.76 and 0.37, respectively.

Primary fluence in the Fastcat simulation was scaled by the primary transmission factor. A fraction of the scatter was attenuated by 173 $\mu$m of lead such that the transmission factor was only 0.37. 173 $\mu$m of lead was used as it is the path length through the 36 $\mu$m lamella at the 12° mean angle of scatter incidence.

Fastcat combines TIGRE GPU raytracing [95] with Monte Carlo scatter kernels and detector optical spread functions into a fast and accurate CBCT simulator. The CBCT geometry followed a 100 cm source axis distance (SAD) and 150 cm source to detector distance (Figure 5.1b).

### 5.2.3 Phantoms

Two phantoms were simulated: a contrast phantom and a head phantom. The contrast phantom was a modified version of the 16 cm diameter Catphan 404 module (The Phantom Laboratory, Salem NY) including 12 mm diameter inserts composed of deflated lung, rib and spongiosa bone, and adipose (Figure 5.1a top) with material composition as defined by ICRU-44 [94]. Contrast was defined relative to the phantom body which was composed of muscle.

The head of the XCAT [75] phantom (Figure 5.1a bottom) was used in this study as it has a small enough radius to fit in the field of view of a single CBCT scan. A 512 × 512 × 200 voxel phantom was generated with voxel dimensions of 0.5mm × 0.5mm× 3.12mm. Energy dependent attenuation coefficients were generated by assigning compositions from ICRU-44 [94] to the XCAT tissues in the head phantom. Additionally, 1 and 1.5 mm rectangles of silver amalgam were added to two XCAT phantom molars to simulate dental fillings as seen in the bottom of Figure 1 a). Scatter was approximated in the simulations by the scatter generated from a 16 cm water cylinder.

### 5.2.4 CBCT image generation and reconstruction

To generate CBCT images, 360 views were taken at equally spaced angles between 0 and 360 degrees for each scan, images were reconstructed using the FDK algorithm [96] with a hamming filter for the contrast phantom. All scans were simulated to have noise consistent with a 7 mGy imaging dose. Doses were calculated using the Fastcat dose calculation engine. CBCT image simulations took, on average, 64 and 87 seconds on a Nvidia GeForce RTX 2070 GPU (Nvidia Corp., Santa Clara, CA) for the contrast phantom and head phantom, respectively.

xspecgen [87], an open source spectrum generator for kV x-ray tubes written in python (version 3.6). Xpecgen has methods for attenuating spectra, calculating half value layers and a python tk GUI which forms the backbone of Fastcat. Default simulation geometry can be seen in Figure 5.1: A cone beam collimated to 16 cm$^2$ at isocenter impinges on a 16 cm diameter cylindrical phantom source at source-to-detector distance (SSD) of 1.52 m and source-to-axis distance (SAD) of 1 m.

Table 5.1: Target thicknesses for MV imaging beams.

| | Tungsten (Varian Truebeam) | Aluminum | Carbon |
|---|---|---|---|
| 2.5 MV | 2.3 mm | 6.7 mm [89] | 7.6 mm [18] |
| 6 MV | 5 mm | 8 mm [25] | 9.9 mm [18] |

### 5.2.5 X-ray beams

The kV spectrum modelled was a 120 kVp beam with a 12-degree tungsten anode, 3 mm inherent aluminum filtration and 0.89 mm titanium beam hardening filtration were added to match the standard filtration of the imaging system. The spectrum was simulated in Fastcat by means of xpecgen [87]. In addition, multiple MV x-ray spectra were calculated in EGSnrc/BEAMnrc [88] using a variety of target materials (carbon, aluminum, and tungsten) and beam energies (2.5, 6 MV) (Figure 5.1c). The thicknesses of the beam targets were based on experimental targets and are summarized in Table 5.1.

### 5.2.6 Detectors

Table 5.2: Main detector parameters.

| | Septa | Scintillator thickness | Material | Pixel size |
|---|---|---|---|---|
| CWO | Yes | 15 mm [17] | $CdWO_4$ | 0.784 mm |
| CsI | No | 0.45 mm [91] | CsI:Tl | 0.784 mm |
| GOS | No | 0.29 mm | $Gd_2O_2S$:Tb | 0.784 mm |

Detectors with scintillators of CWO, CsI, and GOS were modelled. The detector optical simulation method is described in detail in O'Connell and Bazalova-Carter [80] as well as detailed descriptions of the detector materials and properties. A brief description of the detectors can be found in Table 5.2.

The three different detectors have different methods of preventing optical spread in the scintillators. The CWO detector is made up of separate pixels separated by aluminized mylar reflective septa to prevent light escaping a given pixel. The CsI detector has a columnar crystal geometry such that scintillated light reflects internally in a given column and prevents lateral spread of scintillation photons in the detector. Conversely, the GOS detector attenuates its own scintillation photons preventing their spread laterally in the detector but also limiting the thickness of the detector as large detectors would decrease efficiency. To improve efficiency in the GOS detector a copper build-up plate is found directly in front of the GOS crystal to provide more secondary electrons incident on the detector and thus a higher efficiency.

[40] CsI detector simulations were performed similarly to the CWO and GOS detectors in Geant4

[71, 38] extended by Topas [69] using Geant4 Optical and Penelope physics modules and a range cut of 0.5 $\mu$m for all particles. CsI detector response was simulated to the default sixteen Fastcat energies between 30 and 6000 keV as well as for 10 and 20 keV energy bins. These two extra energy bins were added for CWO and GOS detectors as well to fully describe the response of the detectors optical spread function in the kV range when using the fastEPID [39] method of calculating the point spread function. To reduce computation time 600 photons per MeV were used as the scintillation yield for CsI. This reduction in scintillation has not been seen to decrease the accuracy of detector simulations [40].

### 5.2.7 Image Quality Metrics

MTF for different beam detector combinations were modelled in the manner described in O'Connell and Bazalova-Carter [80]: The monoenergetic detector optical spread functions (OSFs) were weighted by the beam energy-spectrum to create a point spread function (PSF). This PSF was then convolved with an idealized 0.1 mm wide slit angled at 1.5 degrees to generate a line spread function (LSF) as described in the work of Fujita *et al.* [120]. This LSF was then presampled to estimate the MTF.

CBCT image contrast was measured in the inserts of the contrast phantom for the 120 kV, 2.5 MV and 6 MV carbon and aluminum target beams. All contrasts were measured relative to the phantom body which was composed of muscle tissue. We denote the average HU value from this region $\mu_{body}$ and the value from the insert $\mu_{insert}$. CNR was measured relative to the same region using the standard deviations $\sigma_{insert}$ and $\sigma_{body}$ as

$$C = \frac{\mu_{insert} - \mu_{body}}{\mu_{body}} \times 100\% \tag{5.1}$$

Similarly, contrasts to noise ratio was measured relative to the same region using the standard deviations $\sigma_{insert}$ and $\sigma_{body}$ as

$$CNR = \frac{\mu_{insert} - \mu_{body}}{\sqrt{\sigma_{body}^2 + \sigma_{insert}^2}} \tag{5.2}$$

CNR was bootstrapped to generate a 99% confidence interval.

## 5.3 Results

Results for kV and MV beams and all detectors in terms of MTF, CNR and head phantom images are presented in the following sections. The results from the aluminium target were very similar to the carbon target in all metrics and therefore the aluminium target results are not shown. Additionally, heat transportation requirements limit feasibility of imaging with aluminium targets [18], making carbon targets a better option in this case.

Table 5.3: Detector optical parameters [17, 90, 92]

| | Density ($g/cm^3$) | Material | Thickness (mm) | Abs. length (cm) \| Refr. ind. | Reflectivity |
|---|---|---|---|---|---|
| (1) Carbon Fiber | 1.62 | C | 2.5 | – | – |
| (2) Foam | 0.05 | C | 33.1, 25.0 | – | – |
| (3) Vikuiti ESR | 1.05 | CH | 0.065 | 0.01 | 0.98 |
| (4) Scintillator Pixel | 7.9 | $CdWO_4$ | 15 | 125 \| 2.25 | – |
| (5) Pixel Glue | 1.0 | Epoxy | 15 | 100 \| 1.47 | – |
| (6) Pixel Septa | 2.7 | Al Mylar | 15 | 0.001 | 0.88 |
| (7) Meltmount Glue | 1.0 | $C_{21}H_{25}ClO_5$ | 0.01 | 300 \| 1.7 | – |
| (8) Mylar | 1.38 | $C_{10}H_8O_4$ | 0.065 | 100 \| 1.65 | – |
| (9) AMFPI | 2.6 | $SiO_2$ | 1 | 0.001 \| 1.70 | – |
| (10) Fiberglass | 1.85 | $SiO_2$ | 0.6, 6.0 | – | – |
| (11) Copper buildup | 8.9 | Cu | 1 | – | – |
| (12) GOS phospor | 4.59 | $Gd_2O_2S$:Tb | 0.29 | 43 \| 2.3, 1.0 (binder) | – |
| (13) Al alloy | 2.8 | Al | 1 | – | – |
| (14) Pb alloy | 10.95 | Pb | 3 | – | – |
| (15) Graphite | 2.26 | C | 1 | 0.001 | 0.88 |
| (16) CsI | 4.51 | CsI:Tl | 0.9 | 1.25 \| 1.8 | – |
| (17) Columnar CsI | 4.51 | CsI:Tl | 3.60 | 1.25 \| 1.8 | – |

### 5.3.1 Detector MTF

The MTF for the three detectors is presented in Figure 5.2. In all cases the 120 kVp beam resulted in the highest MTF at all spatial frequencies for a given detector. Likewise, in nearly all cases the highest energy beam, the 6 MV tungsten target resulted in the lowest MTF. For MV beams the CsI detector had the highest MTF compared to the other detectors. For the kV beam the CWO detector resulted in the highest spatial resolution at low frequencies while the CsI detector resulted in better spatial resolution at high frequencies. The CWO spatial resolution dropped off due to the Nyquist frequency enforced by the detector septa which were only present in the CWO detector. Conversely, the CWO detector had the worst spatial resolution in all cases other than the 120 kVp beam, as mentioned above.

### 5.3.2 Contrast

Some sample contrast phantom CBCTs are shown in Figure 5.3 while CNR results for rib bone, lung, adipose, and spongiosa derived from CBCT images of the contrast phantom for the 120 kVp beam, the 2.5 MV and 6 MV beams with carbon and tungsten target and all three detectors are shown in Figure 5.4. CNRs for all materials were seen to decrease with average beam energy for all detectors. The highest CNRs were for the CWO detector with the 120 kVp beam; CNRs were 53.1, 47.9, 10.2, and 21.1 for the rib bone, lung, adipose, and spongiosa, respectively. CNRs for the CWO detector

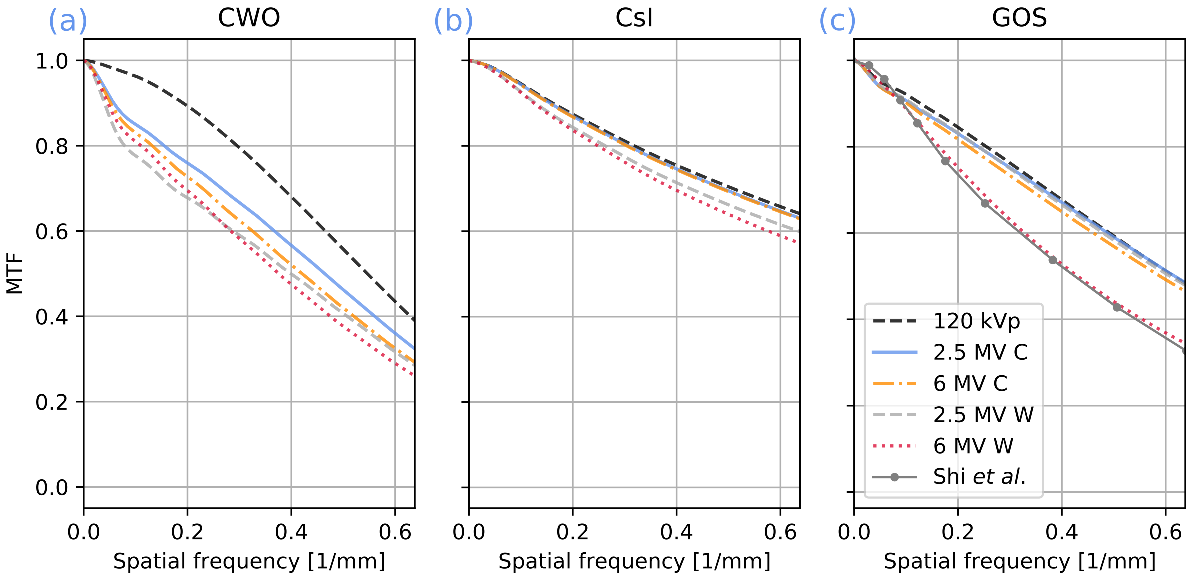

Figure 5.2: The MTF of the CWO (a), CsI (b), and GOS (c) detectors as a function of the 120 kVp beam and the 2.5 MV and 6 MV carbon and tungsten target beams. MTFs were calculated from the presampled line spread function of an angled slit. Experimental MTF calculated by Shi *et al.* [39] for the GOS detector at 6 MV tungsten target beam is displayed in (c) which uses the angled slit MTF calculation method off of which all other measurements are based. Plots are cropped at 0.63 1/mm, the Nyquist frequency of the CWO detector.

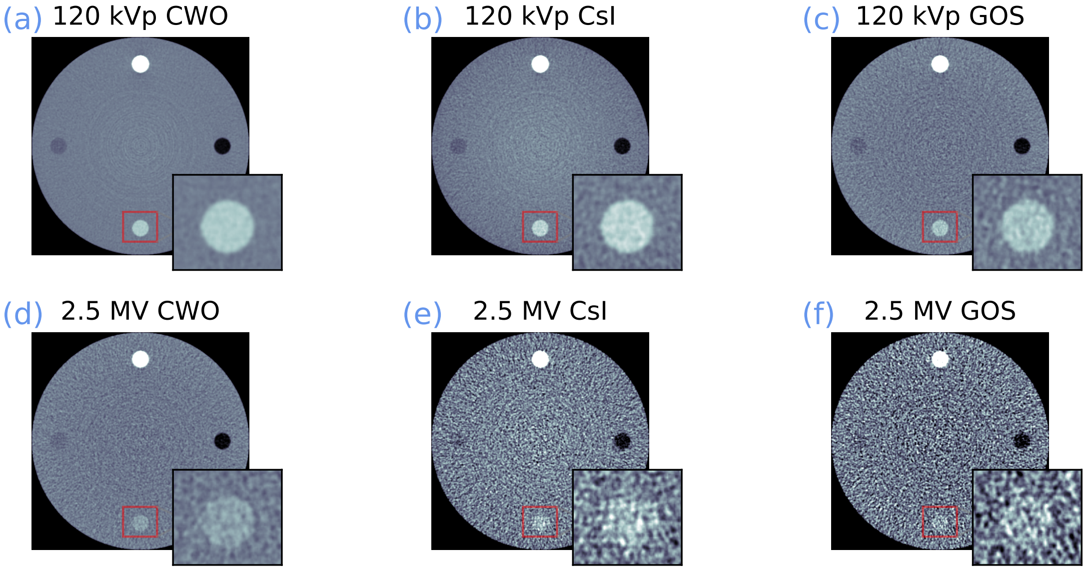

Figure 5.3: Simulated CBCT images of the contrast phantom reconstructed with the CWO (a,d), CsI (b,e) and GOS (c,f) detectors for the 120 kVp (a-c) and 2.5 MV carbon (d-f) beams (W/L 800/0 for images). All images were reconstructed using the FDK algorithm from 360 views with an imaging dose of 7 mGy. The inset shows the spongiosa insert.

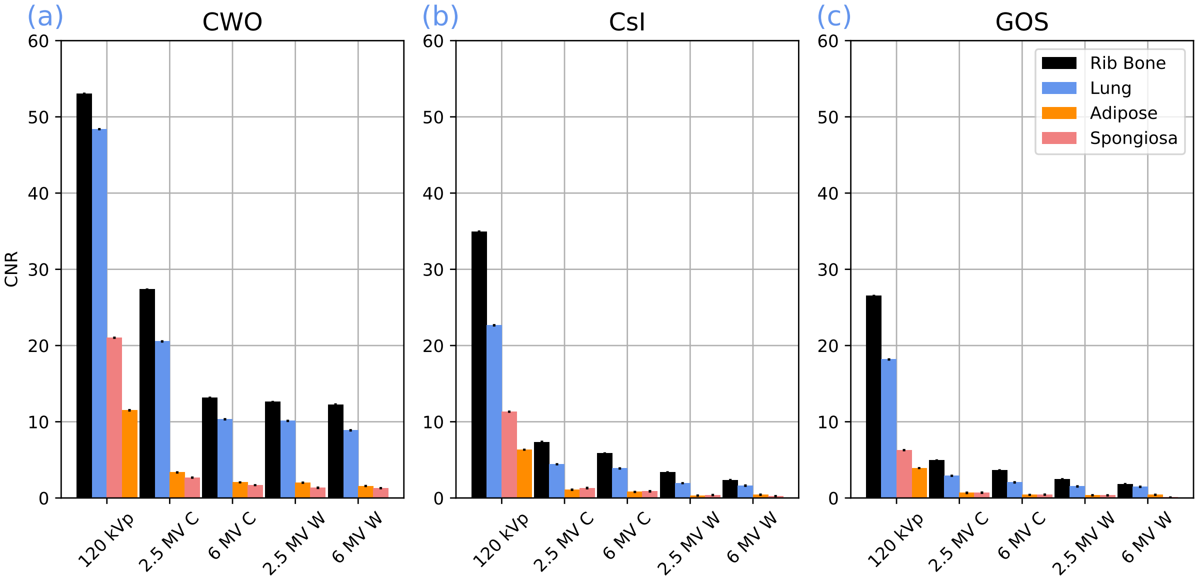

Figure 5.4: The contrast to noise ratio for rib bone, lung, adipose and spongiosa tissues as a function of CWO (a), CsI (b), and GOS (c) detectors for different beam energies and a phantom dose of 7 mGy.

and carbon 2.5 MV beam were 28.1, 20.2, 3.6, and 2.5 for the rib bone, lung, adipose, and spongiosa, respectively. For the CsI and GOS detectors the 120 kVp beam produced the highest CNR over all inserts. The CNRs for the 120 kVp GOS were 27.2, 17.8, 6.6, and 3.4 for the rib bone, lung, adipose, and spongiosa, respectively. The CNRs for the CsI detector and 120 kVp beam were 33.9, 22.2, 6.2, and 11.0 for the rib bone, lung, adipose, and spongiosa, respectively. Finally, the highest-energy 6 MV tungsten target showed the lowest CNR for each detector.

### 5.3.3 Head phantom CBCT imaging

CBCT images of the head phantom with silver amalgam fillings for two beam energies and all three detectors are presented in Figure 5.5. The CBCT images are in agreement with CNR results. Qualitatively, the 120 kVp image shows good contrast as well for both the CWO and CsI detectors (Figure 5.5 a, b). Increased noise becomes prevalent in the images acquired with the CsI and GOS detectors (Figure 5.5 e, c, f). Streaking artifacts are most prevalent in the 120 kVp images, obscuring much of the soft tissue. Likewise, the 2.5 MV images with CsI and GOS detectors show increased streaking artifacts as compared to the CWO image which shows the best preservation of tissue contrast in the soft tissue surrounding the inserts.

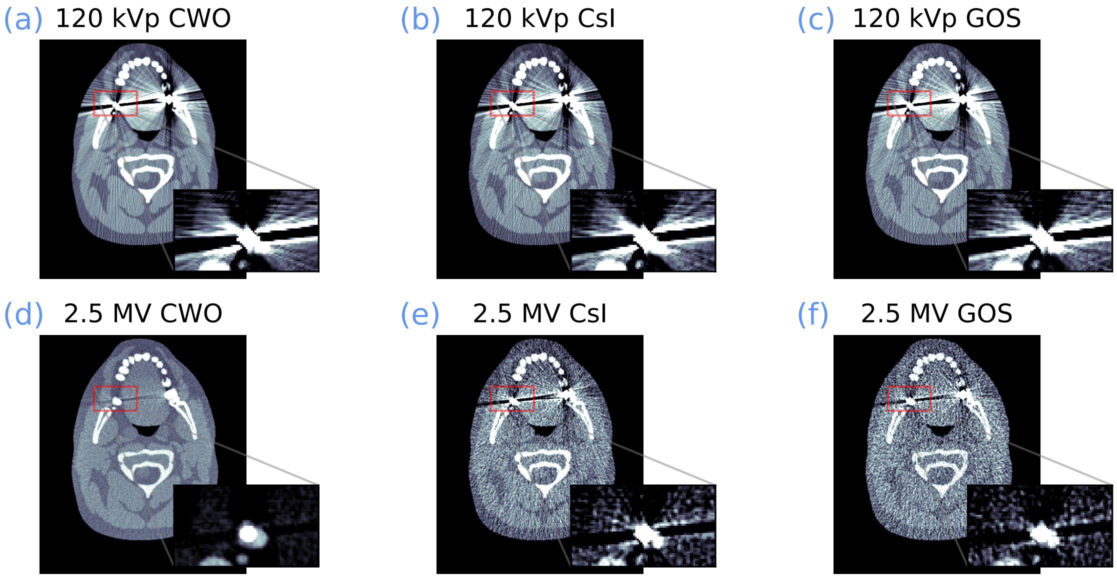

Figure 5.5: Simulated CBCT images of an XCAT head phantom with silver amalgam fillings reconstructed with the CWO (a,d), CsI (b,e) and GOS (c,f) detectors for the 120 kVp (a-c) and 2.5 MV carbon (d-f) beams (W/L 800/0 for images and 1100/450 for inset). All images were reconstructed using the FDK algorithm from 360 views with an imaging dose of 7 mGy.

## 5.4 Discussion

The results of the CNR study presented in Figure 5.4 demonstrate a promising MV beam/detector combination. Undoubtedly, the CWO 120 kVp results in the largest CNRs. However, the CWO CBCT images acquired with the 2.5 MV beam resulted in CNRs comparable to the 120 kVp beam with a CsI or GOS detector. Additionally, this combination shows promise in suppressing metal artifacts, as seen in Figure 5.5. This improvement is in part due to the increased dose efficiency at higher energies, as well as the high absorption efficiency of the CWO relative to the GOS and CsI at MV energies. If high contrast images could be acquired using an EPID, linear accelerator design could be streamlined in some cases by removing the OBI, which would in turn result in reduced linear accelerator costs.

Conversely there are some downsides to this combination. The MTF for the CWO detector with the 2.5 MV carbon target is lower compared to that of the GOS and CsI detectors at all spatial frequencies. The CWO spatial resolution performed differently as a function of beam energy, due to the CWO detector septa. CWO exhibits low attenuation of optical photons at its scintillation energy, resulting in the need for pixel septa to funnel the photons towards the amorphous silicon readout. These septa resulted in a very good MTF at low energies where relatively few interactions in the detector pixel resulted in secondary particles crossing the detector septa and causing scintillation in other pixels. At higher energies the septa were often breached by secondary particles leading to a wider point spread function. However, with the beams discussed, secondary particles did not manage to breach the septa of the adjacent pixels (breaching two septa in total) in large quantities. These metrics can be seen in the optical spread data in fastcat, in which optical spread outside one voxel is not seen in the kV energies but only in MV energies. This led to the two groupings of MTF curves in the CWO detector; a high resolution curve for the 120 kVp beam and the low resolution curve for the rest of the beams. The CWO and GOS detectors showed slowly decreasing MTFs as a function of beam energy with the CsI detector performing slightly better due to its columnar structure. Thus, the CWO detector, at least with the pixel size discussed, shows a disadvantage in terms of spatial resolution as compared to CsI and GOS detectors especially for spatial frequencies above the pixel pitch.

The breach defines detectors with light-blocking septa that enable electron passage. When an electron crosses septa and excites neighboring pixels' photons, CWO's transparency results in isotropic light detection within the pixel. This induces a five-pixels being illuminated in the PSF rather than one, causing a discontinuity in the MTF. In contrast, CsI detectors avert this phenomenon because their micro columnar CsI septa are smaller than the pixel size.

Although both CsI and CWO septal structures induce internal reflection of optical photons, the CsI columnar structure is less efficient in light reflection, allowing a substantial portion of photon fluence to transmit through. Despite this, the micrometer-scale columns lead to cumulative internal reflections, eventually steering photons down a column. This behavior narrows the beam penumbra compared to CWO, which fully reflects light on a millimeter-scale within a pixel. However, due to the millimeter-scale pixel size, light dispersion is more pronounced in the CWO.

Some of the characteristics of real imaging systems were intentionally excluded from simulations in this work. While Fastcat demonstrates the ability to accurately model certain commercial flattening filters for MV imaging and bowtie filters and anti-scatter grids for kV imaging [102], these models were not used in an effort to maintain a fair comparison between beam/detector combinations. The flattening filter was excluded in favour of an idealized uniform beam as the flattening filter is designed for therapy applications and results in cupping artifacts. Likewise, the bowtie filters and anti-scatter grid were excluded in the kV CBCT simulation. We acknowledge that these additional features could led to different results of kV CBCT CNR calculations. These design features will be a topic of future work.

Additionally, the pixel pitch for the detectors was limited to 0.784 mm to model the dimensions of a current CWO detector design [17]. The ability to make smaller pixels of CWO in order to achieve high pixel uniformity is a current limitation of this detector [85]. This limitation is not shared by the GOS and CsI detectors which are commonly produced with smaller pixel sizes defined by their amorphous silicon readout, since they do not require septa. Further, pixel uniformity is generally easily achievable with GOS and CsI detectors, while it is more challenging in CWO detectors. CsI and GOS detectors models examined in this work followed design specifications of existing experimental systems optimized for kV CBCT and MV portal imaging, respectively.

One should note that some of the MTF curves in this publication have been previously validated against experimental beams in previous studies of fastcat [80, 102]. Specifically, the 6 MV MTF curves for the CWO and GOS detectors were compared to experimental results from Star-lack *et al.* and Shi *et al.*, respectively [17, 90]. With MTF values found to have an average root mean squared error (RMSE) of 3.5% and 1.2% compared to experimental values for the CWO and GOS detector respectively. Fastcat's experimental MTF curve was also validated against an experimental beam using the measurements of Howansky *et al.* [116] with results within 4.2% of measurements. In terms of CNR results, kV and MV CNR values were compared between a fastcat simulation of a Catphan CTP404 phantom and an experimental CBCT volume acquired using the OBI and EPID of a Varian Truebeam STx linac.

One question that arises with the use of low-Z target beams is the reduced bremsstrahlung yield compared to high-Z target beams which may affect the length of the image acquisition. There is experimental evidence to suggest that sufficient fluence would be generated, previous studies have shown photon yields from low-Z beams high enough for normal CBCT acquisition at energies above 1.9 MeV [18]. Additionally, there is a trade-off between having a small focal spot size for optimal spatial resolution and acquisition time. Linac focal spot sizes are generally larger than the ones of x-ray tubes. However, on the Truebeam OBI the large kV x-ray tube focal spot size is quoted as 1.0-1.4 mm by 1.4-2.0 mm while the linac electron beam has a focal spot size of approximtely 1.5 mm [121]. This focal spot size could be improved by moving the target higher in the linac head where the electron beam is less divergent or including additional collimation at the target to decrease the focal spot size. However, in previous work by Chan *et al.* MV CBCT system MTF, as determined using the Catphan CTP 528 module, was seen to be worse than that of kV CBCT [122]. Contributing factors to this poor MTF were the decreased contrast of acrylic in the MV range as well as larger focal spots for some MV CBCT setups and the inherent decrease in detector MTF due to the larger MV point spread function as seen in this work.

The demonstration of the increased contrast in the XCAT head phantom CBCT images with the CWO detector and the carbon 2.5 MV beam is compelling as this shows better soft tissue resolution surrounding the silver amalgam fillings compared to the other beam/detector combinations discussed (Figure 5.5d). This demonstrates the possibility of using this beam in some treatment sites for the benefit of metal artifact reduction.

## 5.5 Conclusion

Novel kV/MV CBCT beam/detector combinations were simulated using low-Z beam target spectra and three x-ray detectors. CNR was highest in the CWO detector with a 120 kVp beam. The 2.5 MV carbon target beam combined with a CWO detector showed CNR 4% and 17% lower than current CsI/120 kVp kV imaging systems in lung and bone, respectively and performed best at metal artifact reduction in the XCAT phantom. Whereas, the detector MTF was seen to be highest for a kV beam with the CWO detector at low frequencies, GOS and CsI were seen to outperform CWO in terms of MTF for all MV beams and at high frequencies for the kV beam.

## 5.6 Acknowledgements

This research was enabled in part by support provided by WestGrid (www.westgrid.ca) and Compute Canada Calcul Canada (www.computecanada.ca). The work was partly funded by an NSERC Discovery Grant and the Canada Research Chairs program.

# Chapter 6

# Fastcat Simulations of Perovskite Detectors

**Next generation high resolution perovskite direct conversion detector: Monte Carlo design optimisation and virtual clinical trial**[1]

## 6.1 Introduction

Recent developments in perovskite crystal material chemistry have for the first time introduced a detector material that is simultaneously low-cost, high atomic number, and direct conversion, a combination which could power a next generation of high performing x-ray detectors. These detectors have been demonstrated to have superior spatial resolution to existing detectors, especially at large detector crystal thicknesses [124]: Even though spatial resolution tends to decrease with thickness, a 1200 $\mu$m perovskite crystal detector showed higher modulation transfer function (MTF) than amorphous selenium (a-Se) of any thickness [124].

Additionally, perovskite crystals such as methylammonium lead bromide ($\mathrm{MAPbBr_3}$) have excellent material chemistry when it comes to x-ray detection: The combination of perovskite's high charge carrier mobility ($\mu$) and long carrier lifetimes ($\tau$), as defined by the $\mu\tau$ product, makes them very sensitive to incident x-ray photons [26, 27, 28, 29, 30, 31, 32, 33]. The $\mu\tau$ product of some perovskite crystals is equivalent to that of cadmium zinc telluride (CZT) a promising material that is already being used in cutting edge medical imaging applications [27, 28, 29, 30, 31, 32, 33, 125], while perovskite is simultaneously cheaper and easier to manufacture than CZT [27]. Thus, it is anticipated that this technology could bring in a new generation of flat-panel x-ray detectors.

Analogously, with the introduction of the first generation of direct conversion digital amorphous selenium (a-Se) detectors in the 1990s, a large theoretical and experimental body of work was created to characterise these detectors and their applications [126, 127, 128, 129]. Que *et al.* concluded that geometric distortion from photon incidence at an angle and focal spot were the major contributors to detector MTF. Therefore, as perovskite crystals are produced with large thicknesses it is important to consider the effect of geometric MTF degradation which dominates the spatial resolution of flat

---

[1] This work was published in *Physics in Medicine and Biology* [123]

panel detectors, especially for CT and MV cone beam CT (CBCT) where the higher energy x-rays penetrate deeper in the detector. Additionally, the finite focal spot size for CT modalities limits achievable detective quantum efficiency in flat panels detectors, which is an engineering constraint on the system and cannot be reduced arbitrarily due to heat dissipation requirements in CT. Thus, it is important to discuss the benefit of perovskite detectors while considering these constraints. As a thick high spatial resolution perovskite detector may provide limited benefit over a traditional detector if the system spatial resolution is limited by geometric effects and focal spot blur rather than actual detector spatial resolution.

So, although the high sensitivity and superior spatial resolution of perovskite detectors has been demonstrated in the literature, no quantification has been done on whether these improvements translate to improvements in medical imaging. In this work first we optimise detector thickness based on a combination of theoretical models and Monte Carlo (MC) simulations taking into account degradation of spatial resolution due to geometric factors and device focal spot sizes. Further we perform virtual clinical trials (VCTs) on anthropomorphic phantoms using device specifications from three common CBCT devices to demonstrate the improvement associated with next generation perovskite detectors.

While perovskite can be either a scintillator or a direct conversion detector. In this study we considered it only as a direct conversion device. While scintillation has shown promise in this detector material, currently our lab does not have the ability to fabricate a detector with a microcapillary structure. Thus we thought to simulate the materials that we are able to manufacture such that this work can be translated more readily to experimental applications.

## 6.2 Materials and Methods

### 6.2.1 Energy Deposition Efficiency

To determine the domains of medical imaging for which perovskite crystals are most suited, the energy deposition efficiency of perovskite crystals was compared to other common medical imaging materials for a wide range of photon energies used in medical imaging. Energy deposition efficiency (EDE), $\eta_e$, is a measure of the fraction of the energy absorbed in the detector relative to the energy incident on the detector and is a robust measure of the potential efficiency of a detector. At an energy $e$, $\eta_e$, is defined in terms of ratio of the incident energy $E_{e,i}$ on the detector to the energy absorbed in the detector crystal $E_{e,abs}$ from a mono-energetic pencil beam at energy $e$ impinging normally to the detector

$$\eta_e = \frac{E_{e,abs}}{E_{e,i}}. \tag{6.1}$$

Simulations of detector energy deposition efficiency were performed in TOPAS [69] with $10^7$ initial particles per energy per crystal thickness. The mono-energetic pencil beam energies used were 10 to 90 keV in 10 keV increments, 100 to 900 keV in 100 keV increments, and 1, 2, 4, and 6 MeV. A greater emphasis of energies in the low energy range was used to help resolve photo-electric behaviour near the K-edges of the detector constituent elements. Detector thicknesses of 0.029, 0.1, 0.2, 0.3, 0.5, 1, 2, 5, 10, and 15 mm were considered. A global particle range cutoff of 0.001 mm was used to remain much smaller than the minimum studied crystal thickness of 0.029 mm. Simulations were run on a linux desktop computer on eight 4.0 GHz Intel Skylake cores with compute times on the order of 30 minutes.This aforementioned desktop environment and particle cutoff were used in all simulations in this work if not specified.

### 6.2.2 Detector Materials

Energy deposition efficiency was calculated for three common detector materials; amorphous selenium (a-Se), caesium iodide (CsI), and gadolinium oxysulphide (GOS). a-Se is a common material used for mammography and lower energy imaging application, columnar CsI is standard detector material for kV CT imaging, and GOS is a low cost material commonly used in kV and MV imaging systems. Additionally, cadmium zinc-telluride (CZT) detector was modelled, although not as commonly used, CZT is a promising high atomic number direct conversion material that has properties similar to perovskite halides and is used for photon-counting CT imaging.

The detectors used in the EDE comparison were modelled based on material specifications of existing detectors. As such, the density of the Cu-GOS detector is the density of the phosphor and binder glue of a Varian aS1200 detector, while the CsI detector's density is the average density of a PaxScan 4030CB with a 70% fill ratio. The CZT detector is based on material compositions from Redlen (Redlen Technologies, Saanichton, BC, Canada) [125, 130]. Additional material information is shown in table 6.1 and table 6.2. All detectors were modelled with a pixel pitch of 100 $\mu$m.

Table 6.1: Detector Parameters

| Material | Chemical Formula | Density [g/cm$^3$] | Direct Conversion | Columnar | K-edges [keV] | $\mu$ 40 keV [cm$^{-1}$] | $\mu$ 100 keV [cm$^{-1}$] | $\mu$ 1 MeV [cm$^{-1}$] |
|---|---|---|---|---|---|---|---|---|
| Perovskite | $MAPbBr_3$ | 3.83 | Yes/No | No | 13.5 (Br)<br>88.0 (Pb) | 29.9 | 9.87 | 0.29 |
| Cu-GOS | $Gd_2O_2S$:Tb | 4.59 | No | No | 50.2 (Gd)<br>52.0 (Tb) | 16.2 | 7.30 | 0.25 |
| CsI | CsI:Tl | 3.16 | No | Yes | 36.0 (Cs)<br>85.5 (Tl) | 72.5 | 6.42 | 0.18 |
| aSe | Se | 4.26 | Yes | No | 12.7 (Se) | 32.3 | 2.80 | 0.25 |
| CZT | CdZnTe | 5.8 | Yes | No | 26.7 (Cd)<br>31.8 (Te) | 104 | 9.05 | 0.33 |

### 6.2.3 Virtual Clinical Trials

Three VCTs were conducted in this work to demonstrate perovskite's application in different imaging areas: 1) the Koning dedicated breast CT (BCT) (KBCT 1000, Koning Corporation, West Henrietta, NY, USA), 2) the Varian Truebeam Stx (Varian Medical Systems, Palo Alto, CA) kV on board imager (OBI), and 3) the Truebeam electronic portal imager (EPID) for MV CBCT. A description of the device specifications used in the simulations can be found in table 6.2 and a schematic of the setup in figure 6.1.

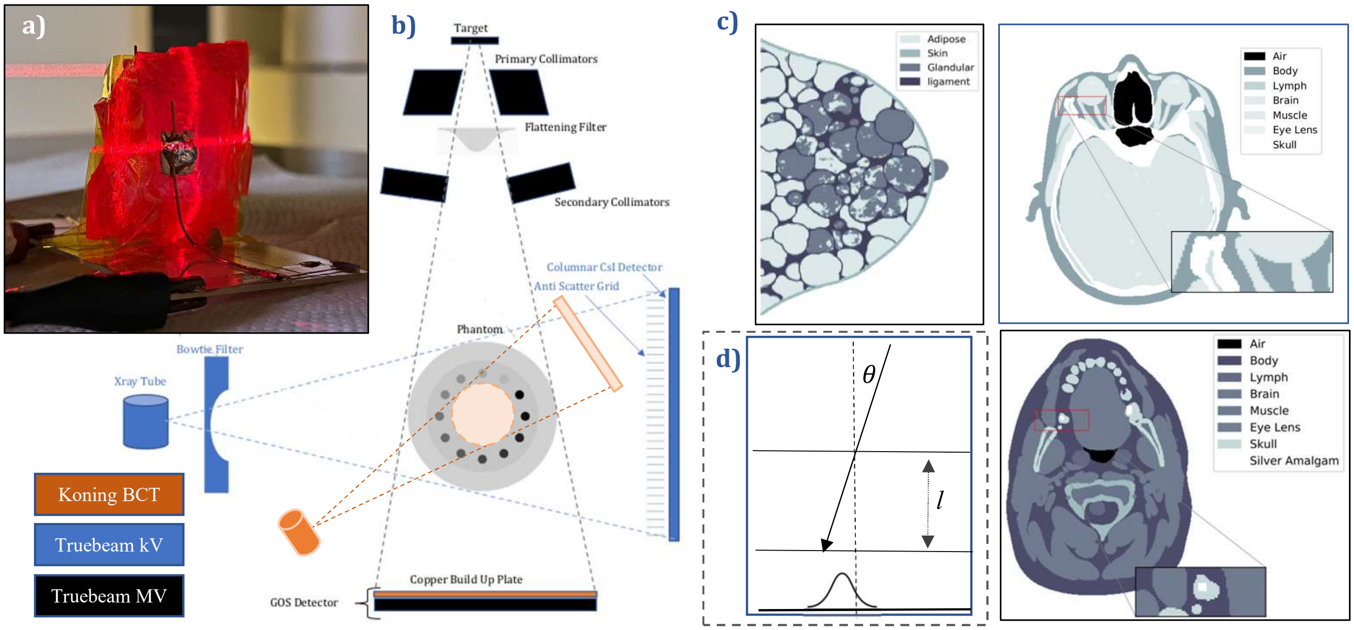

Figure 6.1: a) An image of a thick perovskite crystal grown in our laboratory b) Schematic of the Fastcat simulation setups for the three VCTs. c) Images of the three phantoms used in the VCTs d) Schematic showing an oblique incidence x-ray hitting a detector of thickness $l$ at an angle $\theta$ with a gaussian curve representing the resultant point spread function (PSF).

The kV detector on the Truebeam OBI was modelled with an anti-scatter grid, for details on the anti-scatter grid see the more in depth validation of the fastcat model in Chapter 4. The Koning BCT did not feature an anti-scatter grid as it is not specified in the design parameters.

### 6.2.4 Modulation Transfer Function

The MTFs in this study were first calculated using Fastcat and degraded based on the extensive theoretical work of Que and Rowlands [126] who developed a rigorous framework for MTF degradation. Fastcat weights mono-energetic point spread functions calculated using Topas MC to analytically calculate MTFs for polyenergetic beams. Fastcat's full MTF methodology and experimental validation of the MTF calculations can be found in our previous work [102]. According to Que and Rowlands,

Table 6.2: VCT Parameters

| Imaging Machine | SAD - SID [mm] | Incidence Angle [°] | Detector - crystal thickness | Beam kVp [kV] | Beam Filtration | Focal Spot nominal [mm] |
|---|---|---|---|---|---|---|
| Koning BCT | 422 - 778 | 7.24 | PaxScan 4030CB (CsI:Tl) - 0.6mm | 49 | 0.8 mm Be,<br>1.58 mm Al | 0.3 |
| Varian kV CBCT | 1000 - 1500 | 6 | PaxScan 4030CB (CsI:Tl) - 0.6mm | 100 | 3 mm Al,<br>0.89 mm Ti | 1.0 |
| Varian MV CBCT | 1000 - 1500 | 6 | aS1200 (Cu-GOS) - 0.29 mm | 6000 | N/A | 1.5 [121] |

geometrical distortion is often the largest contributor to MTF degradation. This is especially true for thick detectors and higher energies where the photons and secondary electrons may travel to large depths in the detector crystals. Geometric MTF distortion can be described using the following equation:

$$MTF_g(\nu) = \frac{\{[1-L]^2 + 4L\sin^2(\pi\nu l\tan\theta))\}^{1/2}}{[1-L][1+(2\pi\nu\sin\theta/\mu)^2]^{1/2}}, \tag{6.2}$$

where

$$L = \exp\left(-\mu l/\cos\theta\right) \tag{6.3}$$

and $\mu$ is the attenuation coefficient of the detector material at a given energy. In the case of a polyenergetic beam the attenuation was weighted by the fluence, detector EDE, and energy. The weighting by the detector EDE and energy was necessary as these factors influence the readout intensity of an energy integrating detector. $l$ is the thickness of the detector while $\theta$ is the angle of the incidence of the photons. Finally, $\nu$ is the spatial frequency of the MTF. A schematic of geometric distortion can be seen in figure 6.1d).

For the flat panel detectors discussed, the photon incidence angle, $\theta$, was approximated to be the mean angle of incidence for a typical acquisition. A value of 7.24° was calculated as the mean angle of incidence for the BCT. In kV- and MV-CBCT the average angle of incidence was estimated to be 6°, corresponding to half the angle of the detector collimation of 12°.

The second contributor to MTF degradation discussed is the focal spot of the x-ray tube. It is defined as the full width at half maximum (FWHM) of the source intensity on the x-ray tube target surface. The focal spots of the machines were approximated as Gaussian point spread functions (PSF). Taking the Fourier transform of a Gaussian we obtain the focal spot MTF ($MTF_{fs}$) which is also a Gaussian of the form:

$$MTF_{fs}(\nu) = \exp\left(-\pi^2\nu^2s^2\right) \tag{6.4}$$

where $s$ is the inverse of the standard deviation of the point spread function and $\nu$ is the spatial frequency.

Nominal focal spots as defined by the IEC 60336:2005 standard are stated in table 6.3. According to the standard, the full width 15% max is used as the measure of the focal spot. The nominal focal spot sizes are not exact and have associated permissible dimensions according to the IEC standard. The average of the width and length of the focal spot is averaged and approximated by a gaussian of that dimension. Based on this gaussian, one can calculate a value for the standard deviation s. For the Koning BCT 0.3 nominal focal spot value the permissible dimensions are a width of 0.45 mm and a length of 0.65 mm and for the Truebeam kV-OBI the 1.0 nominal focal spot value the permissible dimensions are a width of 1.4 mm and a length of 2.0 mm. For the Truebeam the MV beam the dimensions relate directly to the FWHM [121]. Using a gaussian distribution these measurements

Table 6.3: Focal Spot Parameters

| Machine | IEC Nominal Focal Spot | IEC Focal Spot Dimensions [mm] | FWHM [mm] | Scaling | s [mm] |
|---|---|---|---|---|---|
| Koning BCT | 0.3 mm | 0.45×0.6 | 0.3321 | 0.81 | 0.114 |
| Varian kV CBCT | 1 mm | 1.4×2.0 | 1.027 | 0.5 | 0.218 |
| Varian MV CBCT | N/A | N/A | 1.5 | 0.5 | 0.340 |

are related to the standard deviation s: A full width at 15% max is 3.894s and the FWHM is 2.355s. These values are then multiplied by the scaling factor, which is the ratio of the source-imager distance (SID) minus the source-axis distance (SAD) divided by the SAD.

The partial MTFs, which are Fourier transforms of spatial convolutions, are then multiplied in the frequency domain to generate a final MTF resultant from the original MTFs degraded by focal spot and geometric distortions.

### 6.2.5 Noise Power Spectrum

The noise power spectrum (NPS) for each of the detector crystal thicknesses was calculated using MC techniques with the Fastcat hybrid MC code [80, 102]. For each photon beam and detector thickness, a flat-field image was simulated in compliance with the IEC-defined normal exposure. The detector was irradiated with an approximate exposure of $1\times10^{-7}$ C/kg and a 128×128 pixel area of the detector was used for calculation of the NPS. The NPS analysis component was the IEC RQA5 method as described by Dobbins *et al.* [60]. The NPS is defined as the Fourier amplitude of a two dimensional image with intensity $I$ as

$$NPS(\mu_n, \nu_k) = \lim_{N_x, N_y \to \infty} (N_x N_y \Delta x \Delta y) |\mathcal{F}_{n,k}[I(x,y) - \bar{I}]|^2 \tag{6.5}$$

Where $I(x, y)$ is the image intensity at the pixel location $(x, y)$, $\mathcal{F}_{n,k}$ is the two dimensional Fourier transform where $n$ and $k$ are indices for the specific spatial frequency being sampled, $\bar{I}$ is the mean intensity of the image, $\nu$ and $\mu$ are the spatial frequencies conjugate to $x$ and $y$, while $\Delta x$ and $\Delta y$ are the pixel pitch of the detector and $N_x$, $N_y$ are the number of pixels in the $x$ and $y$ direction, respectively. Two dimensional NPS was calculated using the IEC 62220-1 method; a 640×640 pixel area of the detector was evaluated with 256×256 overlapping regions of interest (ROIs). Second order detrending was used as a background subtraction method and seven central rows of the two dimensional NPS above and below the x-axis were combined to produce a one dimensional NPS.

### 6.2.6 Detective quantum efficiency

The detective quantum efficiency (DQE) of a detector is a metric that measures the degradation of the information contained in an output signal relative to the original input signal. Since detectors have physical limitations determined by Poisson statistics and finite pixel size, the DQE is measured relative to the ideal detector which is only limited by these factors. The work of Ranger *et al.* was followed to calculate the DQE [59]. Formally DQE is calculated as:

$$DQE(\nu) = S^2 \frac{MTF^2(\nu)}{NPS(\nu) \times q \times E} = \frac{MTF^2(\nu)}{NNPS(\nu) \times q \times E} \tag{6.6}$$

Where $MTF(\nu)$ is the frequency-dependent $MTF$, $NPS(\nu)$ is the frequency-dependent noise power spectrum ($NPS$), $S$ is the square of the large-area signal intensity. This equation can be simplified by using the $NNPS$ which is the noise power spectrum divided by the large-are signal intensity squared. Meanwhile, the $q$ value is an estimate of the number of incident x-ray photons per unit area per unit of exposure incident on the detector generally estimated through computer modelling. Finally, $E$ is the IEC-defined normal exposure. $q$ values and normal exposures were not calculated in this work since they were constant as a function of detector crystal thicknesses, making them unimportant in the context of a detector thickness optimization. Thus as measure denoted the relative DQE ($DQE_r$) was used

$$DQE_r(\nu) = \frac{MTF^2(\nu)}{NNPS(\nu)}. \tag{6.7}$$

### 6.2.7 Imaging beams

Each imaging task was simulated with an appropriate x-ray beam. The BCT spectra was modelled after 40 kVp beam with 0.8 mm of beryllium filtration and 2 mm aluminum filtration. The kV CBCT 100 kVp beam was modelled with 3 mm inherent aluminum filtration and a 0.89-mm thick titanium beam hardening filter. The x-ray beam spectra were simulated in Fastcat by means of xpecgen [87]. In addition, a 6 MV photon energy spectra was calculated from the Truebeam MV phasespace file provided by Varian and available online through the IAEA NDS [131].

### 6.2.8 Phantoms

VCTs for each of the three imaging systems were conducted using appropriate phantoms depicted in figure 6.1c) with parameters in table 6.4. BCT images of an anthropomorphic breast phantom with microcalcifications [76] were simulated for the Koning BCT setup. The breast phantom was composed of adipose tissue, skin, and glandular tissue, with the microcalcification composed of cortical bone. Material elemental compositions were defined using the values defined in the Geant4 default materials [44] and ICRU 44 [98]. The kV and MV CBCT VCTs featured an XCAT [75] head phantom. The kV image demonstrated the image quality in the brain while the MV image focused on a region in the skull with silver amalgam fillings that would generate streaking artifacts in kV images.

Table 6.4: Phantom parameters

| Phantom | # of pixels [x,y,z] | Dimensions [x,y,z] [mm$^3$] |
|---|---|---|
| BCT | 512,512,156 | 205, 205, 125 |
| kV CBCT (XCAT) | 1024,1024,256 | 512, 512, 31.25 |
| MV CBCT (XCAT) | 1024,1024,256 | 512, 512, 31.25 |

A distinct catphan simulation was conducted for specific materials like the lung to ensure statistical adequacy. The CNR was computed using bootstrapping: A larger ROI encompassing water and one encompassing the target material was chosen, with half the points in each ROI sampled to calculate a CNR. This procedure was iterated 100 times to establish a CNR distribution, with the displayed values representing the mean and error bars indicating the 90% confidence interval.

### 6.2.9 Image generation and reconstruction

Virtual clinical trial CBCTs were simulated using the Fastcat hybrid Monte Carlo code. Fastcat uses an angularly independent scatter approximation to speed up the CBCT image simulations in rotationally symmetric objects. Fastcat simulations consider the physics processes described by the Topas Penelope physics module as well as the Topas optical module for simulating light transport in scintillators. Fastcat simulations closely agree with experimental MTF and NPS measurements on a Truebeam linac for both the Cu-GOS electronic portal imager (EPID) and CsI on-board imager (OBI) [102]. Fastcat's full MTF methodology and experimental validation of the MTF calculations can be found in O'Connell and Bazalova's previous work [102, 80]. MTF values for the Paxscan CB4030 and aS1200 detectors agreed within 4.2% and 2.5% of experimental measurements, respectively. All phantom parameters as specified in Fastcat are summarized in table 6.2 and 6.4. To generate CBCT images, views were acquired at 300, 887, and 493 equally spaced angles between 0° and 360° for the BCT, kV- and MV-CBCT acquisitions, respectively. Images were reconstructed using the FDK algorithm [96] with a Ram-Lak filter. All scans were simulated to have noise consistent with a 7 mGy mean dose to the phantom. Doses were calculated in Fastcat. CBCT image simulations took, on average, 64 to 87 seconds on a Nvidia GeForce RTX 2070 GPU (Nvidia Corp., Santa Clara, CA).

CBCT image contrast to noise ratio (CNR) was compared between perovskite and the default detector using the same ROIs in each image. Contrast was measured against adipose tissue in reconstructions of the breast phantom and muscle in reconstructions of the head phantom. We denote the average HU value from this region $\mu_{body}$ and the value from the insert $\mu_{ROI}$. CNR was measured relative to the same region using the standard deviations $\sigma_{ROI}$ and $\sigma_{body}$ as

$$CNR = \frac{\mu_{ROI} - \mu_{body}}{\sqrt{\sigma^2_{body} + \sigma^2_{ROI}}} \tag{6.8}$$

CNR was bootstrapped to generate a 99% confidence interval.

## 6.3 Results

### 6.3.1 Energy deposition efficiency

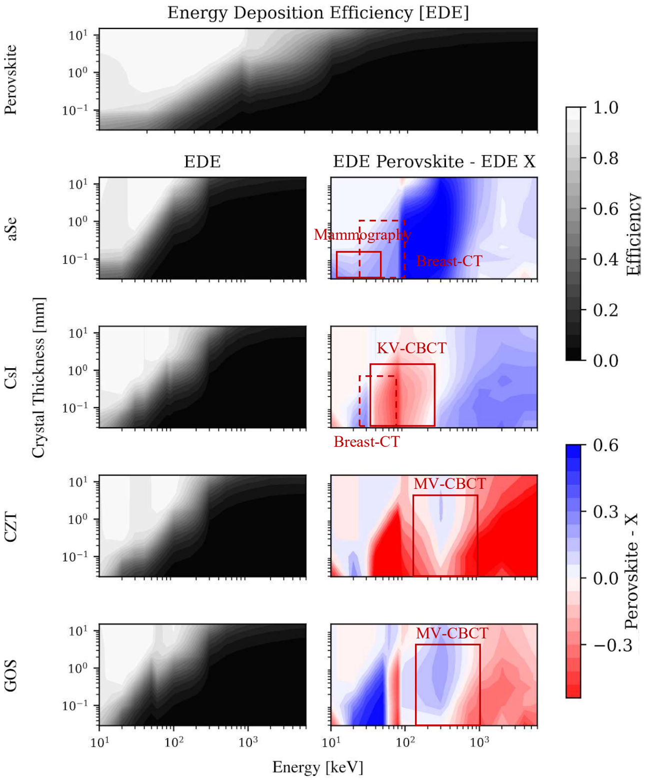

Figure 6.2: Plots of the EDE as a function of crystal thickness and photon energy for each detector material are shown, logarithmic interpolation was used to generate the surfaces shown in this figure from the discrete energies and thicknesses listed in section 2.1. In the right column the EDE of perovskite is compared to the other detectors, blue regions indicating superior EDE for perovskite while red regions indicate regions where perovskite performs poorer as compared to the existing detector.

The energy deposition efficiency (EDE) as a function of beam energy and detector thickness for both the perovskite $MAPbBr_3$ material and a variety of other materials is presented in figure 6.2. The perovskite EDE is also compared individually to current detector materials. The perovskite material's high atomic number lead allows for greater EDE than a-Se at all energies and thicknesses, with a greater than 60% increase generally above the K-edge of lead and a 20-30% efficiency increase for low thickness detectors at low energies. As compared to CsI, perovskite EDE is increased for mammography energies below the K-edges of caesium at 36 keV and iodine at 33 keV while CsI has 20-30% better EDE in the 30-80 keV range, with 10-20% better efficiency above the K-edges of thallium and lead at 85 and 88 keV, respectively. CZT has generally higher EDE than perovskite save in the mammography range below the K-edge of cadmium at 27 keV. GOS is a worse energy absorber than perovskite for energies below the K-edge of gadolinium at 50 keV. Additionally, perovskite is a better energy absorber in the range above the lead K-edge of 88 keV to approximately 1 MeV, which corresponds to the high fluence of an MV x-ray spectrum.

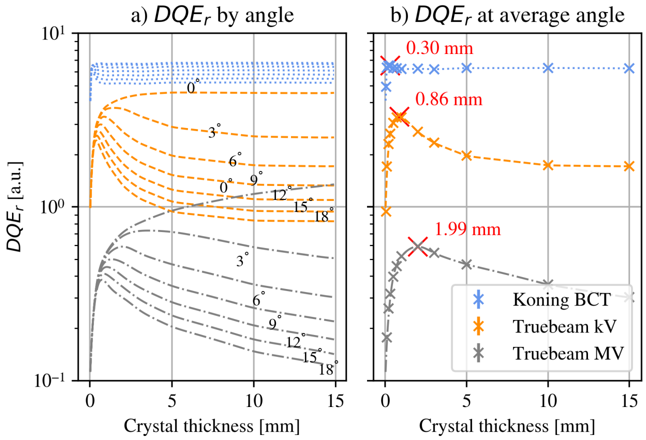

Figure 6.3: The relative DQE results. a) Relative DQE averaged over frequencies up to the Nyquist frequency of 5 lp/mm for a detector pixel pitch of 100 µm was simulated for the different experimental setups at a variety of photon incidence angles as a function of detector thickness. b) The DQE for each of the experimental setups using the average angle of incidence is shown, the thickness of the maximum relative DQE is shown in red.

### 6.3.2 Detective quantum efficiency

The DQE as a function of crystal thickness and beam angle of incidence are shown in figure 6.3 a). As expected according to the work of Que *et al.* the DQE as a function of thickness was much more affected by angle at higher energies due to geometric MTF degradation [126]. For the 40 kVp beam used for the BCT the detector, DQE decreased by less than 5% after the peak DQE but decreased by a factor of 5 for the MV CBCT at 15 mm thicknesses and an 18 degree angle of incidence. For the specific machine setups studied (figure 6.3 b)), the optimal DQE thickness for the Koning BCT, and Truebeam MV and kV CBCT were 0.30, 0.86, and 1.99 mm, respectively. These thicknesses resulted in improvements in the $DQE_r$ seen in figure 6.4.

$DQE_r$ was calculated for each of the three imaging systems using the parameters described in

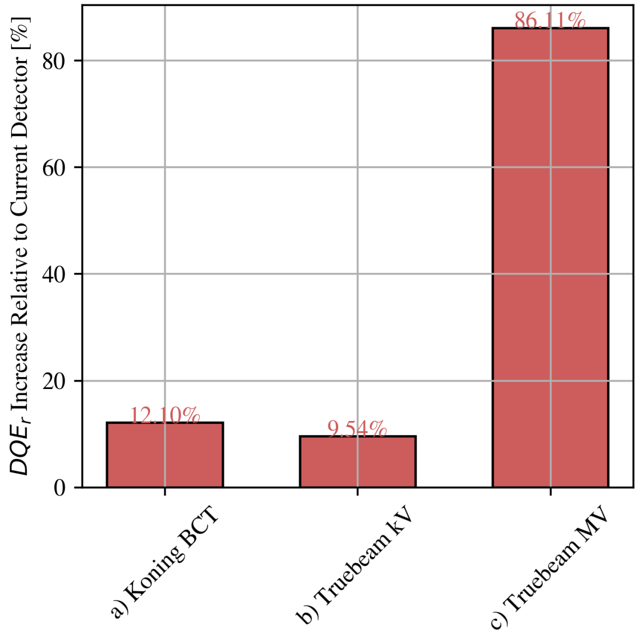

Figure 6.4: The DQE of the optimal perovskite thickness relative to the default detector for the three experimental setups.

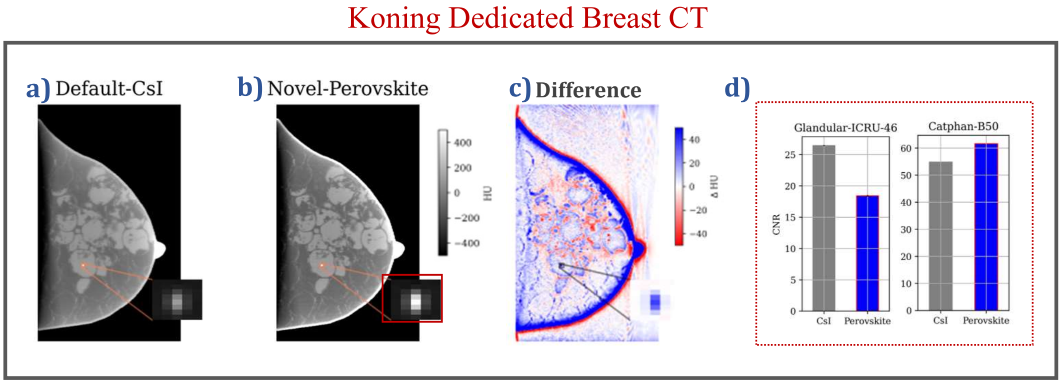

Figure 6.5: The results of the Koning BCT VCT are shown. a-b) Images of the anthropomorphic breast phantom using CsI and Perovskite detectors with a microcalcification in the inlay. c) The difference between CsI and Perovskite CBCTs, blue areas indicating regions where Perovskite has higher HU values. d) CNR of key breast tissues for both detectors is plotted.

tables 1 and 2 for detector thicknesses of 0.029, 0.1, 0.2, 0.3, 0.5, 1, 2, 5, 10, and 15 mm. $DQE_r$ was then interpolated using radial basis function interpolation to find the crystal thickness corresponding to the maximum $DQE_r$.

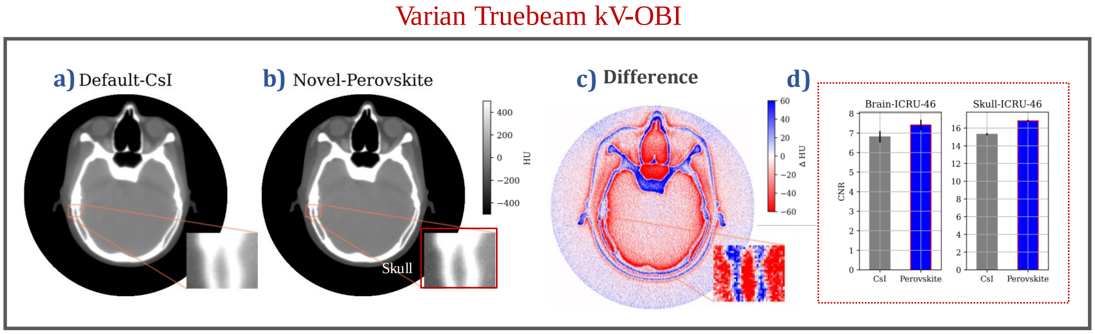

Figure 6.6: The results of the Truebeam kV-CBCT VCT are shown. a-b) Images of the XCAT phantom's brain region using CsI and perovskite detectors, respectively, with fine bone features in the inlay. c) The difference between CsI and perovskite CBCTs, blue areas indicating regions where perovskite has higher HU values. d) CNR of key head tissues for both CBCTs are plotted.

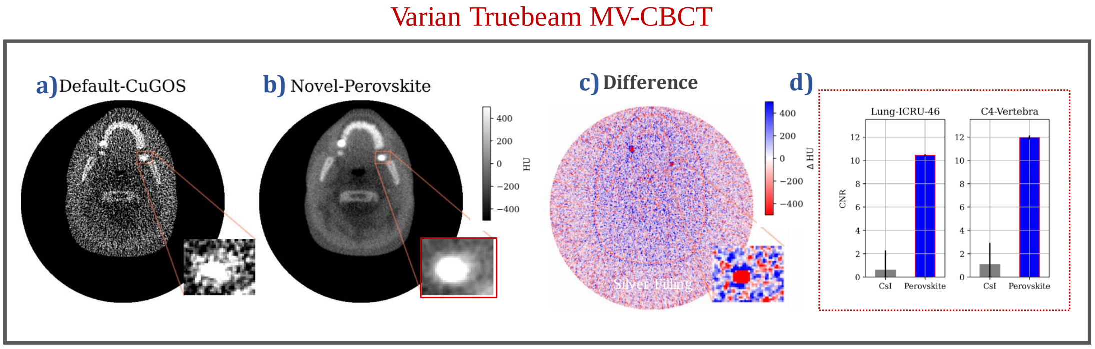

Figure 6.7: The results of the Varian MV-CBCT VCT are shown. a-b) Images of the XCAT phantom's mandible region using GOS and Perovskite detectors, respectively, with silver amalgam fillings in the inlay. c) The difference between GOS and Perovskite CBCTs, blue areas indicating regions where Perovskite has higher HU values. d) CNR of key head tissues for both CBCTs are plotted.

### 6.3.3 Virtual Clinical Trial

#### Koning Breast CT

In figure 6.5 MC-simulated BCT images of the anthropomorphic breast phantom acquired with the default CsI detector (0.30 mm thick, 0.194 mm pixel pitch) and a perovskite detector (0.8 mm thick 0.194 mm pixel pitch) are shown. The perovskite detector resulted in a 87% increase in contrast in the microcalcification of the breast phantom. The contrast to noise ratio (CNR) in inserts of glandular tissue and bone based showed a 28% decrease and 9.8% increase in CNR, respectively, demonstrating an improvement in microcalcification detection and DQE using the novel perovskite detector which can be manufactured at lower cost than CsI.

### Truebeam kV- and MV-CBCT

VCTs of Varian Truebeam kV- (6.6) and MV-CBCT (6.7) images for 0.336 mm pixel pitch, 0.6 mm thick CsI and 0.29 mm thick Cu-GOS detectors and 0.86 mm and 1.99 mm thick 0.336 mm pixel pitch perovskite detectors, respectively, show dramatic image quality improvement for the perovskite detector in the XCAT head phantom. As shown in figure 6.6 a-b), kV-CBCT spatial resolution in fine bone features and tissue contrast was improved dramatically using the perovskite direct conversion detector. At the same time, perovskite detector CNR in brain and skull was increased by 8% and 13%, respectively, as compared to the default CsI detector. In figure 6.7 the high efficiency of the perovskite detector as compared to the Cu-GOS MV-CBCT resulted in dramatic improvement of CNR in the XCAT head phantom with silver fillings in two molars. CNR in lung and C4-vertebra tissues which are commonly imaged when positioning a patient were improved from 0.8 and 1.1 to 10.3 and 12.0, respectively.

## 6.4 Discussion

In the VCTs, perovskite detectors showed great potential to ameliorate existing CBCT devices. We show improvements to CNR in a number of tissues. In figure 6.5, a breast calcified lesion that is poorly defined using a CsI detector, while the increased spatial resolution and CNR of the perovskite detector led to differentiation of the lesion from the surrounding tissue. This differentiation could lead to more accurate identification of such anatomical structures in breast cancer screening. Additionally, there was a 9.8% improvement in bone CNR for the perovskite detector, however, there was also a decrease in the contrast to noise ratio in glandular tissue. This was likely due to a combination of the higher spatial resolution and the thinner detector increasing the spatial resolution at the cost of increased noise as is the general trade-off. To increase the CNR in glandular tissue we recommend that the detector be made thicker than the 0.3 mm which results in the optimal DQE, for example up to a 1.1 mm detector would greatly increase CNR and reduce DQE by less than 2%. Likewise, the improved contrast in the MV-CBCT when perovskite detector is used shows a metal artifact free image of a human jaw with dental amalgam, an imaging case in which kV-CBCT generally produces large streaking artifacts covering clinically relevant anatomical features. Additionally, the MV-CBCT contrast increase for the perovskite detector relative to the default GOS detector could lead to possible imaging of patients on machines lacking a kV-OBI which is the case for most machines in low- and middle-income countries.

The EDE results yielded better performance for perovskite than all other detectors tested in the mammography range of energies (10-40 keV) and only CZT had superior EDE in the MV imaging energy range (0.5-1.5 MeV). In this work we estimate EDE to be a proxy for DQE(0) or the base absorption of the detector, assuming that the detectors have similar conversion efficiency between energy absorbed and readout signal intensity. We assume this equivalence for simplicity as the electron hole transport inside direct conversion detectors cannot be simulated easily in MC particle transport software. The presence of lead in the perovskite material resulted in the highest energy absorption in the mammography energy range. In the kV energy range, perovskite generally did not perform as well as other detector materials due to low EDE below the lead K-edge at 88 keV and poorer Compton absorption due to its relatively low density compared to the other detector materials. In the 0.5 to 1.5 MeV range which contains the majority of photons for MV imaging, the photo-electric attenuation of lead, due to its high atomic number led to greater EDE than all detectors save CZT.

One disadvantage of $MAPbBr_3$ perovskite crystals is the lower density as compared to CZT, GOS, and a-Se, as can be seen in table 1. When considering the degradation to spatial resolution incurred due to the detector thickness, a higher density detector is advantageous as photons are attenuated more quickly in high density materials. The effect of the lower density would not be seen for mammography and breast CT applications as the x-rays do not travel far in the crystal due to the high photo-electric attenuation. However, for higher energy kV and MV beams, the more penetrating beams create geometric MTF degradation. For these cases higher density $MAPbI_3$ crystals would be advantageous and we estimate these crystals would be equivalent to CZT in terms of EDE in kV and MV applications, however it is yet to be seen if these crystals can be grown to the same thicknesses as $MAPbBr_3$ which we can grow to thicknesses of 15 mm in our lab. Another problem encountered with perovskites is that the lead containing crystals provide risk of toxicity if not encapsulated properly.

Care was taken to model detector physics in this work, however, there remain certain relevant detector parameters that were not feasible to model in this study. Without a pixelated perovskite detector we were unable to characterise the electronic noise and conversion efficiency in the detector and compare it to that of currently available detectors. Additionally, we did not include optimization of the current GOS and CsI detectors in this manuscript. This was partially based on the assumption that the crystal thickness was already optimised for their applications by the device manufacturer. Our goal was to compare this novel perovskite technology to existing detectors used in a clinical setting rather than to hypothetical devices. This does leave the possibility that there exist optimizations possible for CsI and GOS detectors to achieve similar $DQE_r$ values given additional optimization.

Replacing the traditional GOS EPID with a novel-perovskite detector resulted in an improvement in $DQE_r$ of 86.11%. This large improvement is due to a number of factors: GOS absorbs its own photon emissions, a property that limits the thickness of the GOS crystal. Likewise, GOS is a turbid phosphor, necessitating thin crystals to produce sharp images. The optimal GOS crystal thickness for the TrueBeam EPID scintillator is therefore a relatively thin 0.29 mm. Conversely, GOS is a convenient EPID material due to its radiation hardness that can withstand the therapeutic doses delivered routinely during linac quality assurance. It remains to be seen whether perovskite materials can provide sufficient radiation hardness for this application.

To allow for efficient optimization of crystal thickness, $DQE_r$ was used as an optimization metric.

While the use of a summary statistic such as $DQE_r$ does not take into account the spatial information of the DQE, $DQE_r$ is less noisy and contains more information than common metrics such as $DQE_{10}$ or $DQE_{50}$. An obvious limitation of the $DQE_r$ is that DQE at some spatial frequencies may be more important than others in some applications. For example, in breast microcalcification detection, high frequency DQE could be prioritised over low frequency DQE.

While detectors with pixel sizes less than 100 $\mu$m are used in medical imaging applications, the pixel size of the detectors discussed in this work was limited to 100 $\mu$m, as pixel pitch of less than 100 $\mu$m is uncommon in the CBCT applications discussed. In the case of the TrueBeam OBI, even the 194 $\mu$m pixels are regularly 2×2 binned to 388 $\mu$m during CBCT acquisition to decrease detector noise and speed up image reconstruction algorithms. From a manufacturing point of view, direct conversion detectors like perovskite materials can be manufactured with smaller pixel pitches than indirect conversion detectors and their application in fields like mammography will be a topic of future work.

A constraint on perovskite crystal thickness due geometric MTF degradation was introduced in this work. Specifically, in kV imaging, we find optimal detector thickness for perovskite to be 0.86 mm which is only slightly thicker than the 0.6 mm thickness often seen in CsI detectors. Perovskite detector's ability to produces high spatial resolution at large crystal thicknesses has a substantial 12.1% benefits to DQE over conventional detectors in Koning BCT and a 9.5% benefit to DQE in Truebeam kV-CBCT. Perovskite also provides greatly increased DQE in MV-CBCT imaging with a 87% increase over a GOS detector on a Truebeam machine. This could enable MV-CBCT to be used more routinely in clinical settings. Additionally, to truly maximise the benefit of thick perovskite detectors, applications such as PET imaging and CT imaging could be targeted; as the detector elements form a focused arc around the source reducing the distortion from geometric MTF degradation. Likewise, variable thickness in the detector or piece-wise focusing of the detector elements as in the work of Star-Lack *et al.* [17] could result in optimised DQE especially in MV imaging. Since the focal spot MTF degradation also effects the achievable DQE for these detectors, we also see potential for smaller focal spot x-ray tubes to be effective in increasing DQE even more than demonstrated here when used in combination with perovskite detectors especially for BCT.

## 6.5 Conclusion

Overall, perovskite-based x-ray detectors have high absorption efficiency and great spatial resolution at low production costs. Here we demonstrate device-specific systematic detector optimisation combined with a state-of-the-art VCT to present the impact of this technology in common medical x-ray imaging devices. We conclude that perovskite detectors perform better than current detectors in breast-CT and kV-CBCT applications, and are far superior to current MV-CBCT detectors in terms of contrast to noise ratio and detective quantum efficiency. Future work aims implemented a prototype perovskite flat-panel detector on these specific devices for experimental verification of these VCT.

# Chapter 7

# SITKA: kV Isocentric Treatment Device

### Lung SABR treatments delivered with a gantry-mounted x-ray tube[1]

## 7.1 Introduction

Radiotherapy (RT) research often focuses on state-of-the-art methods to provide small improvements in the treatment of cancer patients in high-income countries, while less focus is put on providing low-cost treatments suitable for the majority of people in the world who have little or no access to radiotherapy. According to a study conducted by Abdel-Wahab *et al.*, optimal access to linear accelerators in low- and middle- income countries (LMICs) could save a million lives annually by 2035 [132]. Additionally, the conventional model of highly centralized radiotherapy networks, even in developed countries like Canada, Australia, and the UK, has reduced access to care and utilization rates due to the geographically dispersed patient populations, which makes the distance from a treatment center a crucial factor [133, 134, 135]. Thus, there is a potential requirement for more economical external beam radiation therapy systems in cancer care worldwide. One solution to this issue could be the implementation of lower energy kilovoltage x-ray technology, which is relatively inexpensive and requires less shielding and infrastructure.

Grid therapy was one of the earliest attempts to use kilovoltage photons for non-superficial lesion treatment in the early 1900s [136]. This method involved passing the primary photon beam through a metal ”grid” to create an array of parallel small photon beams. The purpose was to fractionate the radiation delivery spatially, thereby reducing skin complications. In recent years, various research groups have explored the potential of using kilovoltage photons to treat deep-seated lesions. For example, Loughery *et al.* aimed to develop and assess the feasibility of a compact kilovoltage intensity modulated radiotherapy platform for contrast-enhanced radiotherapy, which was found to be clinically feasible in both simulation and measurement [137]. Rose *et al.* used a modified CT scanner to treat brain metastases and reported a reduction in metastasis size while maintaining safe healthy brain doses [52]. Prionas *et al.* demonstrated the feasibility of using a dedicated breast CT scanner for the

---

[1] This work is under review in *Radiation and Oncology*

treatment of breast lesions [138], while Abbas *et al.* used a polycapillary optical cable to produce converging kilovoltage x rays with a focal spot size of 0.2 mm, resulting in a broadening of the entrance dose and resulting in a skin-sparing effect [139]. Likewise, Breitkreutz *et al.* developed a Monte Carlo (MC) model of a simple isocentric treatment kilovoltage arc therapy (kVAT) system that utilizes a customized collimator to produce a linear array of converging beamlets for treating deep-seated lesions with minimal damage to skin and organs at risk (OARs) [51, 140].

As we look at opportunities to introduce kV photon beams as a treatment modality for deep malignant lesions in geographic regions where radiotherapy is currently unavailable, one of the main challenges is that there is a lack of necessary tools and equipment for planning the treatment, such as computed tomography (CT) scanners and non-coplanar planning algorithms. The growing use of machine learning in combination with novel non-coplanar treatment planning strategies has the potential to address these issues.

Adaptive radiotherapy techniques often focus on using machine-learning augmented cone-beam CT (CBCT) to plan treatments [141]. By using the same advanced techniques and treatment planning tools, adaptive radiotherapy workflows can be repurposed to plan treatments in places without access to planning CTs, which is one of the obstacles to the implementation of low-cost radiotherapy. Various methods have been utilized to increase the use of CBCT images in RT, including model-based [142, 143, 86] and deep learning-based techniques [63, 64]. While some methods aim to correct specific types of CBCT artifacts such as beam hardening or cupping, a recent approach using deep learning methods generates higher-quality synthetic CT (sCT) directly from CBCT images. Dahiya *et al.* utilize a supervised image-to-image translation technique based on conditional generative adversarial networks (cGANs) to translate CBCT images to sCT images while also performing OAR segmentation driven by a novel physics-based artifact/noise-induction data augmentation pipeline [65]. The use of such algorithms has the potential to remove the necessity of a standalone planning CT from the radiotherapy workflow, lowering radiotherapy costs and thus be more accessible to LMICs.

Another large issue that arises when planning kV treatments is that the equispaced coplanar angles and trajectories used in clinical intensity modulated radiotherapy (IMRT) and volumetric modulated arc therapy (VMAT) plans, when used with kV beams, have exceptionally high skin dose. We address this issue by adopting more intelligent angle sampling schemes in non-coplanar directions. Some non-coplanar treatment planning algorithms have been developed for MV radiotherapy such as the station parameter optimized radiation therapy (SPORT) suite of algorithms. This includes segmentally boosted VMAT, dense angularly sampled and sparse intensity- modulated (DASSIM) radiation therapy, and an algorithm for fully automated Pareto optimal and clinically acceptable treatment planning [144, 145, 146]. In the work of Huang *et al.*, the non-coplanar Pareto optimal projection search (NC-POPS) algorithm is proposed for fully automated non-coplanar treatment planning to address these limitations [147]. However, to properly plan a kV isocentric treatment at depth, care must be taken to ensure adequate dose is delivered to the tumour as the source output is low compared to that of a linac and the dose calculation methods must be adapted to a kV beam which delivers dose more heterogeneously due to greater photoelectric interaction. Thus, a novel, dose-aware, non-coplanar beam optimizer is developed in this work specifically for kV planning.

In our work, we explored novel design parameters for a treatment system using a kV x-ray tube and an articulating, 4-geometry capable, low-cost gantry. This system leverages the decreased cost of a kV x-ray tube compared to the cost of an MV linac. Such a system could cost an-order-of-magnitude less than an MV system, with low operating costs, few specialised components, and low shielding requirements. The simplified isocentric kilovoltage arc (SITKA) treatment machine would avoid the estimated \$5M USD price of a new linac and \$1.5M USD additional cost of constructing the 2-metre thick cement bunker needed for safe operation of a linac [49].

## 7.2 Methods and Materials

### 7.2.1 System Overview

The SITKA machine design simulated in this study, shown in Figure 7.1, incorporated a commercially available, 14 mA, 320 kVp x-ray tube and an articulating, 4-$\pi$ geometry capable, low-cost gantry with a source-axis distance (SAD) of 40 cm. Mounted on a C-arm opposite the source is a CsI kV flat panel detector, which provided cone-beam CT (CBCT) imaging. The machine is positioned such that the machine isocenter aligns with the center of mass of the patients planning target volume (PTV) aligns with the isocenter. A deep learning CBCT to sCT method is employed to provide planning sCT. Machine learning OAR autosegmentation was used in combination with PTV contours drawn by remote radiation oncologists. A novel inverse treatment planning approach was employed, which used GPU backprojection to create a highly non-coplanar treatment plan with circular beams generated by an iris collimator. MC methods were used to evaluate different aspects of this machine, e.g., to test the treatment efficacy of the device and workflow, and to check compliance of two lung cancer patient plans against the Radiation Therapy Oncology Group (RTOG) 0813 protocols [79] for lung stereotactic ablative radiotherapy (SABR) treatments with a prescribed dose of 50 Gy. An overview of the system specification are shown in Table 7.1.

Two patients with lung cancer were treated with stereotactic ablative radiotherapy (SABR) using VMAT on a 6MV Truebeam linear accelerator. The patient's planning CT images, treatment plans were anonymized and used to create SITKA plans. No specific selection criteria were used for the patients in the study other than that they were suitable cases for lung SABR. CT data was composed of 512×512×163 voxels with dimensions of 0.977×0.977×2.00 mm. Patient 1's PTV was 49.5 cc located in the right lung while patient 2's PTV was 27.7 cc PTV located in the left lung.

Table 7.1: Design specifications of the SITKA system.

| | |
|---|---|
| Peak tube voltage [kVp] | 320 |
| Tube current at peak voltage [mA] | 14 |
| Focal spot size [mm] | 3.0 |
| Anode angle [deg] | 20 |
| Beam Filtration [Al-Sn-Cu] [mm] | [1.5-0.75-0.25] |
| Detector pixel pitch [mm] | 0.194 |
| Detector pixels [x-y] | [2,048-1,536] |
| Detector size [x-y] [cm] | [40.64-30.48] |
| Dose rate at 10 cm depth, 3 cm circular field size, 40 cm SAD [Gy/min] | 0.6 |
| Air kerma rates SSD 30 cm [mGy/s] | 35 |

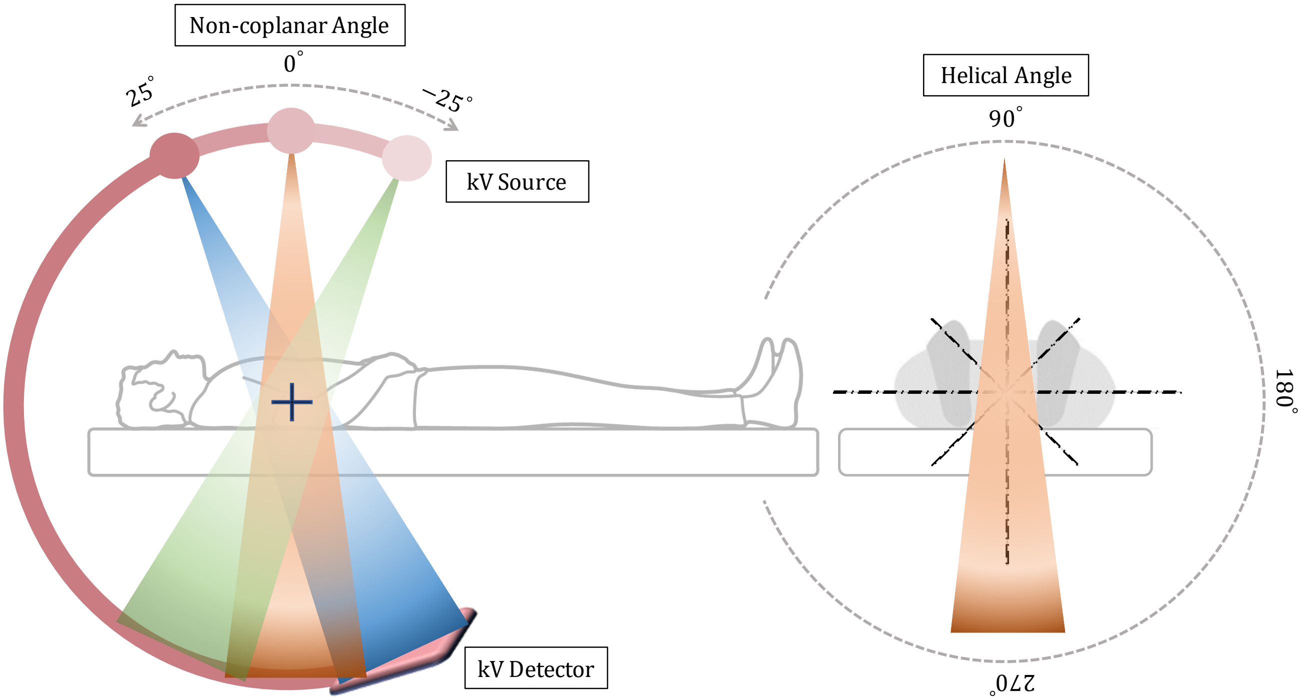

Figure 7.1: Schematic of the SITKA machine. A sagittal and axial view of a patient on the treatment couch is shown.

### 7.2.2 Synthetic CT Generation

The treatment planning optimization used a modification of Dahiya *et al.*'s sCT and auto-contouring generative machine learning models [65]. The machine learning model of Dahiya *et al.* was used to generate synthetic CT data from the CBCT data. The model was trained on the 95 locally advanced non-small cell lung cancer patients treated via intensity-modulated RT and concurrent chemotherapy, the same training as described in Dahiya *et al.* Due to memory limitations on most commercial GPUs, only 128 voxel cubes could be converted from CBCT to sCT. Therefore, a novel low-high-resolution stitching method was developed to convert the large patient volumes in this study. To achieve this, original dimension (high-resolution) data, down-sampled (low-resolution) data, and a normalization method were used to ensure consistent model outputs and avoid stitching artifacts.

First, overlapping low-resolution images were stitched together, with images cropped to a volume of interest of 256×400×128. This resulting image was downsampled by half in the $x$ and $y$ directions to create an image of 128×200×128. A uniform kernel with strides of 10 voxels in the $y$ direction was used to create images for stitching, and these images were saved and used as input for the model. The output of the model was normalized by ensuring that the overlap between consecutive windows had the same mean and standard deviation. The mean of all outputs for a given region of the images was taken to yield a low-resolution image.

Second, images were stitched together at the CBCT image resolution. Again, the volume of interest was cropped to 256×400×128, and a uniform kernel with strides of 16 in the $x$ and $y$ directions was used to create images for stitching. The images were stitched by matching the mean and standard deviation of each high-resolution image to the same region of the low-resolution image. This resulted in a high-resolution 512×512×128 image.

### 7.2.3 Non-coplanar Treatment Planning

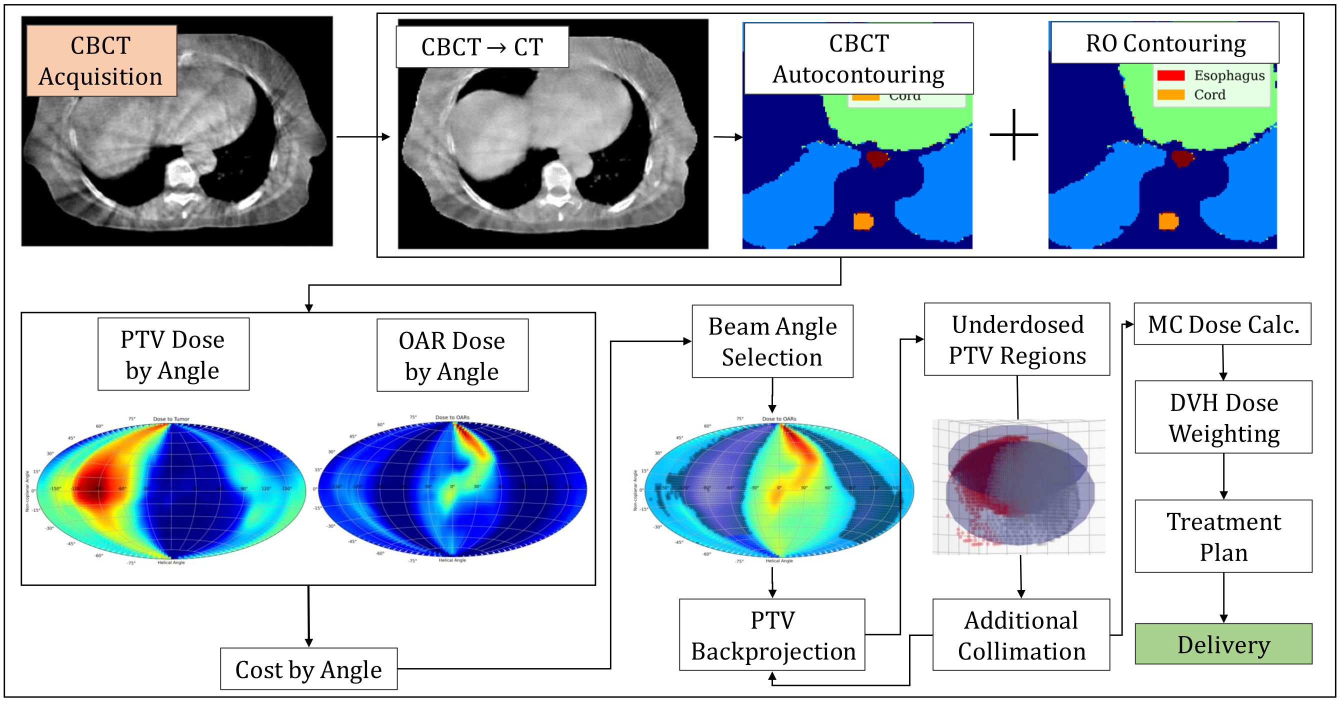

Figure 7.2: Overview of the treatment planning workflow starting with a CBCT acquisition and ending in beam delivery.

A high-speed GPU-based non-coplanar treatment planning algorithm, described in Figure 7.2 was employed to generate optimized SITKA treatment plans. Firstly, the tumor volume was converted into a point cloud and then fitted with a Gaussian mixture model (GMM) to determine the isocenter and dimensions of the treatment beam circular collimation. Since there are many possible arrangements of multiple fields in a tumour, the GMM finds the optimal position probabilistically for a given number of isocenters and defines the collimation at each isocenter, in this way automating the process of isocenter selection. In order to measure the radiation dose accurately in the tumor and OARs, the CT volume was adjusted from 100 kVp attenuation coefficients to 320 kVp attenuation coefficients using the Fastcat Python package [80]. A fifth-order polynomial curve was then generated from the reconstructed image values, which allowed the original 100 kVp CT's attenuation values to be converted to the 320 kVp attenuation values relevant for treatment beam dose calculations.

This conversion step could be done through material assignment in the sCT and assignment of an orthovoltage attenuation coefficient based on the material. In this case fastcat proved an elegant method for conversion as the attenuation coefficient for a given material according to the spectrum of the different polyenergetic beams is not easy to calculate. With the benefit being that once the calibration curve is created in fastcat, it can be reused without recalculation.

Next, attenuation through the modified CT volume was ray-traced using the TIGRE Python package [95] at equally spaced angles around a sphere centered at the isocenter. For each beam the attenuation before the tumour, in the tumour, as well as in OARs was calculated for 256x256 equally spaced rays originating in the source and ending in the plane of the tumour over a region 1.1 times the maximum projected size of the tumour. Three thousand angles were calculated using the method described in Appendix A, angles that entered on the boundary of the CT volume rejected. A 320 kVp x-ray beam was then ray-traced through in both the tumor and the OARs to determine the beam attenuation, using cylindrical collimation determined from the GMM dimensions. To obtain the dose in the tumor, the attenuation was divided by the relative electron density, which was acquired using the HU to relative electron density conversion tables of Bazalova-Carter *et al.* [148].

Angles were then selected based on a cost function that rewarded dose in the tumor and penalized dose in each OAR according to an individual weight. An initial cost is associated with each of the beams and the $n$ beam with the lowest cost ($n$ selected by user) are used in the further optimization. These beam angles were further weighted by the inverse of their dose to the tumor to produce uniform dose in the PTV from all angles. However, to spread out the skin dose, a minimum weighting of one third was given to the highest dose angles. The weighting was determined as follows

$$W_i = 1 - \frac{2D_i}{3D_{max}} \tag{7.1}$$

Where $W_i$ is the weighting for beam $i$, $D_i$ is the dose estimate for beam $i$ and $D_{max}$ is the maximum dose estimate.

The selected beam angles were then used to backproject and reconstruct doses using the FDK algorithm [96], providing an initial estimate of radiation dose in the PTV. Subsequently, areas that received insufficient dose were identified in the reconstruction. To rectify these underdosed areas, extra GMMs were fitted. Additional projection images are then generated with new collimation settings and isocenter positions derived from the GMM representing the underdosed region. Collimation adjustments aimed at delivering extra dose to these regions were computed based on the boundary shapes of each region in each projection image. The additional projected images through each underdosed region were added to the original projected images with a preliminary weighting of $W_r$

$$W_r = \frac{\mu_{PTV} - \mu_r}{\mu_{PTV}} \tag{7.2}$$

where $\mu_{PTV}$ is the mean of the PTV and $\mu_r$ is the mean of the region. This process was continued iteratively until the plan was deemed to be sufficiently conformal in the back projection by the treatment planner.

On a Linux workstation equipped with an Nvidia RTX 2070 GPU, treatment plans were completed in 28 and 26 seconds, for the patient 1 and 2, respectively. Patients 1 and 2 required 6 and 5 iterations, respectively, to achieve sufficient PTV uniformity.

### 7.2.4 Monte Carlo Dose Calculations

The dose calculations on the planning CT images were subsequently performed using the TOPAS MC [69] code. A total of $2 \times 10^9$ total particles were simulated for each collimation iteration recommended by the backprojection-based dose calculation algorithm, using the angles, weightings, and collimation provided by the treatment planning algorithm. This amounted to 6 and 5 times $2 \times 10^9$ particles for the first and second patient, respectively. The kV Fastcat simulation utilized an analytical x-ray source generated in Spekpy with an anode angle of 20° and a tube voltage of 320 kVp. The source was subject to additional analytical filtration of 1.5 mm aluminum, 0.75 mm tin, and 0.25 mm copper. The simulations used the Geant4 Penelope physics list with a particle range cutoff of 0.5 mm and were run on a Linux desktop computer equipped with 8 Intel Skylake CPUs, no variance reduction techniques were used. One isocenter position took four hours to simulate over all of the selected treatment beams. Dose was scored in the CT volume and compared to the doses calculated in the Eclipse treatment planning system for the VMAT plans for each patient, respectively.

Each patient was converted from HU values to materials using the method of Schneider *et al.* [74] using the default settings in Topas for this method. All materials were defined using cross section from the NIST database.

### 7.2.5 Collimation Setting Weighting

In order to ensure proper coverage of the PTV and conformality to the prescribed dose, as outlined in RTOG 0813 section 6.4 (as reproduced in table 1), a novel cost function was developed to weight MC for each collimation setting. To reduce noise in the MC dose distributions for each collimation setting, a Gaussian filter with a standard deviation of 0.6 was applied. The initial cost function was based on the coefficient of variation, which is a measure of the standard deviation relative to the mean of the PTV.

$$D_{PTV} = \Sigma_i x_i D_{PTV,i} \tag{7.3}$$

$$CV_{PTV} = \frac{\sigma_{D_{PTV}}}{\mu_{D_{PTV}}} \tag{7.4}$$

where $x_i$ are the weights for each collimation setting, $D_{PTV,i}$ is the part of the dose distribution inside the PTV for each collimation setting, and $D_{PTV}$ is the weighted dose distribution. The parameters $\sigma_{D_{PTV}}$ and $\mu_{D_{PTV}}$ represent the mean and standard deviation of the dose in the weighted PTV, respectively. This metric was selected because its minimization corresponds to achieving homogeneous coverage of the PTV. To minimize the cost, a limited-memory Broyden–Fletcher–Goldfarb–Shanno (L-BFGS) algorithm was utilized in Python, with initial weights set at 1 and bounds between 0.5 and 10 inclusive. These initial weights were then employed as the basis for an additional cost function centered around the RTOG 0813 constraints. Specifically, according to RTOG 0813, 90% of the prescribed dose must be delivered to 99% of the PTV volume, while 95% of the prescribed dose must be administered to 100% of the PTV. To ensure that the isodose surface selected satisfied these criteria, the dose ($D$) was scaled such that neither of the criteria were violated:

$$D_s = \min\{\text{percentile}(D_{PTV}, 5), \frac{1}{0.9}\text{percentile}(D_{PTV}, 1)\} \tag{7.5}$$

$$D' = 50\text{Gy}\frac{D}{D_s} \tag{7.6}$$

Where $D_s$ is the dose scaling factor, 50 Gy is the prescribed dose, and $D'$ is the scaled dose.

The next step involved maximizing dose conformity by minimizing the number of voxels above the prescription dose in the region 2 cm outside the PTV, which is referred to as the ”z ring”. This was achieved by using Powell's method [149] to generate an isodose surface that conforms to the PTV and meets the prescribed dose criteria. The cost function for this optimization process was defined as follows:

$$D_{high} = \text{percentile}(D_{PTV}, 95) \tag{7.7}$$

$$\text{Cost} = \Sigma[D_{zring} \cup D_{PTV}] > 50 \text{ Gy} + \Sigma[D_{zring} \cup D_{PTV}] > D_{high} \tag{7.8}$$

An additional term was incorporated to penalize the voxels outside the PTV that exceeded the 95th percentile of the PTV dose ($D_{high}$). This was deemed necessary to address cases where bony structures surrounding the PTV received high doses from the 320 kVp x-ray beam.

### 7.2.6 Treatment Time Calculation

In order to calculate the treatment time for the SITKA machine the x-ray tube model was simulated with the BEAMnrc package of EGSnrc [150]. The x-ray tube was modelled after a commercially available Comet x-ray tube. The x-ray anode, a tungsten block at an angle of 20°, received incident fluence of a 320 keV, 3 mm electron beam. Below the anode was the beam filtration of 4 modules made of 0.8 mm beryllium for the exit window and 1.5, 0.75, and 0.25 mm of aluminum, tin, and copper filtration, respectively. The beam was then collimated to a diameter of 3 cm at isocenter through a 2 mm thick circular lead collimator and a phase space was captured at the SAD of 40 cm. The conversion factor between the number of original electrons to the number of photons in the phase space, combined with the absolute dose calculated in Topas for a given treatment was used to calculate the treatment time needed to deliver one 10 Gy fraction from the 14 mA, 320 kVp x-ray tube.

## 7.3 Results and Discussion

### 7.3.1 Synthetic CT Generation

The sCT generation and auto-contouring (Figure 7.3) simultaneously lessened artifacts, improved contrast, and corrected CT numbers of the CBCT data, providing a step toward CBCT-based treatment planning. Pronounced CBCT motion artifacts that can be seen in the heart and diaphragm of Figure 7.3 a) were removed in the sCT allowing accurate dose calculation in these regions. Additionally, in Figure 7.3 b) the autocontouring correctly identifies the OARs in the volume, while Figure 7.3 c) shows the correction of the HU values from CBCT to sCT, a property essential for CBCT-based treatment planning and Figure 7.4 shows a profile through the planning CT and sCT, respectively. Although it is important to acknowledge that planning CTs may still contain motion and movement artifacts, they are conventionally preferred over CBCT for planning purposes due to their reduced motion artifact occurrence and greater tissue contrast. While this approach helps to minimize artifacts in CBCT scans, it is recognized that certain artifacts may still persist despite these efforts due to the fundamentals of CT acquisition.

Although the workflow in Figure 7.2 shows planning based on sCT, CT images instead were chosen for the dose calculation in this work to enable direct comparison to the VMAT plan. This approach was taken as DVH calculations based on the sCT would still contain artifacts from motion and the imperfect registration process that would introduce uncertainty in the results. Moving forward with the prototype machine, planning with the sCT images will need to be evaluated directly using dosimetry in phantoms.

### 7.3.2 Non-coplanar Treatment Planning

The novel treatment planning algorithm executed quickly to produce highly non-coplanar treatment plans, which avoided OARs, maximized tumour dose and only took 28 and 26 seconds to complete on an RTX 2070 GPU, for the two plans respectively. Optimal angles were seen to be two opposing bands of helical angles in both lung patients (Appendix A) which curve with the shape of the spine while avoiding the trachea, esophagus, and bronchial tree.

This optimization method resulted in 1204 beam positions for the first patient and 1020 beam positions were simulated in MC for the dose calculation each with a unique gantry angle and beam

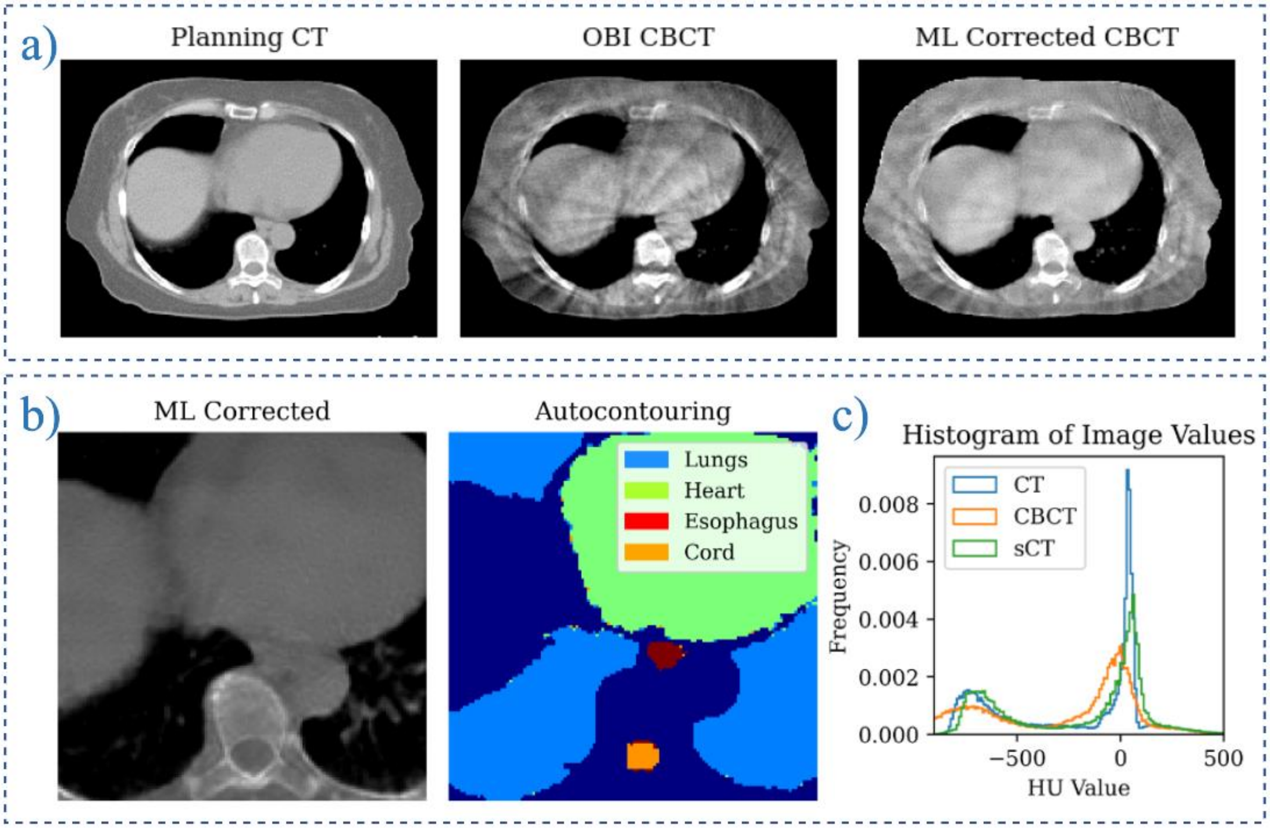

Figure 7.3: a) A planning CT is compared to a registered CBCT and the stitched, full-volume sCT. b) The auto-contouring capability of the model is demonstrated. c) The conversion from CBCT HU values to sCT HU values is seen.

weighting. Each beam position had a unique collimation setting to spare normal tissue. More information on the beam weighting can be found in Appendix A.

### 7.3.3 Treatment Plan evaluation

SITKA treatment plans, shown in Figure 7.5 showed conformal dose distributions and on average 6.7 and 4.9 Gy reduction of the maximum dose in soft tissue OARs for patients 1 and 2 respectively. This was accompanied by a small increase in mean dose of 0.17 and 0.30 Gy in soft tissue OARs for patients 1 and 2, respectively. This is reflected in the SITKA plan DVHs (Figure 7.6, Table 7.2) which showed an increase in the lower dose volume in most OARs, but a reduction of the maximum dose to the aorta, spinal cord, and esophagus due to the use of non-coplanar beams. A larger increase to mean rib dose (4.2 and 2.1 Gy, respectively) as compared to soft-tissue dose was observed due to the high photoelectric absorption of the 320 kVp beam in bone. However, the absolute mean doses to ribs were still modest at 9.15 and 4.5 Gy for the SITKA plans. The SITKA dose falloff according to the 50% and 20% isodose lines (Figure 7.5) were of similar conformality to the VMAT plan. Overall, the plan was deemed acceptable for clinical use by a radiation oncologist.

Table 7.2: RTOG 0813 table

| Structure | RTOG 0813 Limit [Gy] | | Patient 1 Dmean-Dmax [Gy] | | Patient 2 Dmean-Dmax [Gy] | |
|---|---|---|---|---|---|---|
| | Dose [Gy] | Volume | SITKA | VMAT | SITKA | VMAT |
| Cord | 13.5 | (<0.5 cc) | 2.26-8.38 | 1.60-11.8 | 1.92-11.6 | 1.71-16.3 |
| Trachea | 18 | (<4 cc) | 4.21-11.4 | 5.45-15.2 | 5.11-9.02 | 4.83-15.5 |
| Heart | 32 | (<15 cc) | 2.56-8.49 | 3.66-18.9 | 0.64-3.23 | 0.07-0.38 |
| Aorta | 47 | (<10 cc) | 4.49-22.6 | 3.11-25.2 | 1.73-7.87 | 2.07-16.5 |
| Esophagus | 27.5 | (<5 cc) | 3.51-8.11 | 3.36-13.1 | 2.82-9.34 | 2.56-16.2 |
| Ribs | N/A | N/A | 9.15-58.6 | 4.94-56.6 | 4.47-53.1 | 2.22-49.3 |
| Skin | 30 Gy | (<10 cc) | 3.21-16.21 | 2.00-21.2 | 2.16-16.6 | 1.40-22.7 |
| PTV | 50 | (Prescribed) | 59.2.0-70.1 | 58.2-63.8 | 54.3-60.3 | 58.1-62.3 |
| Criteria | RTOG 0813 Limit | | Patient 1 | | Patient 2 | |
| | Patient 1 | Patient 2 | SITKA | VMAT | SITKA | VMAT |
| Ratio of prescription isodose volume to PTV volume, (R100%) | <1.2 | <1.2 | 1.16 (PASS) | 1.02 (PASS) | 1.16 (PASS) | 1.05 (PASS) |
| Ratio of 50% prescription isodose volume to PTV volume (R50%) | <4.0 | <4.4 | 3.99 (PASS) | 3.74 (PASS) | 4.24 (PASS) | 4.11 (PASS) |
| Maximum dose at 2 cm from PTV in any direction (D2cm) | <31.5 Gy | <28 Gy | 25.74 (PASS) | 25.55 (PASS) | 27.34 (PASS) | 25.38 (PASS) |
| Percent of lung receiving 20 Gy or more V20 (%) | <10% | <10% | 7.06 (PASS) | 6.32 (PASS) | 3.52 (PASS) | 3.37 (PASS) |

Table 7.3: Treatment times for different dose regimes

| Cumulative Dose [Gy] | Fractions | Dose per Fraction [cGy] | Treatment time per Fraction [min:sec] | |
|---|---|---|---|---|
| | | | Patient 1 | Patient 2 |
| 60 | 5 | 1200 | 26:42 | 32:54 |
| | 8 | 750 | 16:41 | 20:56 |
| | 30 | 200 | 4:27 | 5:29 |
| 50 | 5 | 1000 | 22:15 | 27:25 |
| | 8 | 625 | 13:54 | 17:08 |
| | 25 | 200 | 4:27 | 5:29 |
| 48 | 4 | 1200 | 26:42 | 32:54 |
| | 8 | 600 | 13:21 | 6:27 |
| | 30 | 200 | 4:27 | 5:29 |

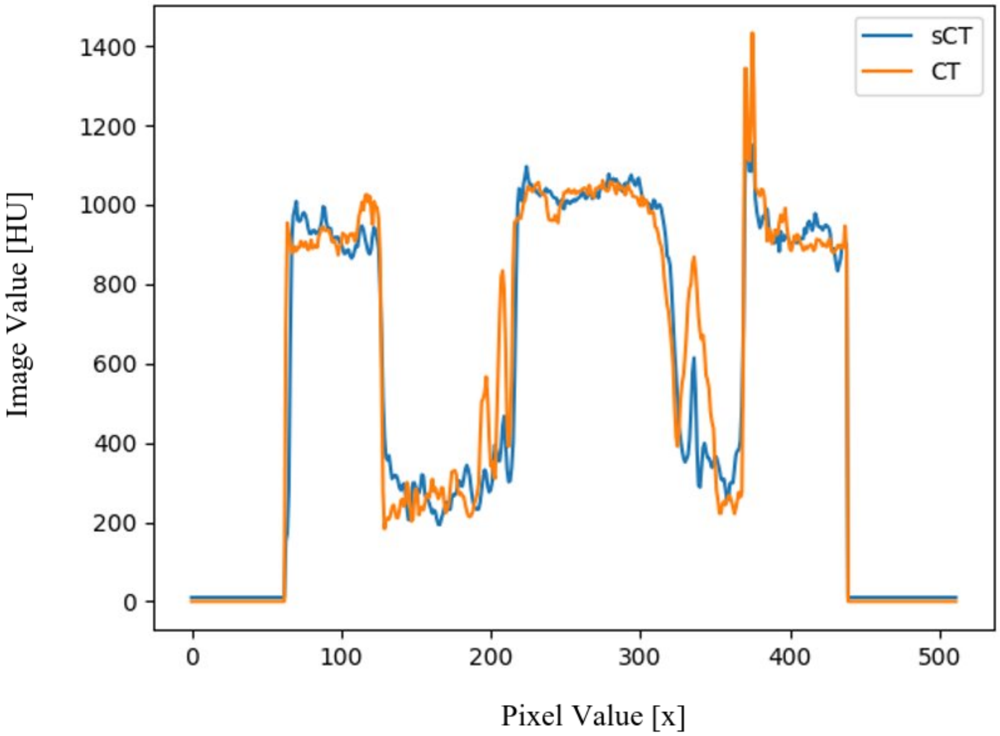

Figure 7.4: A profile through the lungs of the sCT and CT

Regarding RTOG 0813, both treatment plans met the dosimetric constraints for the PTV and the OARs without any violations (refer to Table 7.2). The most demanding constraints in both plans were achieving the ratio of 100% and 50% of the prescription isodose volume to the PTV volume ($R_{100\%}$ and $R_{50\%}$, respectively). This was challenging due to the Iris collimator's inability to provide arbitrary beam shapes, unlike the higher cost, multi-leaf collimator (MLC). With the limitation of using only cylindrical collimation produced by shifting a circular beam shape, SITKA isodose surfaces were characterized as more spherical than the arbitrary shapes provided by the MLC equipped VMAT plan. Consequently, these more spherical SITKA isodose surfaces provided less conformal coverage of the PTV than the VMAT surfaces. This was particularly evident in patient 1, where more homogenous PTV DVHs tended to include the rib bones in the prescription isodose and violate the $R_{50}\%$ constraint, as discussed in Appendix B, forcing the PTV DVH to be inhomogenous as seen in Figure 7.6. The non-coplanar method used differs significantly from previous methods such as the SPORT suite or DASSIM method. This was done as the device dose rate and beam constraints (high bone absorption) are different from those stipulated for MV beams.

To meet the $R_{100\%}$ and $R_{50\%}$ constraints in both plans, the dose allowances of 99% of the PTV volume receiving only 90% of the dose and 100% of the PTV receiving only 95% of the prescribed dose were used to compensate for areas of the PTV with irregular shapes that were challenging to cover with a spherical prescription isodose volume. It is important to note that the areas receiving

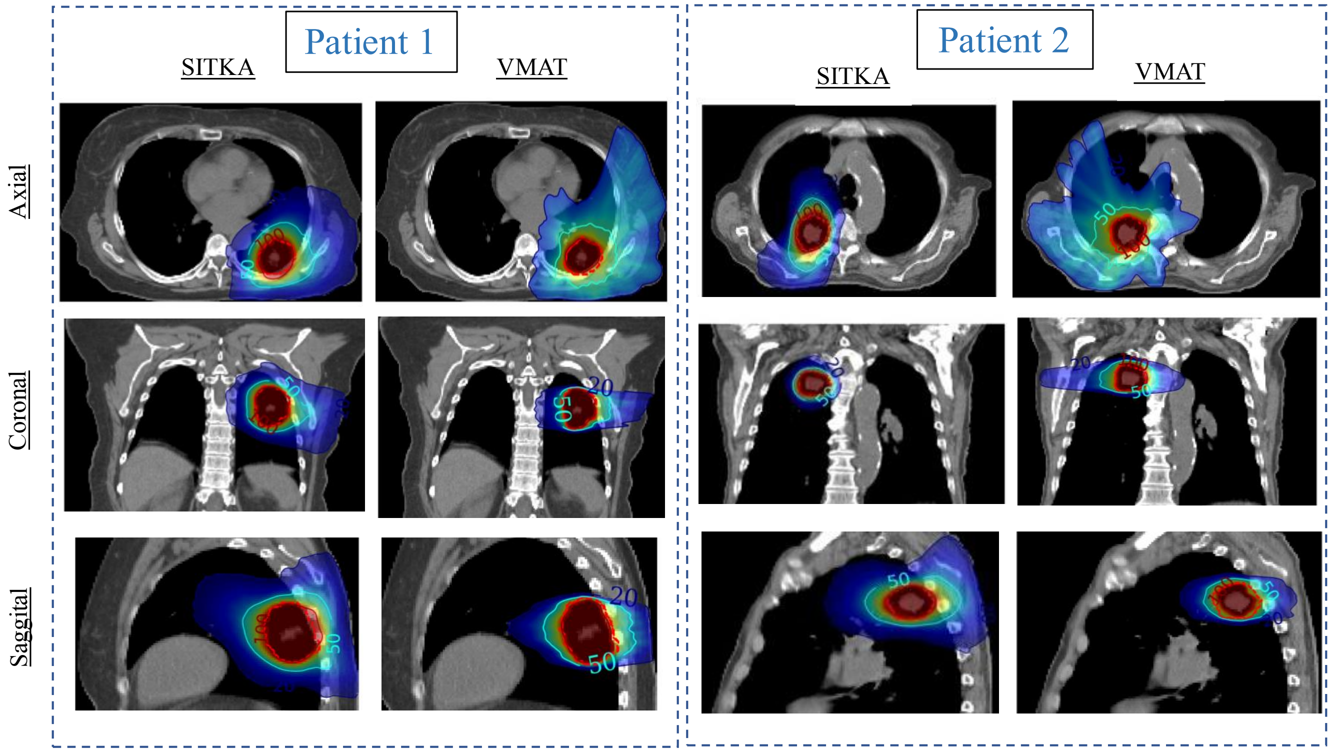

Figure 7.5: Lung dose distributions for bose patients are shown for a lung SABR patient using either SITKA or VMAT treatments, the PTV is denoted as the red dotted line, 100, 50, and 20% prescription isodose lines are shown in red, green, and blue.

less than 100% of the prescribed dose in the SITKA plan were strictly in the PTV margin and not in the gross tumor volume (GTV).

The machine specifications of the simulated device are unique and do not correspond to any existing radiotherapy device. However, it is worth noting that a device with similar specifications is currently being constructed by Sirius Medicine LLC (Halfmoon Bay, CA). Furthermore, all the design parameters used in this study are based on commercially available components. Some modifications have been made to the device specifications in order to maintain the confidentiality of Sirius Medicine's designs.

Additionally, while a prototype machine is under development, it is important to note that many of the design parameters have not yet been finalised. In order to assess the feasibility and potential of the device, this simulation study was conducted. During this study, various design parameters such as beam filtration, kVp, and detector model were set as proof of concept to showcase the attainable dose distributions. However, these parameters do not necessarily reflect the actual design characteristics of the prototype. They were selected solely for the purpose of demonstrating the potential capabilities of the device. Finalising the design parameters will require further research, rigorous testing, and expert analysis to ensure the device meets all necessary standards and safety requirements.

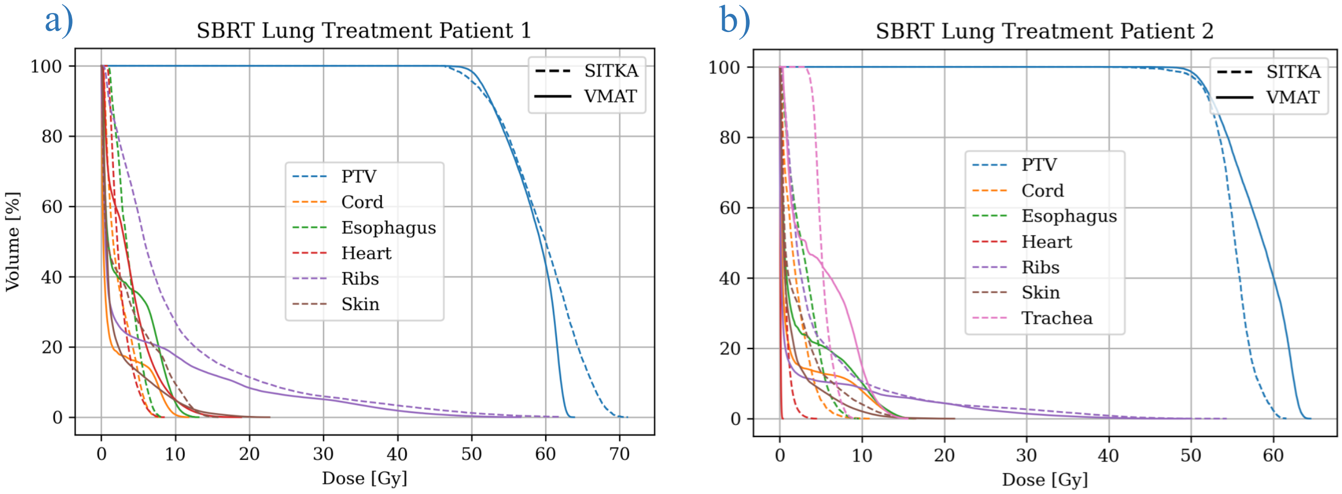

Figure 7.6: DVH curves computed for the SITKA and VMAT plans. are shown for both patient 1 (a) and patient 2 (b).

Lung patients were used in this study as the cancer has high prevalence in LMICs and in previous studies [140] it was shown to be a suitable site for treatment. Although there are other sites that have higher prevalence in LMICs, many of them, such as ovarian and head and neck cancers, prove hard to treat with non-coplanar beams due to the many organs at risk involved.

This conversion step could be done through material assignment in the sCT and assignment of an orthovoltage attenuation coefficient based on the material. In this case fastcat proved an elegant method for conversion as the attenuation coefficient for a given material according to the spectrum of the different polyenergetic beams is not easy to calculate. With the benefit being that once the calibration curve is created in fastcat, it can be reused without recalculation.

### 7.3.4 Limitations

A more sophisticated approach to treatment planning, involving optimized beam weighting by angle and beamlet-based inverse dose calculations, has the potential to create SITKA radiation treatment plans of greater conformality and target homogeneity than those discussed herein. Due to the fact that constraints on maximum and mean doses were well below RTOG 0813 limits in SITKA OARs we can see some latitude for such an optimization strategy to improve tumor doses conformity while still being in compliance with RTOG dose limits. This study employed MC treatment planning, recognized as the standard of excellence for dose calculations, as a step in the optimization in the absence of established, open-source analytical treatment planning tools. However, a key drawback of MC treatment planning is its speed, as demonstrated by the fact that a single simulation in this case took 8 hours to complete using 8 Intel Broadwell cores. Additionally, the backprojection-based algorithm employed in this study was inadequate in accounting for the inhomogeneities present in the lung, which is challenging to simulate through simple ray tracing techniques. Further work seeks to employ analytical inverse treatment planning, using beamlet methods or GPU MC techniques, to enable more sophisticated beam weighting.

Additional cost functions were chosen due to their direct relevance to DVHs, a crucial aspect for complying with RTOG guidelines. While the same approach could have been applied to the first cost function, the extensive parameters (hundreds of beams) would have hindered convergence of the optimization function. Additionally, the initial costs stem from swift 2D raytracing, while the subsequent cost functions derive from volumetric data. In summary, the first function minimizes variables, while the second produces an optimal dose distribution. Ideally, a rapid dose calculation algorithm with per-beam dose distribution would be ideal, but lacking this, MC-based calculation for each beam was too slow. Despite the complexity posed by numerous cost functions, this approach was necessary for satisfying DVH constraints in RTOG 0813. Future work should aim to streamline this process by consolidating cost functions.

An SAD of 40 cm is used in this study to increase the dose rate of the x-ray tube, however, this generates an increased risk of collision. While all source positions in this study were well away from the patient the exact dimensions of the treatment head including shielding are not known. During the development and testing stages of the device, extensive simulations and physical measurements will be conducted to assess and optimize the clearance around the patient so as to remove the possibility of collision. The goal is to provide adequate space while maintaining the necessary precision and accuracy required for effective radiotherapy treatments. Safety protocols and guidelines will be followed to ensure that patient collision issues are mitigated and that the treatment environment is optimized for patient comfort and safety.

One challenge associated with the extended duration of SITKA treatments is the need for patient immobilisation over an extended period. However, given that detector material employed has radioresistance properties to withstand treatment doses, the SITKA system offers the possibility of mid-treatment imaging, leveraging the suitability of the kilovoltage beam for imaging purposes. By incorporating mid-treatment imaging, it becomes feasible to verify and maintain accurate target positioning throughout the prolonged SITKA treatment sessions, thereby enhancing treatment precision.

The SITKA treatments for patients 1 and 2 were observed to have an estimated duration of 22 minutes and 15 seconds, and 27 minutes and 25 seconds, respectively, for each 10 Gy fraction based on the BEAMnrc models. While not as fast as conventional radiotherapy, this study aimed to show that adequate treatment plans could be achieved using a simple gantry mounted x-ray tube setup. It is important to note that the parameters employed in this work, such as beam weighting and beam filtration, included some trade-offs that reduced the treatment dose rates. To increase the dose rates, one may replace the inverse dose weighting approach used in this study, which assigned lower weights to high dose beam angles, with a more sophisticated beamlet inverse planning technique that could perhaps yield both conformal PTVs and high dose rates. A complete set of treatment times for different dose regimes can be seen in Table 7.3.

In the context of lung stereotactic ablative radiotherapy (SABR) treatments using a medical linear accelerator, the typical beam on time with a flattening filter is generally less than 4 minutes, while without the flattening filter it is approximately half that time for a 6 MV beam [151]. These treatment durations are associated with maximum dose rates of 4.0 Gy/min and 9.0 Gy/min, respectively, at a depth of 10 cm [151]. In contrast, the SITKA system has a maximum dose rate of 0.6 Gy/min at 10 cm depth, indicating longer treatment times. However, when comparing treatment times, it is worth noting that the SABR treatments using a medical linear accelerator still demonstrate more favourable durations than the cyberknife system, which typically requires between 60-90 minutes to treat a lung SABR patient [152]. Given this comparison, it would be valuable to explore additional techniques for increasing the dose rate on the SITKA system. This could potentially involve incorporating additional sources mounted on the gantry or utilising higher powered x-ray tubes to enhance treatment efficiency.

However, a conventional fraction of 2 Gy could be delivered by the SITKA system in 5 minutes. So, while the stringent dosimetric criteria for lung SABR have been followed here, as the fewer patient visits and commonality of lung lesions in LMICs make it an impactful treatment in the LMIC setting, the machine could also be used for more conventional treatments.

Additionally, the beam utilized in this study was hard for a kV beam, having been filtered by 0.75 mm tin. Employing a beam with less filtration would increase the dose rate while likely still maintaining the skin dose within the prescribed RTOG 0813 limit, as neither patient's skin dose was near the limit. In addition, higher current x-ray tubes are available than the 14 mA model employed in this study, which could further reduce the treatment times.

Overall, we present a straightforward design that can effectively deliver targeted doses to lung lesions while ensuring sufficient avoidance of OARs. The focus of our future work will be to build and characterize a prototype SITKA system for the delivery of veterinary treatments.

### 7.3.5 Further Treatments

The focus of this study has been on lung lesions in close proximity to the chest wall, which present challenges for kilovoltage treatments. Achieving uniform dose distributions becomes difficult due to tissue heterogeneity within the planning target volume (PTV), and the proximity of the tumour to the skin leads to the formation of hotspots near the skin in the dose distribution. Moreover, the presence of rib bones, which readily absorb kilovoltage dose, poses challenges in lung treatment.

However, the small size of the PTVs proves advantageous for kilovoltage treatments. Iris collimation and the short source-to-axis distance (SAD) of 40 cm are well-suited for treating smaller volumes. It should be noted that the current envisioned SITKA system is unlikely to be suitable for treating large irregular tumours due to the long treatment times required. Additionally, obese patients pose challenges due to the limited penetration of the kilovoltage beam.

Prostate patients may be suitable candidates for treatment using the SITKA system, given the central location of the tumour, which reduces the possibility of collision. However, it remains to be determined whether the non-coplanar planning can effectively accommodate constraints on all the OARs in that region. Breast cancer treatment would likely be feasible, as previous studies have demonstrated successful plans using kilovoltage beams [153]. Brain lesions are also expected to be amenable to treatment, considering the reasonable tissue depth and minimal risk of collision. The main drawback in brain treatments would be the absorption of kilovoltage dose by the bony skull, resulting in hotspots.

In summary, while lung lesions adjacent to the chest wall present challenges for kilovoltage treatments, the small PTV size and suitability for certain tumour sites like the prostate, breast, and brain indicate potential feasibility. However, limitations exist, such as the inability to treat large irregular tumours, challenges with obese patients, and considerations regarding OAR constraints in non-coplanar planning for certain treatment sites. Further research is necessary to explore these aspects and refine the application of low-cost radiotherapy treatment planning in diverse clinical scenarios.

## 7.4 Conclusion

The novel, low-cost, SITKA system in combination with adaptive machine learning methods and novel planning was demonstrated to provide RTOG 0813 compliant lung treatments to meet the urgent and increasing demand for radiotherapy treatment in LMICs.

# Chapter 8

# Conclusions

The approach undertaken in this PhD may appear unconventional by traditional standards. Taking a contrarian stance; MV beams have been employed for imaging and kilovoltage beams for treatment. This has been a deliberate departure from the long-standing convention followed by generations of physicists, who dedicated significant effort to produce MV beams in order to avoid using kilovoltage beams for treatment. Likewise, despite the substantial advancements achieved with kilovoltage on-board imagers in the realm of image guided radiotherapy, we have intentionally overlooked their remarkable progress.

The objective of this PhD is to reimagine radiotherapy development, retracing its path back 100 years on the treatment side, to an era when kilovoltage was the preferred modality, while simultaneously incorporating the advancements made in computation. Consequently, it can be argued that this PhD work opposes the technical feats of previous generations, a stance that can be justified in some circumstances. From this perspective, our cancer centers currently house unnecessarily expensive, burdensome RT machines akin to Ferraris—costly, challenging to maintain, and with many features unnecessary for the average user. However, perhaps there is an opportunity to introduce a radiotherapy solution equivalent to a Toyota Corolla: simple, efficient, and equally suitable for urban Mumbai as to urban America.

This research herein presents advancements towards this alternative radiotherapy solution. It introduces Fastcat (Chapter 3), a highly efficient CBCT simulator that significantly reduces simulation time by utilizing pre-calculated MC CBCT scatter and detector response functions. This technological improvement enables faster and more efficient CBCT simulations for both MV and kV imaging, while maintaining a high level of accuracy in comparison to measurements and traditional MC simulations. Furthermore, extensive validation of the Fastcat simulations demonstrates their ability to accurately reproduce key metrics such as MTF curves, HU values, and CNR, comparable to conventional MC simulations. Experimental validation against kV and MV CBCT images acquired with a Varian Truebeam linac further confirms the accuracy and reliability of the Fastcat simulator. A simulator on which much of the work in this thesis is based on.

The research also focuses on optimizing CBCT image quality by exploring innovative combinations of kV and MV beams and detector materials (Chapter 5 and 6) in an effort to employ lower cost imaging methods in radiotherapy. By comparing semiconductor methylammonium lead bromide perovskite crystals with four common detector materials, the study identifies Koning's dedicated breast CT and Varian's Truebeam kV- and MV-cone beam CT systems as suitable applications for perovskite detectors. Leveraging the system-specific Fastcat hybrid MC cone beam CT image simulation, the perovskite detector design is refined, resulting in device-specific optimal crystal thicknesses. Replacing current detectors with cost-effective perovskite crystal detectors has the potential to significantly enhance detective quantum efficiency and contrast-to-noise ratio in brain, lung, and bone tissues.

Likewise, the research introduces the SITKA system (Chapter 7), a low-cost treatment solution proposed for SABR lung patients in LMICs. The SITKA system incorporates a cost-effective gantry-mounted x-ray tube and integrates deep learning CBCT to sCT methods, along with a novel inverse treatment planning approach. This approach enables the generation of effective treatment plans that adhere to dosimetric criteria while minimizing maximum doses in OARs.

In summary, this research contributes to the ongoing development of CBCT simulation techniques, image quality optimization, integration of novel detector materials, and the development of a low-cost treatment machines . These achievements have the potential to improve the efficiency, accuracy, and accessibility of radiotherapy, with the goal of making an impact on the lives of the many people in the world who are burdened with cancer but lack access to treatment.

## 8.1 Future Direction

A recommendation for a new direction in low cost radiotherapy treatment would be a workflow that combines many of the aspects of this thesis; integrating the SITKA treatment system with a perovskite detector, CBCT to sCT machine learning methods and utilizing GPU Monte Carlo simulations in conjunction with the Fastcat simulation method for treatment planning an idealized system could be constructed. This treatment paradigm could have the potential to significantly improve radiotherapy efficiency, and accessibility, particularly in LMICs.

The SITKA system offers a cost-effective treatment solution for treatments in LMICs, thanks to its affordable gantry-mounted x-ray tube and integration of deep learning CBCT to synthetic CT methods to avoid the added cost of a planning CT, along with a novel inverse treatment planning approach. By incorporating the SITKA non-coplanar geometries, it enables the generation of effective treatment plans that adhere to dosimetric criteria while minimizing maximum doses in OARs. This would greatly enhance the quality and precision of radiotherapy treatments for patients in resource-constrained settings where more penetrating MV machines are infeasible.

Additionally, integrating a perovskite detector into the treatment machine would capitalize on the superior image quality predicted to be attainable by these low-cost detectors. By replacing existing detectors with cost-effective perovskite crystal detectors, the machine could enhance detective quantum efficiency and contrast-to-noise ratio in tissues enabling high quality CBCT imaging and in turn higher quality sCT. This improvement in image quality could result in more accurate treatment guidance and improved patient outcomes. To further enhance the capabilities of the treatment machine, the incorporation of GPU MC simulations alongside the Fastcat simulation method in terms of treatment planning. This integration would significantly reduce simulation time and improve overall efficiency. By harnessing the computational power of GPUs, the machine would achieve faster and more efficient dose calculations for treatments, while maintaining a high level of accuracy. These advancement would enable quicker treatment planning and delivery, ultimately facilitating timely access to radiotherapy for more patients.

Another future direction of this work involves integrating photon counting capabilities into the perovskite detector and introducing high-Z adjuvants, such as gold nanoparticles (GNPs) or injected iodine, into kV treatments [53, 154, 155]. High-Z adjuvants have a large cross section for the photoelectric effect and can selectively accumulate in tumors, enabling targeted tumor treatments. kV photons, in turn, interact more readily through the photoelectric effect, making the benefits of these adjuvants particularly pronounced in kV treatments as compared to MV treatments. Likewise, perovskite detectors, being direct conversion detectors, have the advantage of photon counting, allowing for the detection of incident particle quantity and energy [156, 157, 158]. Incorporating this capability into a prospective treatment system would allow the eliminate of much of the low-energy scatter incident on the detector and mitigate beam hardening effects caused by preferential weighting of higher-energy radiation, an effect seen in energy integrating detectors. The integration of these two technologies into a prospective kV treatment system could improve both treatment planning and treatment efficacy by enhancing image quality and enabling targeted tumor treatment, ultimately enhancing the overall performance of the low-cost system.

In summary, by combining the SITKA treatment system with a perovskite detector and GPU Monte Carlo simulations combined with Fastcat based treatment planning, a future treatment machine would provide a not only adequate but perhaps state-of-the-art solution for radiotherapy in LMICs as well as perhaps applications in high-income countries. This integrated approach could enhance treatment accuracy, optimize image quality, and offer a cost-effective means of delivering precise radiotherapy.

# Bibliography

[1] Cancer in Developing Countries, Cancer – A neglected health problem in developing countries, INCTR, http://www.inctr.org/about-inctr/cancer-indeveloping- countries/.

[2] Canadian Cancer Statistics Advisory Committee. Canadian Cancer Statistics 2021, 2021.

[3] UN General Assembly. Political Declaration of the High-level Meeting of the General Assembly on the Prevention and Control of Non-communicable Diseases. A/RES/66/2. Technical Report January, 2012.

[4] World health Organization. WHO Global Coordination Mechanism on the Prevention and Control of NonCommunicable Diseases. *WHO Publication*, 2018.

[5] Massoud Samiei. Challenges of making radiotherapy accessible in developing countries. *Cancer Control*, 2013.

[6] Elizabeth R. Claridge Mackonis, Nicholas Hardcastle, and Annette Haworth. Stereotactic ablative body radiation therapy (SABR) in NSW. *Physical and Engineering Sciences in Medicine*, 43(2), 2020.

[7] David A. Palma, Robert Olson, Stephen Harrow, Rohann J.M. Correa, Famke Schneiders, Cornelis J.A. Haasbeek, George B. Rodrigues, Michael Lock, Brian P. Yaremko, Glenn S. Bauman, Belal Ahmad, Devin Schellenberg, Mitchell Liu, Stewart Gaede, Joanna Laba, Liam Mulroy, Sashendra Senthi, Alexander V. Louie, Anand Swaminath, Anthony Chalmers, Andrew Warner, Ben J. Slotman, Tanja D. De Gruijl, Alison Allan, and Suresh Senan. Stereotactic ablative radiotherapy for the comprehensive treatment of 4-10 oligometastatic tumors (SABR-COMET-10): Study protocol for a randomized phase III trial. *BMC Cancer*, 19(1), 2019.

[8] David A. Palma, Robert Olson, Stephen Harrow, Stewart Gaede, Alexander V. Louie, Cornelis Haasbeek, Liam Mulroy, Michael Lock, George B. Rodrigues, Brian P. Yaremko, Devin Schellenberg, Belal Ahmad, Sashendra Senthi, Anand Swaminath, Neil Kopek, Mitchell Liu, Karen Moore, Suzanne Currie, Roel Schlijper, Glenn S. Bauman, Joanna Laba, X. Melody Qu, Andrew Warner, and Suresh Senan. Stereotactic ablative radiotherapy for the comprehensive treatment of oligometastatic cancers: Long-term results of the SABR-COMET Phase II randomized trial. *Journal of Clinical Oncology*, 38(25):2830–2838, 9 2020.

[9] Charlotte Billiet, Ines Joye, Carole Mercier, Lieselotte Depuydt, Geert De Kerf, Peter Vermeulen, Steven Van Laere, Erik Van de Kelft, Paul Meijnders, Dirk Verellen, and Piet Dirix. Outcome and toxicity of hypofractionated image-guided SABR for spinal oligometastases. *Clinical and Translational Radiation Oncology*, 24, 2020.

[10] Shan Li and Liangfang Shen. Radiobiology of stereotactic ablative radiotherapy (SABR): Perspectives of clinical oncologists. *Journal of Cancer*, 11(17), 2020.

[11] David Asher, Pablo Munoz-Schuffenegger, Wellington F. P. Neves-Junior, Heloisa A. Carvalho, Alan Dal Pra, and Fabio Y. Moraes. Practical considerations of lung stereotactic ablative radiotherapy in the developing world. *Therapeutic Radiology and Oncology*, 3, 2019.

[12] Shane Mesko, He Wang, Samuel Tung, Congjun Wang, Dario Pasalic, Bhavana V. Chapman, Amy C. Moreno, Jay P. Reddy, Adam S. Garden, David I. Rosenthal, G. Brandon Gunn, Steven J. Frank, Clifton D. Fuller, William Morrison, and Jack Phan. Estimating PTV Margins in Head and Neck Stereotactic Ablative Radiation Therapy (SABR) Through Target Site Analysis of Positioning and Intrafractional Accuracy. *International Journal of Radiation Oncology Biology Physics*, 106(1), 2020.

[13] He Wang, Congjun Wang, Samuel Tung, Andrew Wilson Dimmitt, Pei Fong Wong, Mark A. Edson, Adam S. Garden, David I. Rosenthal, Clifton D. Fuller, Gary B. Gunn, Vinita Takiar, Xin A. Wang, Dershan Luo, James N. Yang, Jennifer Wong, and Jack Phan. Improved setup and positioning accuracy using a three-point customized cushion/mask/bite-block immobilization system for stereotactic reirradiation of head and neck cancer. *Journal of Applied Clinical Medical Physics*, 17(3), 2016.

[14] Linear Accelerator (LINAC) Price Guide & Costs, https://www.oncologysystems.com /resources/linear-accelerator-guides/used-linac-price, 2021.

[15] Mareike Held, Penny K. Sneed, Shannon E. Fogh, Jean Pouliot, and Olivier Morina. Feasibility of MV CBCT-based treatment planning for urgent radiation therapy: Dosimetric accuracy of MV CBCT-based dose calculations. *Journal of Applied Clinical Medical Physics*, 16(6), 2015.

[16] Irina Malajovich, Boon Keng Kevin Teo, Heather Petroccia, James M. Metz, Lei Dong, and Taoran Li. Characterization of the megavoltage cone-beam computed tomography (MV-CBCT) system on HalcyonTM for IGRT: Image quality benchmark, clinical performance, and organ doses. *Frontiers in Oncology*, 9(JUN), 2019.

[17] Josh Star-Lack, Daniel Shedlock, Dennis Swahn, Dave Humber, Adam Wang, Hayley Hirsh, George Zentai, Daren Sawkey, Isaac Kruger, Mingshan Sun, Eric Abel, Gary Virshup, Mihye Shin, and Rebecca Fahrig. A piecewise-focused high DQE detector for MV imaging. *Medical Physics*, 42(9):5084–5099, 9 2015.

[18] David Parsons and James L. Robar. Beam generation and planar imaging at energies below 2.40 MeV with carbon and aluminum linear accelerator targets. *Medical Physics*, 39(7Part2):4568–4578, 7 2012.

[19] David Parsons and James L. Robar. Planar imaging at energies below 2.4 MV with carbon and aluminum linear. In *IFMBE Proceedings*, 2013.

[20] James L. Robar, David Parsons, Avery Berman, and Alex MacDonald. Volume-of-interest cone-beam CT using a 2.35 MV beam generated with a carbon target. *Medical Physics*, 39(7):4209–4218, 2012.

[21] Marios Myronakis, Pascal Huber, Mathias Lehmann, Rony Fueglistaller, Matthew Jacobson, Yue Houng Hu, Paul Baturin, Adam Wang, Mengying Shi, Thomas Harris, Daniel Morf, and Ross Berbeco. Low-dose megavoltage cone-beam computed tomography using a novel multi-layer imager (MLI). *Medical Physics*, 47(4):1827–1835, 4 2020.

[22] Marios Myronakis, Josh Star-Lack, Paul Baturin, Joerg Rottmann, Daniel Morf, Adam Wang, Yue Houng Hu, Daniel Shedlock, and Ross I. Berbeco. A novel multilayer MV imager computational model for component optimization:. *Medical Physics*, 44(8):4213–4222, 8 2017.

[23] Hyungdong Kim, Byungyong Kim, Jonggeun Baek, Youngkee Oh, Sangmo Yun, and Hyunsoo Jang. Investigation of the use of external aluminium targets for portal imaging in a medical accelerator using Geant4 monte carlo simulation. *British Journal of Radiology*, 91(1084), 2018.

[24] S. Flampouri, P. M. Evans, F. Verhaegen, A. E. Nahum, E. Spezi, and M. Partridge. Optimization of accelerator target and detector for portal imaging using Monte Carlo simulation and experiment. *Physics in Medicine and Biology*, 47(18):3331–3349, 9 2002.

[25] Jonggeun Baek, Hyungdong Kim, Byungyong Kim, Youngkee Oh, and Hyunsoo Jang. Assessment of portal image resolution improvement using an external aluminum target and polystyrene electron filter. *Radiation Oncology*, 14(1):70, 4 2019.

[26] Emma Dennis, Soumya Kundu, Deepak Thrithamarassery Gangadharan, Jingjun Huang, Victor M. Burlakov, Devon Richtsmeier, Magdalena Bazalova-Carter, David C. Leitch, and Makhsud I. Saidaminov. High length-to-width aspect ratio lead bromide microwiresviaperovskite-induced local concentration gradient for X-ray detection. *CrystEngComm*, 23(11), 2021.

[27] Sergii Yakunin, Mykhailo Sytnyk, Dominik Kriegner, Shreetu Shrestha, Moses Richter, Gebhard J. Matt, Hamed Azimi, Christoph J. Brabec, Julian Stangl, Maksym V. Kovalenko, and Wolfgang Heiss. Detection of X-ray photons by solution-processed lead halide perovskites. *Nature Photonics*, 9(7), 2015.

[28] Haotong Wei, Yanjun Fang, Padhraic Mulligan, William Chuirazzi, Hong Hua Fang, Congcong Wang, Benjamin R. Ecker, Yongli Gao, Maria Antonietta Loi, Lei Cao, and Jinsong Huang. Sensitive X-ray detectors made of methylammonium lead tribromide perovskite single crystals. *Nature Photonics*, 10(5), 2016.

[29] Yong Churl Kim, Kwang Hee Kim, Dae Yong Son, Dong Nyuk Jeong, Ja Young Seo, Yeong Suk Choi, In Taek Han, Sang Yoon Lee, and Nam Gyu Park. Printable organometallic perovskite enables large-area, low-dose X-ray imaging. *Nature*, 550(7674), 2017.

[30] Shreetu Shrestha, René Fischer, Gebhard J. Matt, Patrick Feldner, Thilo Michel, Andres Osvet, Ievgen Levchuk, Benoit Merle, Saeedeh Golkar, Haiwei Chen, Sandro F. Tedde, Oliver Schmidt, Rainer Hock, Manfred Rührig, Mathias Göken, Wolfgang Heiss, Gisela Anton, and Christoph J. Brabec. High-performance direct conversion X-ray detectors based on sintered hybrid lead triiodide perovskite wafers. *Nature Photonics*, 11(7), 2017.

[31] Fei Ye, Hong Lin, Haodi Wu, Lu Zhu, Zhanfeng Huang, Dan Ouyang, Guangda Niu, and Wallace C.H. Choy. High-Quality Cuboid CH3NH3PbI3 Single Crystals for High Performance X-Ray and Photon Detectors. *Advanced Functional Materials*, 29(6), 2019.

[32] Yanmin Huang, Lu Qiao, Yuanzhi Jiang, Tingwei He, Run Long, Fan Yang, Lin Wang, Xiaojuan Lei, Mingjian Yuan, and Jun Chen. A-site Cation Engineering for Highly Efficient MAPbI3 Single-Crystal X-ray Detector, 2019.

[33] Peter Capper Safa Kasap. *Springer Handbook of Electronic and Photonic Materials*. 2017.

[34] Hardeep Singh Gill, Bassem Elshahat, Akshay Kokil, Lian Li, Ravi Mosurkal, Piotr Zygmanski, Erno Sajo, and Jayant Kumar. Flexible perovskite based X-ray detectors for dose monitoring in medical imaging applications. *Physics in Medicine*, 5, 2018.

[35] Bhavana Butey, Swatika Butey, Bhakti Patankar, V. D. Raut, Mugdha Dambhare, and S. V. Moharil. Current status of perovskite in X-ray detection for medical imaging technology. In *Journal of Physics: Conference Series*, volume 1913, 2021.

[36] Wenjuan Zhu, Wenbo Ma, Yirong Su, Zeng Chen, Xinya Chen, Yaoguang Ma, Lizhong Bai, Wenge Xiao, Tianyu Liu, Haiming Zhu, Xiaofeng Liu, Huafeng Liu, Xu Liu, and Yang Yang. Low-dose real-time X-ray imaging with nontoxic double perovskite scintillators. *Light: Science and Applications*, 9(1), 2020.

[37] Yue Houng Hu, Marios Myronakis, Joerg Rottmann, Adam Wang, Daniel Morf, Daniel Shedlock, Paul Baturin, Josh Star-Lack, and Ross Berbeco. A novel method for quantification of beam's-eye-view tumor tracking performance. *Medical Physics*, 44(11):5650–5659, 11 2017.

[38] Samuel J. Blake, Philip Vial, Lois Holloway, Peter B. Greer, Aimee L. McNamara, and Zdenka Kuncic. Characterization of optical transport effects on EPID dosimetry using Geant4. *Medical Physics*, 40(4):041708, 3 2013.

[39] Mengying Shi, Marios Myronakis, Yue-Houng Hu, Matthew Jacobson, Mathias Lehmann, Rony Fueglistaller, Pascal Huber, Paul Baturin, Adam Wang, Dianne Ferguson, Thomas Harris, Daniel Morf, and Ross Berbeco. A novel method for fast image simulation of flat panel detectors. *Physics in medicine and biology*, 64(9):095019, 2019.

[40] Josh Star-Lack, Mingshan Sun, Andre Meyer, Daniel Morf, Dragos Constantin, Rebecca Fahrig, and Eric Abel. Rapid Monte Carlo simulation of detector DQE(f). *Medical Physics*, 41(3), 2014.

[41] Joerg Rottmann, Daniel Morf, Rony Fueglistaller, George Zentai, Josh Star-Lack, and Ross Berbeco. A novel EPID design for enhanced contrast and detective quantum efficiency. *Physics in Medicine and Biology*, 61(17):6297–6306, 8 2016.

[42] C. Kausch, B. Schreiber, F. Kreuder, R. Schmidt, and O. Dössel. Monte carlo simulations of the imaging performance of metal plate/phosphor screens used in radiotherapy. *Medical Physics*, 26(10):2113–2124, 1999.

[43] C. Kirkby and R. Sloboda. Comprehensive Monte Carlo calculation of the point spread function for a commercial a-Si EPID. *Medical Physics*, 32(4):1115–1127, 2005.

[44] Julien Bert, Hector Perez-Ponce, Ziad El Bitar, Sébastien Jan, Yannick Boursier, Damien Vintache, Alain Bonissent, Christian Morel, David Brasse, and Dimitris Visvikis. Geant4-based Monte Carlo simulations on GPU for medical applications. *Physics in Medicine and Biology*, 58(16):5593–5611, 8 2013.

[45] Andreu Badal and Aldo Badano. Accelerating Monte Carlo simulations of photon transport in a voxelized geometry using a massively parallel graphics processing unit. *Medical Physics*, 36(11):4878–4880, 2009.

[46] Guillaume Landry, François deBlois, and Frank Verhaegen. ImaSim, a software tool for basic education of medical x-ray imaging in radiotherapy and radiology. *Frontiers in Physics*, 1, 2013.

[47] Brent van der Heyden, Lotte E.J.R. Schyns, Mark Podesta, Ana Vaniqui, Isabel P. Almeida, Guillaume Landry, and Frank Verhaegen. VOXSI: A voxelized single- and dual-energy CT scenario generator for quantitative imaging. *Physics and Imaging in Radiation Oncology*, 6:47–52, 4 2018.

[48] Ehsan Abadi, Brian Harrawood, Shobhit Sharma, Anuj Kapadia, William P. Segars, and Ehsan Samei. DukeSim: A realistic, rapid, and scanner-specific simulation framework in computed tomography. *IEEE Transactions on Medical Imaging*, 38(6):1457–1465, 6 2019.

[49] Dylan Y. Breitkreutz, Michael D. Weil, and Magdalena Bazalova-Carter. External beam radiation therapy with kilovoltage x-rays, 2020.

[50] Wonmo Sung and Jan Schuemann. Energy optimization in gold nanoparticle enhanced radiation therapy. *Physics in Medicine and Biology*, 63(13), 2018.

[51] Dylan Y. Breitkreutz, Michael D. Weil, Sergei Zavgorodni, and Magdalena Bazalova-Carter. Monte Carlo simulations of a kilovoltage external beam radiotherapy system on phantoms and breast patients:. *Medical Physics*, 44(12), 2017.

[52] J. Holt Rose, Amos Norman, Marylou Ingram, Chuck Aoki, Tim Solberg, and Albert Mesa. First radiotherapy of human metastatic brain tumors delivered by a computerized tomography scanner (CTRx). *International Journal of Radiation Oncology Biology Physics*, 45(5), 1999.

[53] A. V. Mesa, A. Norman, T. D. Solberg, J. J. Demarco, and J. B. Smathers. Dose distributions using kilovoltage x-rays and dose enhancement from iodine contrast agents. *Physics in Medicine and Biology*, 44(8), 1999.

[54] Jerrold T. Bushberg, J. Anthony. Seibert, Edwin Marion. Leidholdt, and John M. Boone. *The essential physics of medical imaging.*

[55] Harold Elford Johns and John Robert Cunningham. *The Physics of Radiology; a reivew*, volume 55. 1983.

[56] E. Podgorsak. Radiation Physics for Medical Physicists, Biological and Medical Physics Biomedical Engineering. *Springer*, 1999(December), 2006.

[57] G T Herman. *Fundamentals of Computerized Tomography*, volume 224. 2009.

[58] Daniel W. Rickey. Rotating Anode Image.

[59] Nicole T. Ranger, Ehsan Samei, James T. Dobbins, and Carl E. Ravin. Assessment of detective quantum efficiency: Intercomparison of a recently introduced international standard with prior methods. *Radiology*, 243(3), 2007.

[60] James T. Dobbins, Ehsan Samei, Nicole T. Ranger, and Ying Chen. Intercomparison of methods for image quality characterization. II. Noise power spectrum. *Medical Physics*, 33(5), 2006.

[61] Ian J Goodfellow, Jean Pouget-Abadie, Mehdi Mirza, Bing Xu, David Warde-Farley, Sherjil Ozair, Aaron Courville, and Yoshua Bengio. Generative Adversarial Nets. Technical report.

[62] Xin Yi, Ekta Walia, and Paul Babyn. Generative adversarial network in medical imaging: A review. *Medical Image Analysis*, 58, 12 2019.

[63] Yanbo Zhang and Hengyong Yu. Convolutional Neural Network Based Metal Artifact Reduction in X-Ray Computed Tomography. *IEEE Transactions on Medical Imaging*, 37(6), 2018.

[64] Shiyu Xu, Peter Prinsen, Jens Wiegert, and Ravindra Manjeshwar. Deep residual learning in CT physics: Scatter correction for spectral CT. In *2017 IEEE Nuclear Science Symposium and Medical Imaging Conference, NSS/MIC 2017 - Conference Proceedings*, 2018.

[65] Navdeep Dahiya, Sadegh R. Alam, Pengpeng Zhang, Si Yuan Zhang, Tianfang Li, Anthony Yezzi, and Saad Nadeem. Multitask 3D CBCT-to-CT translation and organs-at-risk segmentation using physics-based data augmentation. *Medical Physics*, 48(9), 2021.

[66] Olaf Ronneberger, Philipp Fischer, and Thomas Brox. U-Net: Convolutional Networks for Biomedical Image Segmentation. pages 234–241. 2015.

[67] Fabian Isensee, Jens Petersen, Andre Klein, David Zimmerer, Paul F Jaeger, Simon Kohl, Jakob Wasserthal, Gregor Köhler, Tobias Norajitra, Sebastian Wirkert, and Klaus H Maier-Hein. nnU-Net: Self-adapting Framework for U-Net-Based Medical Image Segmentation. Technical report.

[68] Getao Du, Xu Cao, Jimin Liang, Xueli Chen, and Yonghua Zhan. Medical image segmentation based on U-Net: A review. *Journal of Imaging Science and Technology*, 64(2), 2020.

[69] J Perl, J Shin, J Schumann, B Faddegon, and H Paganetti. TOPAS: An innovative proton Monte Carlo platform for research and clinical applications. *Medical Physics*, 39:6818, 2012.

[70] I. Kawrakow and B. R.B. Walters. Efficient photon beam dose calculations using DOSXYZnrc with BEAMnrc. *Medical Physics*, 33(8), 2006.

[71] S. Agostinelli and et al. Geant4 a simulation toolkit. *Nuclear Instruments and Methods in Physics Research Section A: Accelerators, Spectrometers, Detectors and Associated Equipment*, 506(3):250–303, 7 2003.

[72] W. A. Wagenaar. Generation of random sequences by human subjects: A critical survey of literature. *Psychological Bulletin*, 77(1), 1972.

[73] David Johnston. 12. RdRand and RdSeed Instructions in x86 CPUs. In *Random Number Generators—Principles and Practices*. 2018.

[74] Wilfried Schneider, Thomas Bortfeld, and Wolfgang Schlegel. Correlation between CT numbers and tissue parameters needed for Monte Carlo simulations of clinical dose distributions. *Physics in Medicine and Biology*, 45(2), 2000.

[75] W. P. Segars, G. Sturgeon, S. Mendonca, Jason Grimes, and B. M.W. Tsui. 4D XCAT phantom for multimodality imaging research. *Medical Physics*, 37(9):4902–4915, 2010.

[76] Hosang Jeon, Hanbean Youn, Jin Sung Kim, Jiho Nam, Jayoung Lee, Juhye Lee, Dahl Park, Wontaek Kim, Yongkan Ki, and Donghyun Kim. Generation of polychromatic projection for dedicated breast computed tomography simulation using anthropomorphic numerical phantom. *PLoS ONE*, 12(11), 2017.

[77] Karen Breitman, Satyapal Rathee, Chris Newcomb, Brad Murray, Don Robinson, Colin Field, Heather Warkentin, Sherry Connors, Marc MacKenzie, Peter Dunscombe, and Gino Fallone. Experimental validation of the Eclipse AAA algorithm. *Journal of Applied Clinical Medical Physics*, 8(2), 2007.

[78] Janne Sievinen, Waldemar Ulmer, and Wolfgang Kaissl. AAA photon dose calculation model in Eclipse. *Palo Alto (CA): Varian Medical Systems*, Varian doc, 2005.

[79] Andrea Bezjak, Rebecca Paulus, Laurie E. Gaspar, Robert D. Timmerman, William L. Straube, William F. Ryan, Yolanda I. Garces, Anthony T. Pu, Anurag K. Singh, Gregory M. Videtic, Ronald C. McGarry, Puneeth Iyengar, Jason R. Pantarotto, James J. Urbanic, Alexander Y. Sun, Megan E. Daly, Inga S. Grills, Paul Sperduto, Daniel P. Normolle, Jeffrey D. Bradley, and Hak Choy. Safety and efficacy of a five-fraction stereotactic body radiotherapy schedule for centrally located non–small-cell lung cancer: NRG Oncology/RTOG 0813 trial. *Journal of Clinical Oncology*, 37(15), 2019.

[80] Jericho O'Connell and Magdalena Bazalova-Carter. fastCAT: Fast Cone Beam CT (CBCT) Simulation. *Medical Physics*, 48:4448–4458, 2021.

[81] Aleksandra Grzadziel, Barbara Smolinska, Roman Rutkowski, and Krzysztof Slosarek. EPID dosimetry - Configuration and pre-treatment IMRT verification. *Reports of Practical Oncology and Radiotherapy*, 12(6):307–312, 11 2007.

[82] Ben Mijnheer, Sam Beddar, Joanna Izewska, and Chester Reft. In vivo dosimetry in external beam radiotherapy. *Medical Physics*, 40(7), 7 2013.

[83] Sofia Celi, Emilie Costa, Claas Wessels, Alejandro Mazal, Alain Fourquet, and Pascal Francois. EPID based in vivo dosimetry system: clinical experience and results. *Journal of Applied Clinical Medical Physics*, 17(3):262–276, 5 2016.

[84] Parham Alaei and Emiliano Spezi. Imaging dose from cone beam computed tomography in radiation therapy. *Physica Medica*, 31(7):647–658, 11 2015.

[85] C. Lindsay, M. Bazalova-Carter, A. Wang, D. Shedlock, M. Wu, M. Newson, L. Xing, W. Ansbacher, R. Fahrig, and J. Star-Lack. Investigation of combined kV MV CBCT imaging with a high-DQE MV detector. *Medical Physics*, 46(2):563–575, 2 2019.

[86] Meng Wu, Andreas Keil, Dragos Constantin, Josh Star-Lack, Lei Zhu, and Rebecca Fahrig. Metal artifact correction for x-ray computed tomography using kV and selective MV imaging. *Medical Physics*, 41(12), 12 2014.

[87] Guillermo Hernández and Francisco Fernández. xpecgen: A program to calculate x-ray spectra generated in tungsten anodes. *The Journal of Open Source Software*, 1(7):62, 11 2016.

[88] I Kawrakow, E Mainegra-Hing, DWO Rogers, F Tessier, and BRB Walters. The EGSnrc Code System, Monte Carlo Simulation of Electron and photon Transport. *NRCC Report PIRS-701, National Research Council Canada*, 2018.

[89] David Parsons, James L. Robar, and Daren Sawkey. A Monte Carlo investigation of low-Z target image quality generated in a linear accelerator using Varian's VirtuaLinac. *Medical Physics*, 41(2):021719, 2 2014.

[90] Mengying Shi, Marios Myronakis, Yue Houng Hu, Daniel Morf, Joerg Rottmann, and Ross Berbeco. A Monte Carlo study of the impact of phosphor optical properties on EPID imaging performance. *Physics in Medicine and Biology*, 63(16):165013, 8 2018.

[91] Renu Sharma, Vandana Sharma, Parjit S. Singh, and Tejbir Singh. Effective atomic numbers for some calcium–strontium-borate glasses. *Annals of Nuclear Energy*, 45:144–149, 7 2012.

[92] Melanie Freed, Stuart Miller, Katherine Tang, and Aldo Badano. Experimental validation of Monte Carlo (MANTIS) simulated x-ray response of columnar CsI scintillator screens. *Medical Physics*, 36(11):4944–4956, 2009.

[93] M.J. Berger, J.H. Hubbell, S.M. Seltzer, J. Chang, J.S. Coursey, R. Sukumar, D.S. Zucker, and K. Olsen. XCOM: Photon Cross Sections Database - Version 1.5.

[94] D. R. White, J. Booz, R. V. Griffith, J. J. Spokas, and I. J. Wilson. Report 44. *Journal of the International Commission on Radiation Units and Measurements*, os23(1):NP–NP, 1 1989.

[95] Ander Biguri, Manjit Dosanjh, Steven Hancock, and Manuchehr Soleimani. TIGRE: A MATLAB-GPU toolbox for CBCT image reconstruction. *Biomedical Physics and Engineering Express*, 2(5):055010, 9 2016.

[96] L. A. Feldkamp, L. C. Davis, and J. W. Kress. Practical cone-beam algorithm. *Journal of the Optical Society of America A*, 1(6):612, 6 1984.

[97] John Paul Archambault and Ernesto Mainegra-Hing. Comparison between EGSnrc, Geant4, MCNP5 and Penelope for mono-energetic electron beams. *Physics in Medicine and Biology*, 60(13), 2015.

[98] H. Q. Woodard and D. R. White. The composition of body tissues. *The British Journal of Radiology*, 59(708):1209–1218, 12 1986.

[99] William Hadley Richardson. Bayesian-Based Iterative Method of Image Restoration*. *Journal of the Optical Society of America*, 62(1):55, 1 1972.

[100] L. B. Lucy. An iterative technique for the rectification of observed distributions. *The Astronomical Journal*, 79:745, 6 1974.

[101] Ehsan Abadi, W. Paul Segars, Hamid Chalian, and Ehsan Samei. Virtual Imaging Trials for Coronavirus Disease (COVID-19). *American Journal of Roentgenology*, pages 1–7, 8 2020.

[102] Jericho O'Connell, Clayton Lindsay, and Magdalena Bazalova-Carter. Experimental validation of Fastcat kV and MV cone beam CT (CBCT) simulator. *Medical Physics*, 48(11):6869–6880, 4 2021.

[103] D. A. Jaffray and J. H. Siewerdsen. Cone-beam computed tomography with a flat-panel imager: Initial performance characterization. *Medical Physics*, 27(6), 2000.

[104] David A. Jaffray, Jeffrey H. Siewerdsen, John W. Wong, and Alvaro A. Martinez. Flat-panel cone-beam computed tomography for image-guided radiation therapy. *International Journal of Radiation Oncology Biology Physics*, 53(5), 2002.

[105] Tong Xu, Justin L Ducote, Jerry T Wong, and Sabee Molloi. Dynamic dual-energy chest radiography: a potential tool for lung tissue motion monitoring and kinetic study. *Physics in Medicine and Biology*, 56(4):1191–1205, 2 2011.

[106] Wolfgang Kainz, Esra Neufeld, Wesley E. Bolch, Christian G. Graff, Chan Hyeong Kim, Niels Kuster, Bryn Lloyd, Tina Morrison, Paul Segars, Yeon Soo Yeom, Maria Zankl, X. George Xu, and Benjamin M. W. Tsui. Advances in Computational Human Phantoms and Their Applications in Biomedical Engineering—A Topical Review. *IEEE Transactions on Radiation and Plasma Medical Sciences*, 3(1), 2018.

[107] Xiang Li, Ehsan Samei, W. Paul Segars, Gregory M. Sturgeon, James G. Colsher, Greta Toncheva, Terry T. Yoshizumi, and Donald P. Frush. Patient-specific radiation dose and cancer risk estimation in CT: Part II. Application to patients. *Medical Physics*, 38(1), 2011.

[108] H. Jiang and H. Paganetti. Adaptation of GEANT4 to Monte Carlo dose calculations based on CT data. *Medical Physics*, 31(10), 2004.

[109] Blyth C. Simon. Opticks : GPU Optical Photon Simulation for Particle Physics using NVIDIA OptiX. In *Journal of Physics: Conference Series*, volume 898, 2017.

[110] Yeon Soo Yeom, Min Cheol Han, Chansoo Choi, Haegin Han, Bangho Shin, Takuya Furuta, and Chan Hyeong Kim. Computation Speeds and Memory Requirements of Mesh-Type ICRP Reference Computational Phantoms in Geant4, MCNP6, and PHITS. *Health Physics*, 116(5), 2019.

[111] Xun Jia, Hao Yan, Laura Cerviño, Michael Folkerts, and Steve B. Jiang. A GPU tool for efficient, accurate, and realistic simulation of cone beam CT projections. *Medical Physics*, 39(12), 2012.

[112] Bruno De Man, Samit Basu, Naveen Chandra, Bruce Dunham, Peter Edic, Maria Iatrou, Scott McOlash, Paavana Sainath, Charlie Shaughnessy, Brendon Tower, and Eugene Williams. CatSim: a new computer assisted tomography simulation environment. In *Medical Imaging 2007: Physics of Medical Imaging*, volume 6510, 2007.

[113] Ning Li, Hua Xia Zhao, Sang Hyun Cho, Jung Gil Choi, and Myoung Hee Kim. A fast algorithm for voxel-based deterministic simulation of X-ray imaging. *Computer Physics Communications*, 178(7), 2008.

[114] Beat Münch, Pavel Trtik, Federica Marone, and Marco Stampanoni. Stripe and ring artifact removal with combined wavelet-Fourier filtering. *EMPA Activities*, (2009-2010 EMPA ACTIVITIES), 2009.

[115] Jens Wiegert, Matthias Bertram, Dirk Schaefer, Norbert Conrads, Jan Timmer, Til Aach, and Georg Rose. Performance of standard fluoroscopy antiscatter grids in flat-detector-based cone-beam CT. In *Medical Imaging 2004: Physics of Medical Imaging*, volume 5368, 2004.

[116] Adrian Howansky, A. R. Lubinsky, S. K. Ghose, Katsuhiko Suzuki, and Wei Zhao. Direct measurement of Lubberts effect in CsI:Tl scintillators using single x-ray photon imaging. In *Medical Imaging 2017: Physics of Medical Imaging*, volume 10132, 2017.

[117] Joshua M. Wilson, Olav I. Christianson, Samuel Richard, and Ehsan Samei. A methodology for image quality evaluation of advanced CT systems. *Medical Physics*, 40(3), 2013.

[118] Jericho O'Connell and Magdalena Bazalova-Carter. Investigation of image quality of MV and kV CBCT with low-Z beams and high DQE detector. *Medical Physics*, 49(4), 2022.

[119] Alexis Bujold, Tim Craig, David Jaffray, and Laura A. Dawson. Image-Guided Radiotherapy: Has It Influenced Patient Outcomes? *Seminars in Radiation Oncology*, 22(1):50–61, 1 2012.

[120] Hiroshi Fujita, Du Yih Tsai, Takumi Itoh, Kunio Doi, Junji Morishita, Katsuhiko Ueda, and Akiyoshi Ohtsuka. A Simple Method for Determining the Modulation Transfer Function in Digital Radiography. *IEEE Transactions on Medical Imaging*, 11(1):34–39, 1992.

[121] Miguel López-Sánchez, María Pérez-Fernández, José Manuel Fandiño, Antonio Teijeiro, Víctor Luna-Vega, Nicolás Gómez-Fernández, Faustino Gómez, and Diego M. González-Castaño. An EGS Monte Carlo model for Varian TrueBEAM treatment units: Commissioning and experimental validation of source parameters. *Physica Medica*, 64, 2019.

[122] M. F. Chan, J. Yang, Y. Song, C. Burman, P. Chan, and S. Li. Evaluation of imaging performance of major image guidance systems. *Biomedical Imaging and Intervention Journal*, 7(2), 2011.

[123] J. O'Connell, S. Kundu, M. Saidaminov, and M. Bazalova-Carter. Next generation high resolution perovskite direct conversion detector: Monte Carlo design optimisation and virtual clinical trial. *Physics in Medicine and Biology*, 68(2), 2023.

[124] Amlan Datta, John Fiala, and Shariar Motakef. 2D perovskite-based high spatial resolution X-ray detectors. *Scientific Reports*, 11(1), 2021.

[125] Chelsea A. S. Dunning, Jericho O'Connell, Spencer M. Robinson, Kevin J. Murphy, Adriaan L. Frencken, Frank C. J. M. van Veggel, Kris Iniewski, and Magdalena Bazalova-Carter. Photon-counting computed tomography of lanthanide contrast agents with a high-flux 330-$\mu$m-pitch cadmium zinc telluride detector in a table-top system. *Journal of Medical Imaging*, 7(03), 2020.

[126] W. Que and J. A. Rowlands. X-ray Imaging Using Amorphous Selenium: Inherent Spatial Resolution. *Medical Physics*, 22(4), 1995.

[127] J. A. Rowlands, D. M. Hunter, and N. Arai. X-ray imaging using amorphous selenium: A photoinduced discharge readout method for digital mammography. *Medical Physics*, 18(3), 1991.

[128] Patrick J. Papin and H. K. Huang. A prototype amorphous selenium imaging plate system for digital radiography. *Medical Physics*, 14(3), 1987.

[129] Ulrich Neitzel, Ingo Maack, and Susanne Günther-Kohfah. Image Quality of A Digital Chest Radiography System Based on A Selenium Detector. *Medical Physics*, 21(4), 1994.

[130] D. Richtsmeier, C. A.S. Dunning, K. Iniewski, and M. Bazalova-Carter. Multi-contrast K-edge imaging on a bench-top photon-counting CT system: acquisition parameter study. *Journal of Instrumentation*, 15(10), 2020.

[131] Roberto Capote. IAEA NDS. *https://www-nds.iaea.org/phsp/photon1/*.

[132] May Abdel-Wahab, Soehartati S. Gondhowiardjo, Arthur Accioly Rosa, Yolande Lievens, Noura El-Haj, Jose Alfredo Polo Rubio, Gregorius Ben Prajogi, Herdis Helgadottir, Eduardo Zubizarreta, Ahmed Meghzifene, Varisha Ashraf, Stephen Hahn, Tim Williams, and Mary Gospodarowicz. Global Radiotherapy: Current Status and Future Directions—White Paper. *JCO Global Oncology*, (7), 2021.

[133] Katharine E. Heathcote and Bruce K. Armstrong. Disparities in cancer outcomes in regional and rural Australia, 2007.

[134] Talar W. Markossian, Robin B. Hines, and Rana Bayakly. Geographic and racial disparities in breast cancer-related outcomes in Georgia. *Health Services Research*, 49(2), 2014.

[135] Peter D. Baade, Paramita Dasgupta, Joanne F. Aitken, and Gavin Turrell. Distance to the closest radiotherapy facility and survival after a diagnosis of rectal cancer in queensland. *Medical Journal of Australia*, 195(6), 2011.

[136] Jean A. Laissue, Hans Blattmann, and Daniel N. Slatkin. Alban Köhler (1874-1947): Inventor of grid therapy. *Zeitschrift fur Medizinische Physik*, 22(2), 2012.

[137] Brian Loughery, Robert Halford, Kathryn Dess, Joseph Rakowski, Mary Cox, Joseph Koh, Alan Mayville, Jeffery Riess, and Michael Snyder. A proof of concept kilovoltage intensity modulated radiotherapy platform for the treatment of glioblastoma multiforme. *Biomedical Physics and Engineering Express*, 5(5), 2019.

[138] Nicolas D. Prionas, Sarah E. McKenney, Robin L. Stern, and John M. Boone. Kilovoltage rotational external beam radiotherapy on a breast computed tomography platform: A feasibility study. *International Journal of Radiation Oncology Biology Physics*, 84(2), 2012.

[139] Hassan Abbas, Dip N. Mahato, Jahangir Satti, and C. A. Macdonald. Measurements and simulations of focused beam for orthovoltage therapy. *Medical Physics*, 41(4), 2014.

[140] Dylan Y. Breitkreutz, Marc André Renaud, Jan Seuntjens, Michael D. Weil, Sergei Zavgorodni, and Magdalena Bazalova-Carter. Inverse optimization of low-cost kilovoltage x-ray arc therapy plans. *Medical Physics*, 45(11), 2018.

[141] A. van de Schoot, D. Hoffmans, K. van Ingen, M. Simons, M. Admiraal, N. van Wieringen, and J. Wiersma. PO-1611 Characterization of Ethos therapy systems for adaptive radiotherapy: a multi-machine comparison. *Radiotherapy and Oncology*, 161, 2021.

[142] Lei Zhu, Yaoqin Xie, Jing Wang, and Lei Xing. Scatter correction for cone-beam CT in radiation therapy. *Medical Physics*, 36(6), 2009.

[143] Yuan Xu, Ti Bai, Hao Yan, Luo Ouyang, Arnold Pompos, Jing Wang, Linghong Zhou, Steve B. Jiang, and Xun Jia. A practical cone-beam CT scatter correction method with optimized Monte Carlo simulations for image-guided radiation therapy. *Physics in Medicine and Biology*, 60(9), 2015.

[144] Ruijiang Li and Lei Xing. An adaptive planning strategy for station parameter optimized radiation therapy (SPORT): Segmentally boosted VMAT. *Medical Physics*, 40(5), 2013.

[145] Gregory Smyth, Philip M. Evans, Jeffrey C. Bamber, and James L. Bedford. Recent developments in non-coplanar radiotherapy, 2019.

[146] Lei Xing and Ruijiang Li. Inverse planning in the age of digital LINACs: Station parameter optimized radiation therapy (SPORT). In *Journal of Physics: Conference Series*, volume 489, 2014.

[147] Charles Huang, Yong Yang, and Lei Xing. Fully automated noncoplanar radiation therapy treatment planning. *Medical Physics*, 48(11), 2021.

[148] Magdalena Bazalova, Jean-François Carrier, Luc Beaulieu, and Frank Verhaegen. Dual-energy CT-based material extraction for tissue segmentation in Monte Carlo dose calculations. *Physics in Medicine and Biology*, 53(9), 2008.

[149] M. J.D. Powell. Restart procedures for the conjugate gradient method. *Mathematical Programming*, 12(1), 1977.

[150] D W O Rogers, B Walters, and I Kawrakow. BEAMnrc Users Manual. *Source*, 2005.

[151] Thitiporn Jaruthien, Sarin Kitpanit, Danita Kannarunimit, Chonnipa Nantavithya, Anussara Prayongrat, Petch Alisanant, Kitwadee Saksornchai, Napapat Amornwichet, Tassapong Raiyava, Chakkapong Chakkabat, Chawalit Lertbutsayanukul, Chonlakiet Khorprasert, and Kanjana Shotelersuk. Flattening filter free stereotactic body radiation therapy for lung tumors: outcomes and predictive factors. *Translational Cancer Research*, 10(2), 2021.

[152] Iris C. Gibbs and Billy W. Loo. CyberKnife stereotactic ablative radiotherapy for lung tumors, 2010.

[153] H. M. Garnica-Garza. Stereotactic breast irradiation with kilovoltage x-ray beams. *Physics in Medicine and Biology*, 61(2), 2016.

[154] James F. Hainfeld, Henry M. Smilowitz, Michael J. O'connor, Farrokh Avraham Dilmanian, and Daniel N. Slatkin. Gold nanoparticle imaging and radiotherapy of brain tumors in mice. *Nanomedicine*, 8(10), 2013.

[155] E. Lechtman, N. Chattopadhyay, Z. Cai, S. Mashouf, R. Reilly, and J. P. Pignol. Implications on clinical scenario of gold nanoparticle radiosensitization in regards to photon energy, nanoparticle size, concentration and location. *Physics in Medicine and Biology*, 56(15), 2011.

[156] Lei Pan, Yihui He, Vladislav V. Klepov, Michael C. De Siena, and Mercouri G. Kanatzidis. Perovskite CsPbBr3Single Crystal Detector for High Flux X-Ray Photon Counting. *IEEE Transactions on Medical Imaging*, 41(11), 2022.

[157] Martin J. Willemink, Mats Persson, Amir Pourmorteza, Norbert J. Pelc, and Dominik Fleischmann. Photon-counting CT: Technical principles and clinical prospects, 2018.

[158] Ehsan Abadi, Brian Harrawood, Jayasai R. Rajagopal, Shobhit Sharma, Anuj Kapadia, William Paul Segars, Karl Stierstorfer, Martin Sedlmair, Elizabeth Jones, and Ehsan Samei. Development of a scanner-specific simulation framework for photon-counting computed tomography. *Biomedical Physics and Engineering Express*, 5(5), 2019.

[159] A. Platek, A. Ostrowski, M. Platek, A. Beattie, S. Fung-Kee-Fung, V. Gupta, D. Cohan, W. Hicks, H. Arshad, M.A. Kuriakose, and A.K. Singh. Free Open Source REDCap Software to Track EORTC QLQ-30 and H&N-35 Quality of Life Scores and Allow Real-Time Clinical Management of Individual Patients. *International Journal of Radiation Oncology*Biology*Physics*, 94(4), 2016.

# Appendix A

# Additional Information

## A.1 Fastcat Validation

### A.1.1 Fastcat Experimental Validation Simulations

Here is a brief description of the kV and MV Fastcat models used for experimental validation. The kV Fastcat simulation used as input an analytical x-ray source generated in xpecgen [87] with an anode angle of 14° and a tube voltage of 100 kVp. The source was subject to additional analytical filtration of 2.7 mm of aluminum and a 0.89 mm titanium beam hardening filter. The detector modelled in the simulation was a columnar CsI detector with optical properties based on the work of Freed *et al.* [92]. The columnar CsI was 0.6 mm thick with a fill factor of 70% and a pixel pitch of 384 $\mu$m.

The MV Fastcat simulation source was a 6 MV Truebeam phase-space file provided by Varian. Although considered preferable by the authors, an analytical simulation of the MV beam was not used as a suitable model could not be found. This phasespace was binned by photon energy to provide a photon spectra for input into Fastcat. The detector used in the simulation was modelled as a Varian as1200 detector using the optical properties from Shi et al [90]. This detector is the same as described in previous work [80]. The GOS scintillator was 0.29 mm thick with a pixel pitch of 392 $\mu$m.

### A.1.2 Dose Comparison

A validation of dose linearity was performed. Four CBCTs at increasing doses were acquired experimentally for both the kV and the MV setups. Doses were measured using machine CTDI for the kV CBCTs with CTDIs of 5.27, 7.03, 10.55, and 21.1 with a 16 cm diameter CTDI phantom. Four MV CBCTs were acquired with machine MU values which were 75, 100, 150, and 300 MU. The dose in Fastcat was adjusted such that the average CNR over all inserts in the Catphan phantom agreed with that of the experimental CBCT with the lowest dose averaged. This Fastcat dose was then multiplied by factors of 1.5, 2, and 4. Agreement between average CNR was then compared between these Fastcat simulations and the experimental CBCTs.

An MC validation of the Mean phantom dose for a single projection was performed. Mean phantom dose for a single projection was calculated in Topas [69] using an MC model of the Catphan phantom with $2{\times}10^8$ initial photons. This dose was compared to the dose calculated in Fastcat for the same number of photons. These simulations used the Geant4 Penelope physics list and a particle range cutoff of $5\mu$m. Simulations were run on a linux desktop computer with 8 Intel Skylake CPUs. No variance reduction techniques were used. Two simulations were run in total, one with the 6 MV Varian phasespace file and one with an analytical 100 kVp x-ray spectrum filtered by 2.7 mm of aluminum, 0.89 mm titanium, and an aluminum bowtie filter. Both simulations measured the mean phantom dose to virtual Catphan 504 phantom.

The mean dose values from the MC simulations were used to perform a back of the envelope calculation to check that values were consistent between Fastcat kV and MV mean phantom doses and linac values reported as CTDI and in MUs, respectively. A conversion factor between the number of Fastcat photons to Fastcat mean phantom dose was estimated using the ratio of the dose scored in the MC simulations to the number of MC-simulated photons. The conversion factors were multiplied by the number of photons in the kV and MV experimental Fastcat simulations to get the mean phantom dose per projection and finally by the number of experimental projections to get the mean phantom dose for the total simulation.

## A.2 kV Radiotherapy

### A.2.1 Non-coplanar Angles

Non-coplanar angle were spaced equally about a unit sphere around the isocenter. For a number of angles $n$ these angles were then assigned a non-coplanar angle $\nu$ and helical angle $\phi$ calculated using the following pseudocode algorithm:

```
$\alpha = 4.0 * \pi / n$
$d = \sqrt{\alpha}$
$m_\nu = \text{round}(\pi / d)$
$d_\nu = \pi / m_\nu$
$d_\phi = \alpha / d_\nu$
for m in range(0, $m_\nu$):
    $\nu = \pi * (m + 0.5) / m_\nu$
    $m_\phi = \text{round}(2 * \pi * \sin(\nu) / d_\phi)$
    for n in range(0, $m_\phi$):
        $\phi = 2 * \pi * n / m_\phi$
    end
end
```

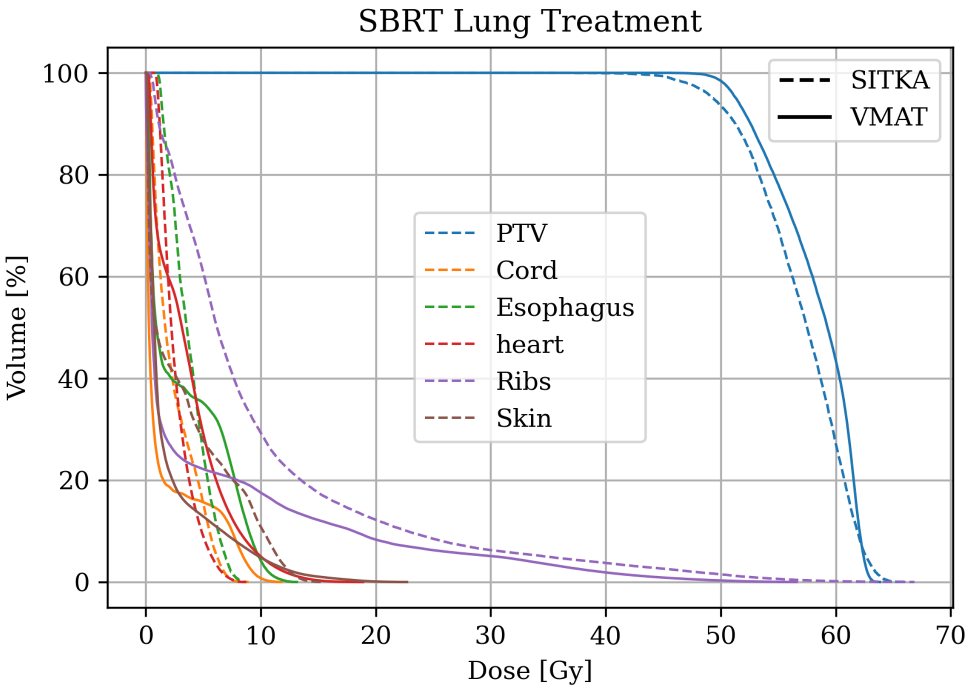

Figure A.1: Patient 1 dose distribution that violates the $R_{50\%}$ but passes all other RTOG dosimetric checks.

### A.2.2 Planning Trade Off

There existed a planning trade-off in meeting RTOG 0813 guidelines for the first patient in the study. The trade-off arose as part of patient 1's PTV margin included an area of rib bone. While it was possible to administer more conformal dose to the PTV than is shown in Figure 7.6 as demonstrated in Figure A.1, this pushed the PTV to encompass the ribs due to the high dose deposition of the kV beam in bony tissues. This expansion of the PTV isodose surface would then cause a minor violation in the $R_{50\%}$ which was generally the limiting factor in optimization. The $R_{50\%}$ being 4.3 which is higher than the 4.0 limit for this volume of PTV.

### A.2.3 Cost Function Figures

### A.2.4 Data Analysis

Data was analyzed using Python 3.8. The DICOM data was analyzed using the dicompyler [159] Python package to compute cumulative dose-volume histograms (DVHs) in Gy from a DICOM RT structure set for both the SITKA and VMAT plans. Additionally, mean doses, maximum doses, and doses delivered to specific volumes of a structure, such as the percentage of lung receiving 20 Gy or more ($V_{20}$), as outlined in RTOG 0813, were also computed using dicompyler.

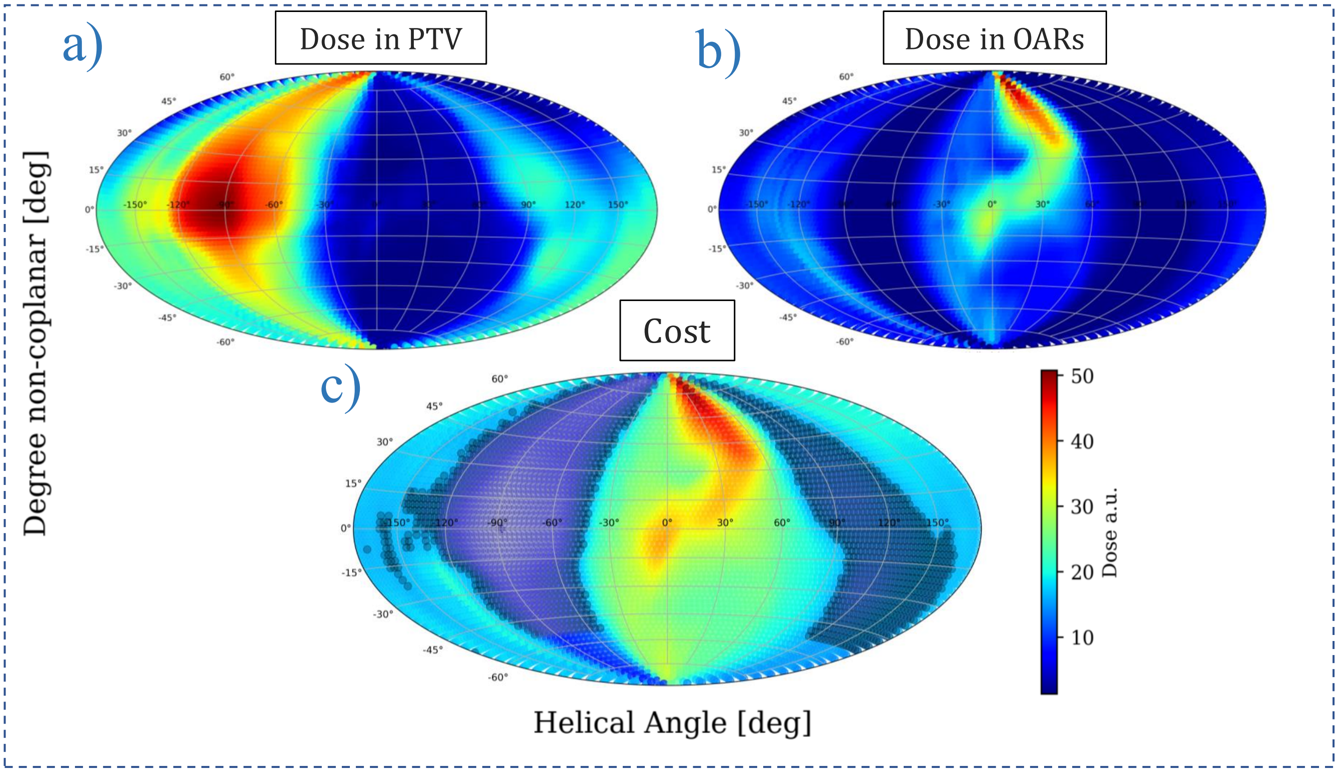

Figure A.1: a) The raytraced dose in the tumour and dose in the OARs is shown sampled at 6000 equally spaced angles around a sphere, a hammer projection was used to map the sphere to a two dimensional plot. b) An example of the cost function as a function of helical and non-coplanar angle, darkened areas denoting the angles selected.

### A.2.5 Idealised Collimation

While the collimation in our simulations was idealised, this decision was made because it was considered a conservative parameter. One challenge encountered during the optimization process was that the beam's falloff was too sharp, resulting in certain areas of the tumor receiving doses below the prescription isodose line. The inclusion of a penumbra, which was not directly addressed in our simulations, would have helped in the optimization process by providing a smoother dose distribution. However, we used Gaussian filtration of the beam to remove noise, which had a similar smoothing effect as a penumbra. The omission of real collimation from the simulation was done to maintain computational efficiency.

To demonstrate the impact of the penumbra on arc kV beams, we modelled two arcs: one with lead collimation of 2 mm placed 10 cm away from the source, and another with the idealised collimation as used in our work. Both beams were collimated to 3 cm at the isocenter, and the dose for $5 \times 10^7$ photons was measured in a 10 cm diameter water cylinder for a single angle. The dose distribution was then radially convolved around the cylinder to create an arc. Figure A.1 presents the dose distributions for the two beams. It can be observed that while the realistic collimation results in a slightly smoother dose falloff, the deviation from the idealised dose distribution does not exceed 4%.

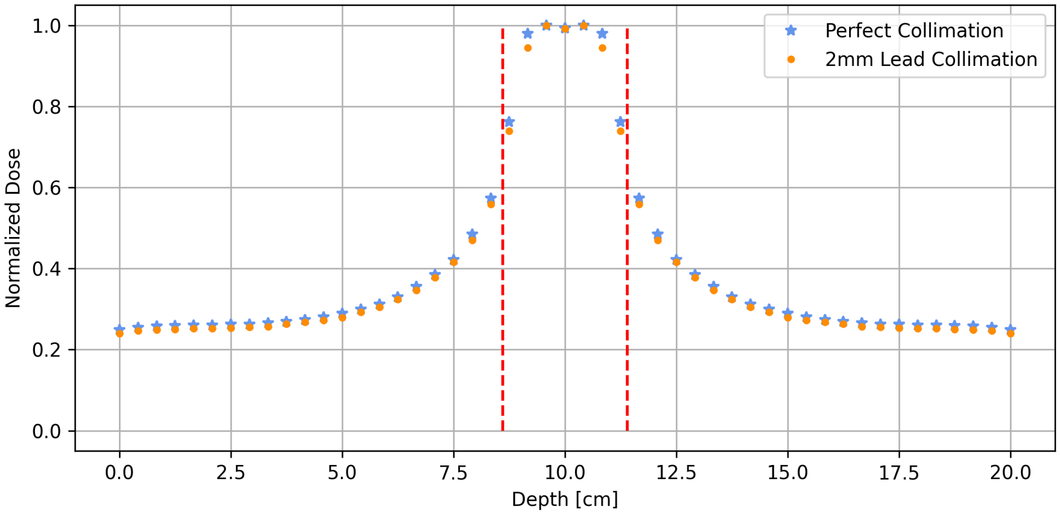

Figure A.1: Two MC dose profiles through the central axis of a 10 cm diameter cylinder are shown. One using idealised collimation and the second using 2 mm of lead collimation. Red lines denote the boundary of the collimation inside the phantom.